The preparation and characterisation of nano-metal hexacyanoferrates with a potential catalytic application

A dissertation submitted in accordance with the requirements for the degree

Magister Scientiae

In the

Faculty of Natural and Agricultural Sciences

Department of Chemistry

At the

University of the Free State

By

Stephanus Johannes Gerber

Date

November 2016

Supervisor

Dr. E. Erasmus

Aan my pa, Chris Gerber
(25 November 1959 – 24 Maart 2016)

‘n Seun wil soos sy pa wees
‘n Seun wil sy pa trots maak
Van jag tot visvang
handtekening en biltong hang

Ek het soveel as moontlik lewenskennis uit jou gekry,
Maar tog was dit nie genoeg nie
Want geen storie sal ‘n seun reg maak om ‘n man te word nie

Jy was my held, my makelaar,
my botanis en my finansiële adviseur

Ek voel ontneem
van die geleentheid om die steun aan jou terug te verleen

Ek sal myself eendag weer bevind tussen die rooi duine van die Kalahari
Daar sal ek aan jou dink
En ‘n glasie op jou klink
En onthou hoe ‘n gemsbok se grys pels blink

“Als van jou wat in my gis, gee my hoendervleis as dit November is”
– Fokofpolisiekar

Abstract

A series of bulk and nano-sized metal hexacyanoferrates ($KM_y[Fe(CN)_6]_z \cdot qH_2O$, M = Fe, Co, Ni and Cu) were prepared by a co-precipitation and reverse emulsion reaction, respectively. The yields obtained were dependant on the Pauling scale electronegativity, σ_M, of the metal M. Transmission electron microscopy showed that nano-sized metal hexacyanoferrates had an average size between 46 and 124 nm. Multiple CN peaks in the 1900 – 2200 cm^{-1} area of the infrared spectroscopy of the prepared coordination compounds confirmed mixed oxidation states of the different metals in the metal hexacyanoferrates. X-ray photoelectron spectroscopy was used to determine the ratio between the metals as well as the ratio of each oxidation state present of the different metals. The comparison of results between infrared spectroscopy and X-ray photoelectron spectroscopy gave insight into the electron distribution, charge transfer and degree of covalency within these compounds. The thermal gravimetric analyses indicated that mass loss upon heating are categorised into three groups: up to ~200 °C, external water is evaporated, ~200 to ~300 °C intercalated (internal) water is lost and from ~300 °C onwards decomposition of the organic binder occurs. This is confirmed by differential scanning calorimetry and comparative Fourier transformed infrared spectroscopy recorded after each heating stage. Cobalt hexacyanoferrate was used to modify electrodes by either physical coating or by electrodeposition of a glassy carbon working electrode, carbon paste modified electrodes were also prepared. The electrochemical response of the modified electrodes were tested in a blank water and acetonitrile solution. The electrochemical behaviour in water/KCl of cobalt hexacyanoferrates-electrodeposited modified glassy carbon electrode (**GCED**), showed an electrochemically reversible (ΔE = 0 mV) but chemically irreversible ($i_{pa}/i_{pc} < 1$) Fe^{II}/Fe^{III} couple. The modified glassy carbon electrodes revealed no Co^{II}/Co^{III} couples, which implies that the compounds crystallised in the insoluble form. The influence on the fast electron transfer compound ferrocene was also investigated. These electrodes were also tested for their electrocatalytic oxidation of hydrazine.

The heterogeneous hydrogenation of 1-octene was tested to determine the viability and practicality of metal hexacyanoferrate compounds as heterogeneous catalytic material. It was determined, during these

preliminary catalysis experiments, that more than one product formed during the hydrogenation of 1-octene, exhibiting that metal hexacyanoferrates has the potential to be used as heterogeneous catalysts.

Keywords: metal hexacyanoferrates, FTIR, XPS, TGA, TEM, electrode modification, hydrazine oxidation, cyclic voltammetry.

Opsomming

'n Reeks grootmaat- asook nano-grootte metaal heksasianoferraat partikels ($KM_y[Fe(CN)_6]_z \cdot qH_2O$, M = Fe, Co, Ni en Cu) is voorberei met behulp van 'n gesamentlike presipitasie en omgekeerde emulsie reaksie, onderskeidelik. Dit is gevind dat die opbrengs afhanklik is van die Pauling elektronegatiwiteit, σ_M, van die metaal M. Transmissie elektron mikroskopie het getoon dat die nano-grootte metaal heksasianoferrate se gemiddelde groottes tussen 46 en 124 nm varieer. Daar is veelvuldige CN pieke in die 1900 – 2200 cm^{-1} gebied van die infrarooi spektroskopie gevind van die voorbereide koördinasieverbindings, wat die gemengde oksidasietoestande van die verskillende metale in die heksasianoferrate bevestig het. X-straal foto-elektron spekstroskopie is gebruik om die verhouding tussen die metale asook die verhouding van elke oksidasietoestand teenwoordig van die veerskillende metale te bepaal. Die vergelyking van resultate tussen infrarooi spektroskopie en X-straal foto-elektron spektroskopie het insig in die elektron verspreiding, ladingsoordrag en mate van koördinasie in hierdie verbindings gelewer. Die termiese gravimetriese ontledings het massaverlies by verwarming in drie groepe verdeel. Tot en met ~200 °C, is eksterne water molekules verdamp, tussen 200 °C en 300 °C is interkalêre (interne) water molekules verdamp en vanaf ~300 °C het die ontbinding van die organiese bindings plaasgevind. Hierdie word deur differensiaal skanderings kalorimetriese en fourier getransformeerde infrarooi spektroskopiese opnames bevestig wat geneem is na elke verwarmingsgedeelte. Kobalt heksasianoferraat is gebruik om elektrodes te modifiseer deur óf 'n fisiese laagvorming óf deur elektrodeponering van die oppervlak van 'n glasagtige koolstof werkselektrode. Koolstof puree gemodifiseerde elektrodes is ook voorberei. Die elektrochemiese

reaksie van die gemodifiseerde elektrodes is in blanko water en asetonitriel oplossings onderskeidelik getoets. Die invloed op die vinnige elektronoordraende verbinding ferroseen is ook ondersoek. Hierdie elektrodes is ook getoets vir hul elektrokatalitiese oksidasie van hidrasien.

Sleutelwoorde: metaal heksasianoferrate, FTIR, XPS, TGA, TEM, elektrode modifiseering, hydrasien oksidasie, sikliese voltammetrie.

Table of contents

List of abbreviations I

Chapter 1

Introduction and aims of study 1

1.1. Introduction 1

1.2. Aim 2

References 3

Chapter 2

Literature Survey 5

2.1 Introduction 5

2.2 Introduction to heterogeneous catalysis 5

2.3 Catalyst Supports 6

2.4 Co-precipitation as a preparation method 7

2.4.1. Preparation of catalytic material by Co-precipitation 9

2.5 Application of Mono metallic catalysts 10

2.6 Bimetallic catalysts 10

2.7 Metal Hexacyanometallates 15

2.7.1 Synthesis of Metal Hexacyanoferrates 16

2.7.1.1 Bulk material 17

2.7.1.2 Nano particles 17

2.7.2 Properties of MHCF 22

2.7.2.1 Electrochemistry 22

2.7.2.2 Magnetic properties 27

2.7.2.3 Ion Exchange 29

2.7.2.4 X-ray photoelectron spectroscopy 30

2.7.3 Applications 31

2.7.3.1 Energy storage 31

2.7.3.2 Biosensing 32

2.7.4 Catalysis with metal hexacyanoferrates 35

References 37

Chapter 3

Results and discussion 41

3.1 Introduction 41

3.2 Synthesis 42

3.2.1 Preparation of bulk-sized metal hexacyanoferrates 42

3.2.2. Preparation of nano-sized metal hexacyanoferrates 43

3.3 Characterisation 45

3.3.1 Transmission electron microscopy 45

3.3.1.1 Transmission electron microscopy of bulk material 45

3.3.1.2 Transmission electron microscopy of nano material 46

3.3.2 Inductively coupled plasma – optical emission spectroscopy 49

3.3.3 Attenuated Total Reflection Fourier Transformed Infrared 50

3.3.4 X-ray photoelectron spectroscopy 55

3.3.5 Thermal gravimetric analysis 67

3.3.6 Differential Scanning Calorimetry 72

3.3.7 Electrochemistry 74

3.3.7.1 Electrochemical characterisation of modified glassy carbon electrodes 75

3.3.7.2 Electrochemical characterisation of electrodeposited cobalt hexacyanoferrate on glassy carbon electrodes 79

3.3.7.3 Electrochemical characterisation of modified Carbon paste electrodes 82

3.3.7.4 Evaluation of oxidation on all the modified electrodes 84

3.3.7.5 Electrocatalytic oxidation of hydrazine on all the modified electrodes 87

3.3.8 Heterogeneous catalysis 89

References 92

Chapter 4

Experimental 95

4.1. Introduction 95

4.2. Materials 95

4.3. Spectroscopic measurements 95

4.3.1. Nuclear Magnetic Resonance 95

4.3.2. Attenuated Total Reflection Fourier Transformed Infrared 95

4.3.3. Thermogravimetric Analysis 96

4.3.4. X-ray Photoelectron Spectroscopy 96

4.3.5. Transmission Electron Microscopy 96

4.3.6. Differential Scanning Calorimetry 96

4.3.7. Inductive Coupled Plasma – Optical Emission Spectroscopy 97

4.4 Preparation of bulk-sized metal hexacyanometallates 98

4.4.1 Iron hexacyanoferrate 98

4.4.2 Cobalt hexacyanoferrate 99

4.4.3 Nickel hexacyanoferrate 100

4.4.4 Copper hexacyanoferrate 101

4.5 Preparation of nano-sized metal hexacyanometallates 102

4.5.1 Metal Aerosol-OT 102

4.5.2 Iron hexacyanoferrate 102

4.5.3 Cobalt hexacyanoferrate 103

4.5.4 Nickel hexacyanoferrate 103

4.5.5 Copper hexacyanoferrate 104

4.6 Heterogeneous Catalysis Reactions 105

4.6.1 Hydrogenation of 1-Octene 105

4.6.1.1 Using Nickel Hexacyanoferrate 105

4.6.1.2 Using Coblat Hexacynoferrate 105

4.7 Electrode preparation 105

4.7.1 Physical coating of a glassy carbon electrode surface with the cobalt hexacyanoferrate B2 and N2 106

4.7.2 Electrodeposition of cobalt hexacyanoferrate onto a glassy carbon electrode surface 106

4.7.3 Cobalt hexacyanoferrate (B2 and N2) modified carbon paste electrodes 106

4.8. Electrochemistry 107

4.8.1 Electrochemical characterisation in blank solutions of modified electrodes 107

4.8.2 Evaluation of ferrocene oxidation on all the modified electrodes 107

4.8.3 Electrocatalytic oxidation of hydrazine on all the modified electrodes 107

References 107

Chapter 5

Conclusions and future prospects 108

5.1. Conclusion 108

5.2. Future prospects 111

Appendix 113

List of abbreviations

For simplicity, metal hexacyanoferrate complexes will be abbreviated as MHCF where M = the coordinated metal (Fe for iron, Co for cobalt, Ni for nickel and Cu for copper). When the oxidation states of the coordinated metals and iron in the metal hexacyanoferrate complexes are discussed the notation of M-C≡N-Fe or M-CN-Fe will be used where superscript roman numerals will be inserted accordingly to display the current oxidation state of the different metals. The stoichiometry for each metal hexacyanoferrate might not be accurately displayed by these abbreviations but will serve as a convenient notation. Regular periodic table element abbreviations will be used where applicable.

Å	angstrom
AOT	aerosol OT (Dioctyl sulfosuccinate sodium salt, the surfactant)
ATR FTIR	Attenuated Total Reflection Fourier Transformed Infrared
BE	binding energy
calc.	calculated
CTAB	cetyltrimetyl ammonium bromide
CTAFeII	cetyltrimetyl ammonium ferrocyanide
CN	cyanide
CoHCF	cobalt hexacyanoferrate
Coord.	coordinated
CP	carbon paste
CuHCF	copper hexacyanoferrate
CV	cyclic voltammetry
DSC	differential scanning calorimetry
EDTA	ethylenediaminetetraacetic acid
eV	electronvolt
FeHCF	iron hexacyanoferrate
FE-SEM	field emission scanning electron microscopy
Fc	ferrocene
GC	glassy carbon
HCF	hexacyanoferrate
ICP-OES	Inductively Coupled Plasma Optical Emission Spectroscopy

KNiHCF	potassium nickel hexacyanoferrate
KCoHCF	potassium cobalt hexacyanoferrate
MHCM	metal hexacyanometallate
MHCF	metal hexacyanoferrate
NiHCF	nickel hexacyanoferrate
NMR	Nuclear Magnetic Resonance
Oe	Oersted
PCy	cyclohexyl phosphine
pH	potential hydrogen
RME	reverse microemulsion
satel	satellite
$TBAPF_6$	tetra-*n*-butylammonium hexafluorophosphate
TEM	transmission electron microscopy
Temp.	temperature
TGA	thermal gravimetric analysis
UV	ultra violet
XPS	X-ray photoelectron spectroscopy

1 Introduction and aims of study

1.1 Introduction

Although metal hexacyanoferrate complexes have been studied extensively for different types of applications (including grid scale energy storage, biosensing and electrocatalysis),[1, 2, 3] with respect of the knowledge of the author, there does not exist comprehensive characteristic study on these coordination compounds. A coherent study that compare the different types of characteristic properties in finding the explanation of the individual characteristic properties are in need of attention. This would give insight into the electron distribution, charge transfer and degree of covalency within these compounds. It would also provide a better understanding of how the compounds can form nano-sized particles and what their catalytic capabilities would be limited to if applicable.

Nano-sized catalytic particles have great value in heterogeneous catalysis. The possibilities of catalysing chemical reactions, on an industrial scale, are endless. [4]

Cyanometallates are coordination compounds where one or more cyanide ligands are coordinated to a metal center. One of the proposed products, Prussian blue, possesses an empirical formula of $Fe_4[Fe(CN)_6]_3$ which corresponds to a lattice structure that displays hexacoordinate low spin Fe^{II} atoms that are bonded through the carbon atom of the cyanide ligand as well as hexacoordinate, high spin Fe^{III} atoms that are bonded through the nitrogen atom in the cyanide ligand. By varying the oxidation state of the iron atoms at different sites on the cubic structure will result in different coordination compounds with different properties and different colours. By using linkage isomerism it also becomes possible to vary the metal atom that bonds through the nitrogen atom in these cyanometallates to other metals such as cobalt, nickel and copper. [5]

It is difficult to selectively prepare bimetallic particles in the original meaning of the word. It sometimes occur that the prepared material consists of a mixture of two separate monometallic particles as well as bimetallic particles.[6, 7] Metal hexacyanoferrates always form a compound with the two metals coordinated to each other through a cyanide bond in a single compound.

There are some advantages of these metal hexacyanoferrates that can be considered:

i) They can be prepared with relative ease;[3]

ii) They can be prepared at low cost;[8]

iii) They can be used in electrocatalysis;[9]

iv) They hold the potential of revolutionary technology in charge-storage devices;[10, 11]

vi) They possess a large interstitial site that can be used to house a catalytic entity;[12]

vii) They can be prepared in different shapes and sizes that can be controlled.[13]

Nanomaterials of metal hexacyanometallates usually exhibit multiple enhanced properties such as magnetic, electrical, surface, optical, catalytic, electrochemical, chemical and biological activities. Among other inorganic materials, transition metal hexacyanoferrates have undergone intensive study due to their exceptional characteristics such as mixed valency, water insolubility, high ionic conductivity as well as showing exceptional redox mediator properties.[14]

The electrochemistry of metal hexacyanometallates have great significance for both fundamental research and practical application. In terms of fundamental research, since for example cobalt hexacyanoferrate consists of multiple redox centers Co^{II}, Co^{III}, Fe^{II} and Fe^{III} in various stoichiometries, interesting electrochemical properties are expected. For practical application the electrochemistry is useful in biosensing, electrocatalysis, ion-exchange and charge storage capabilities.[10]

It has been shown that potassium cobalt hexacyanoferrate (KCoHCF) as ion exchanger proved chemical stability in nitric acid solutions of pH = 1, as well as favourable selective uptake for caesium ions over strontium and sodium ions. It was shown that the ion exchange capacity for caesium ions obtained for a binary system was found to be 1.72 meq/g.[15]

1.2 Aims of study

With the above background, the following goals were set for this study.

1) The synthesis and characterisation of a series of bulk-sized metal hexacyanoferrates with the general formula $K_xM_y[Fe(CN)_6]_z \cdot qH_2O$, with M = Fe, Co, Ni and Cu, and x, y, z and q representing stoichiometric numbers. Sizes of prepared particles will be confirmed with transmission electron microscopy.

2) The synthesis and characterisation of a series of nano-sized metal hexacyanoferrates with the general formula $K_xM_y[Fe(CN)_6]_z \cdot qH_2O$, with M = Fe, Co, Ni and Cu, and x, y, z and q representing stoichiometric numbers. Sizes of prepared particles will be confirmed with transmission electron microscopy.

3) Determination of the oxidation states of the different metal atoms as well as the amount of each state present in all synthesized metal hexacyanoferrates with the use of comparative Fourier transformed infrared spectroscopy and X-ray photoelectron spectroscopy.

4) Determination of thermal stability of all prepared metal hexacyanoferrates by means of thermal gravimetric analyses and differential scanning calorimetry.

5) Modification of a glassy carbon (working) electrode surface by either coating it with the metal hexacyanoferrate (followed by a nafion coating) or by electrodeposition of the metal hexacyanoferrate onto the surface from solution. Various carbon paste electrodes will also be prepared for comparison. Testing the electrochemical response of the modified electrodes in a blank water and acetonitrile solution.

6) These metal hexacyanoferrates modified electrodes' influence will be examined on the cyclic voltammetry of the fast electron transfer compound ferrocene, as well as their electrocatalytic oxidation of hydrazine

7) Preliminary catalytic hydrogenation of 1-octene will be tested to determine if catalysis is indeed possible and viable.

To summarise, metal hexacyanoferrates can be synthesized with relative ease but the applications thereof holds revolutionary potential. Multiple types of characterisation methods will be applied on the prepared material and compared with one another for the purpose of a deeper understanding of properties such as mixed valency, water insolubility, high ionic conductivity, electron distribution, charge transfer, thermal stability, shape, size and degree of coordination.

References

[1] F. Ricci and G. Palleschi, *Biosensors and Bioelectronics*, 2005, **21**, 389-407.

[2] N. A. Sitnikova, M. A. Komkova, I. V. Khomyakova, E. E. Karyakina and A. A. Karyakin, *Analytical Chemistry*, 2014, **86**, 4131 – 4134.

[3] C. D. Wessells, M. T. McDowell, S. V. Peddada, M. Pasta, R. A. Huggins and Y. Cui, *American Chemical Society*, 2012, **2**, 1688-1689.

[4] A. T. Bell, *Science*, 2003, **299**, 1688.

[5] J. E. Huheey, in *Inorganic Chemistry: Principles of structure and reactivity*, Harper & Row Publishers Inc., New York, 3rd edn, 1983, ch. 10, pp. 521 – 523.

[6] M. T. Schaal, A. C. Pickerell, C. T. Williams and J. R. Monnier, *Journal of Catalysis*, 2008, **254**, 131.

[7] S. Djokic, *Modern Aspects of Electrochemistry,* 2002, **35**, 51.

[8] E. D. Park and J. S. Lee, *Journal of Catalysis*, 1999, **186**, 1.

[9] S. R. Ali, P. Chandra, M. Latwal, S. K. Jain, V. K. Bansal and S. P. Singh, *Chinese Journal of Catalysis*, 2011, **32**, 1844.

[10] L. Shi, T. Wu, M. Wang, D. Li, Y. Zhang and J. Li, *Chinese Journal of Chemistry*, 2005, **23**, 149 – 154.

[11] S. M. Chen, *Journal of Electroanalytical Chemistry*, 1996, **417**, 145.

[12] M. Berrettoni, M. Ciabocco, M. Fantauzzi, M. Giorgetti, A. Rossi and E. Caponetti, *Royal Society of Chemistry Advances*, 2015, **5**, 35435 -35445.

[13] S. Vaucher, M. Li and S. Mann, *Aangewandte Chemie International Edition,* 2000, **39**, 1793.

[14] S. R. Ali, V. K. Bansal, A. A. Khan, S. K. Jain and M. A. Ansari, *Journal of Molecular Catalysis A: Chemical*, 2009, **303**, 60-61.

[15] J. Moon, E. Lee and H. Kim, *Korean Journal of Chemical Engineering*, 2004, **21**, 1026-1031.

2 Literature survey

2.1 Introduction

A literature review of the preparation, the physical characterisation methods as well as applicable catalysis applications relevant to this study is presented in this chapter.

2.2 Introduction to heterogeneous catalysis

Heterogeneous catalysis can be explained as the form of catalysis where the phase of the catalytic material is different than the phase of the reactants that is used during a reaction. Different phases in this regard is not only limited to solid, liquid or gas phases but also immiscible liquids such as oil and water. Heterogeneous catalysts often consists of expensive noble metals such as Rh or Pt. By reducing the amount of metal that is utilized, will then have an economical interest element. It will therefore be economically preferable to prepare dispersed particles on a support or fine powders to bulk material. Using metal particles instead of bulk material can also affect the rate of the reaction mechanism.[1]

In explanation, heterogeneous catalytic reactions will usually involve adsorption of the reactants from a fluid phase onto a solid surface, after which surface reaction of adsorbed species will take place. Lastly, desorption of the products into the fluid phase follows. [2] A typical heterogeneous catalyst can be considered to be an inorganic solid such as metals, metal-oxides, -sulphides and salts, but can also be organic materials such as enzymes and ion exchangers.[3]

Heterogeneous catalysts usually consist of small particles that are supported on oxide substrates such as alumina or MgO. Industrially these reactions are run inside a reactor that is operated with a continuous flow under steady-state conditions. The rate of the reaction is usually determined, apart from the nature of the catalytically active surface, by external parameters such as temperature, flow rate and partial pressure.[4]

When comparing heterogeneous and homogeneous catalysis it can be seen that heterogeneous catalysis has a practical advantage considering that separation processes are uncomplicated by keeping catalysts and products in different phases.[4] Heterogeneous catalysts also have better thermal stability and are normally easier to prepare and handle. Heterogeneous catalysts have multiple active sites where homogeneous catalysts usually have a single active site.[5]

Important factors to consider in heterogeneous catalysts during their syntheses are the selectivity, activity, stability, morphology, mechanical strength, thermal characteristics, regenerability,

reproducibility, cost and originality. Heterogeneous catalysts can be differentiated between bulk materials and supported catalysts. The bulk material can be acquired relatively easily by use of precipitation, direct synthesis or leaching of an immense precursor.[5]

The main objective of a catalyst is to alter the rate and activity towards a chemical reaction in such a way that a specific product can be produced preferentially and in relative high yield. For example, in order to successfully achieve total selectivity towards unsaturated alcohols, the promotion of the polarization of the C=O double bond or the hindrance of the α, ß-unsaturated aldehyde adsorption *via* the C=C double bond is compulsory. This can be accomplished by the presence of two metals in a catalytic system. During a selective hydrogenation of cinnamaldehyde, a Cu-Co/SiO_2 combination catalyst has proven good selectivity in the direction of the formation of cinnamyl alcohol, while Co-Ni/SiO_2 and Ni-Cu/SiO_2 showed selectivity towards the formation of hydrocinnamaldehyde.[6]

During catalytic reactions, reactants are transferred to the catalyst surface where the reaction occurs in successive steps in such a way that the catalyst is regenerated in the final step. These steps are as follows:

1. Reactants are diffused from the bulk fluid phase to the external surface of the catalyst particle.
2. Reactants are diffused between particles through the catalyst pores to the internal active sites.
3. Reactants are adsorbed onto the active sites.
4. Catalyst reaction occurs on the surface of the catalyst.
5. Products are desorbed from catalyst surface.
6. Products are diffused between particles through the catalyst pores to the external surface of the catalyst particle.
7. Products are diffused from the external particle surface to the bulk of the fluid. [7]

2.3 Catalyst Supports

The main purpose of the catalyst support is the dispersion of the active catalyst (a small amount of small particles) over a large surface area. The support provides high surface area and stabilises the dispersion of the active component, [3] since small metal particles are often unstable and prone to sintering at catalytic conditions. Catalysts based on supported metal particles are widely used in both chemical industry and environmental catalysis. Supported catalysts are typically prepared by supporting an active phase on a high surface area support such as metal oxides (silica, alumina, zeolites, titania, magnesia, zinc oxide and zirconia) or carbon based supports like graphite, carbon nanotubes etc.[5] Although supports are generally considered as being inert it will not always be the case.[8]

Both bulk and supported catalysts usually contain one or more promoters that exercise different promoting roles such as improving the structural and phase stability, textural properties as well as catalytic activity.[5]

Supported palladium particles are a captivating example of how the metal-support interaction can play a role during the stabilization of the dispersion of metal particles. Compared to palladium metal, palladium oxide has a major affinity towards oxidic supports. Therefore, when a Pd/SiO_2 catalyst is heated in air at high temperatures, the metal particles will be oxidized above 350°C and palladium oxide produced tends to spread over the support, which in turn prevents sintering of the particles.[5]

2.4 Co-precipitation as preparation method

In principle there are two main routes for the preparation of supported catalysts; by impregnation or co-precipitation.[9, 10] The preparation process usually involves combining the precursor of the support and the active components, which is followed by drying and calcining at elevated temperatures, and if required further reduction. Modification of the preparation method may affect the catalytic performance. [10] Impregnation involves the loading of a pre-existing support material with the catalytically active material. This method is normally used for catalyst precursors that are expensive and the aim is to form nano-sized particles on the support.[11]

Co-precipitation can be defined as the simultaneous precipitation of a mixture of substances, the tracer (a trace amount of substance, normally the catalyst precursor) and the carrier (the support) from a solution (in which the substances are normally soluble). This method is normally used for catalyst precursors that are inexpensive and obtaining the maximum catalytic activity per volume is the main consideration. Co-precipitation occurs without regard to the specific mechanisms involved.[14] The three most important mechanisms which can occur during co-precipitation are: inclusion, occlusion and adsorbate.[12] Inclusion is defined as the co-precipitation of substances, where the tracer occupies a lattice site within the precipitate (crystal structure) without changing the regular structure of the lattice. Occlusion is where the tracer is not incorporated into the crystal lattice but is trapped within the crystal of the carriers as the crystal grows, giving rise to the formation of imperfections in the crystal. Adsorbate is the co-precipitation of a tracer onto the surface of the carrier crystal. This type of co-precipitation is only of practical importance when the precipitate has a large surface. In general, if the precipitate has a micro-crystalline character the amount of co-precipitation is, as a rule, of no practical significance.[13]

Co-precipitation is a method commonly used to purify many environmental issues, especially water resources. These include metal contaminant transport, metal concentrations in aquatic systems, wastewater treatment and acid mine drainage. [14] It is a possibility that this co-precipitation method can

be used to eliminate unwanted compounds in drinking water, however this might also lead the elimination of the desired product that precipitates out with the impurities.

Co-precipitation is a useful method to prepare composites (compounds made of two different metals or two different substances) of a mixture of substance for instance: $Pb(TiZr)O_3$, $PbTiO_3$ and $NiCo_2O_4$.[15, 16] During the preparation of these composites utilising the co-precipitation method has shown some specific advantages: [15]

- Homogeneity in mixed precipitates;
- Low-temperature synthesis (0 °C – 50 °C);
- Controlled morphology of the products;
- High specific surface of the products.

In the co-precipitation method, the precipitant is an important factor that affects the properties of the final product. For instance, Ni-Co spinel oxide could be prepared by co-precipitation using either hydroxide, carbonate or oxalic acid as the precipitant. The hydroxide prepared Ni-Co spinel oxide gave the highest specific area and has the best electrocatalytic behaviour. [16]

Another example in this regard, is the Ni-Al_2O_3 catalyst preparation via the co-precipitation method using different precipitants namely urea, Na_2CO_3, NaOH, K_2CO_3 and NH_4OH. During this study the Ni50-urea catalyst exhibited the largest specific surface area, the highest pore volume as well as the highest Ni dispersion and the largest Ni surface area (as depicted in the tabular representation below).[17]

Table 2.1: Physisorption results of catalysts prepared via co-precipitation using various precipitants.

Sample	Specific surface area (m^2 g-cat^{-1})	Pore Volume (cm^3 g-cat^{-1})	Average pore Size (nm)
Ni50-urea	210	0.77	15
Ni50-Na_2CO_3	183	0.47	10
Ni50-NaOH	206	0.33	6
Ni50-K_2CO_3	163	0.57	14
Ni50-KOH	169	0.31	7
Ni50-NH_4OH	127	0.40	13

Another interesting example is the effect the precipitant has on a Ni-CeO_2 (prepared by co-precipitation) the catalyst's catalytic performance as well as physical and chemical properties. The precipitants used were Na_2CO_3, NaOH and a mixture of Na_2CO_3 and NaOH in a 1:1 ratio. In this study it was found that the catalyst prepared by the mixture of the precipitants showed higher catalytic activities as well as had

the most amount of oxygen vacancies accompanied with highly dispersed Ni particles. While the Na_2CO_3 or NaOH precipitant catalysts resulted in little or no oxygen vacancies in Ni-CeO_2 and presented poor catalytic performance during methane steam reforming at different gas hourly spaced velocity regions. Ni50-urea and Ni50-K_2CO_3 exhibited the highest CH_4 conversion in all regions ranging from approximately 98% to approximately 67% – 70%.[18]

2.4.1 Preparation of catalytic material by Co-precipitation

It has been suggested that the preparation method and the synergism between active noble metal component and metal support play an important role in determining the catalytic performance.[10] Various methods and techniques have been explored in preparation of the supported noble metal catalysts in an effort to achieve better catalytic performance.

Various parameters such as the preparation conditions, choice of support and thermal treatment may affect the physiochemical, catalytic and surface properties of various catalytic systems towards some catalytic reactions. Catalysts that contain iron oxides are used in CO oxidation processes. Ferrites are the products of the reciprocal action between divalent metal oxides (the catalytic species) and Fe_2O_3.[19] Metal oxides are well known to act as catalyst supports and are usually obtained by being calcined at elevated temperature, which is regarded as an important factor for the high catalyst activity.[20]

However, calcining the support at elevated temperatures (ranging from approximately 130 °C – 500 °C) to form the oxide is a very time and energy consuming process which releases polluted gases, such as NO*x*, HCl, etc. Several papers have reported that noble metal catalysts prepared by co-precipitation of the noble metal with the support metal and then calcining the resultant precipitated catalyst at relatively mild temperature (ranging from approximately 50 °C – 130 °C) were more active than those calcined at elevated temperatures with some minor exceptions.[21] [22] [23] [24] [25] [26] It has been found that ferric oxide and manganese oxide supported gold catalysts prepared by co-precipitation which was only dried at about 100°C without being calcined showed higher catalytic activity during CO oxidation at 120 °C.[27] [28]

Co-precipitation has been employed to prepare highly active supported gold catalysts, in which chloroauric acid was used as precursor to form appropriate nano-Au metal particles. Even the use of ferric hydroxide to support the noble metal catalyst which is prepared by co-precipitation without calcining possessed better catalytic performance than that of the corresponding catalyst calcined at elevated temperatures. [29] [30]

2.5 Application of mono metallic catalysts

The most widely used supported catalysts in the industry are of mono metallic nature.[31] This implies that there is only one kind of active species supported. For example Fe_2O_3/zeolite,[32] where the Fe_2O_3 is the active species however Pt/FeO_x is also a mono-metallic catalyst in this case, the platinum is the active species and the iron oxide is the support and is does not partake during the catalytic process.

Ferrite particles in the nano-size range have attracted much attention due to their technological applications in disk and digital tape recordings as well as magnetic refrigeration. Methanol have been considered to become one of the more favourable liquid energy carriers due to the fact that it can be synthesized from coal, biomass as well as natural gas. Synthesis gas and hydrogen can be obtained from the decomposition of methanol, which in turn can be used for other chemical processes. The decomposition of methanol reaction is an endothermic reaction, and can thus also be utilized for chemical storage of heat. The decomposition of methanol can produce methane and/or carbon monoxide/carbon dioxide. When an iron catalyst, prepared by co-precipitation, was compared with a mixed catalyst (mixed with cobalt) it was shown that there exists a significant difference in the selectivity during in the decomposition of methanol reaction towards CO and methane. It was found that when cobalt was present the reaction selectively leaned towards the formation of CO.[33]

When one is considering the other side of the above mentioned decomposition of methanol reaction, there is also the possibility of reforming reactions of, for instance, methane to produce synthesis gas and hydrogen. During this reaction, monometallic nickel-based catalysts can possibly be used. These catalysts can be prepared by co-precipitation and reduced at temperatures below 600 °C if necessary.[34]

Another example that can be considered is the decomposition reaction of methane using nickel, cobalt and iron based monometallic catalysts. This reaction produces CO_x free hydrogen and nano-carbon. During a study it was shown that these catalysts have high thermal stability and starts to decompose from 500 °C to 700 °C. However, the catalytic material was not prepared by co-precipitation, but by impregnation. Comparing the results led to a conclusion that nickel based catalysts produced high hydrogen yield (74 %) but had low catalytic stability. Cobalt and iron based catalysts showed relative low hydrogen yield (43 % and 46 % respectively) but maintained high catalytic stability.[35]

2.6 Bimetallic catalysts

In the chemical industry, numerous monometallic catalysts utilized during chemical processes have been replaced by bimetallic catalysts to enhance the catalytic performance thereof, especially in the field of hydrogenation.[36] Bimetallic catalysts can be prepared by co-impregnation. It is difficult to

selectively prepare bimetallic particles in the original meaning of the word. It sometimes occur that the prepared material consists of a mixture of two separate monometallic particles as well as bimetallic particles.[37, 38] Bimetallic catalysts often show electronic and chemical properties that are unique as from those of the metals they originated from individually. Bimetallic catalysts gained considerable interest for their use in hydrocarbon reforming. During the abovementioned hydrocarbon reforming reactions, greater activities than those of monometallic catalysts are exhibited. The study of bimetallic surfaces in the field of catalysis has gained considerable interest due to the fact that it is difficult to determine, theoretically, whether the electronic and chemical properties of a particular bimetallic catalyst surface will be modified relative to metals it originated from.[39]

When considering the modification of chemical and electronic properties of the metal surface in a bimetallic compound, two factors are deemed important. When heteroatom bonds are formed, the electronic environment changes at the metal surface. This gives rise to a modification of the electronic structure of the compound (through the ligand effect). Secondly, the geometry of the bimetallic structure is different from that of the original metal. Meaning, the average metal-to-metal bond lengths change. This results in the strain effect that modifies the electronic structure of the metal *via* changes in the orbital overlap.[39, 40]

An interesting fact regarding bimetallic catalysts is that one of the metals can alter the catalytic properties of the other metal as a result of both electronic and structural effects. Using different preparation methods of supported bimetallic catalysts (by deposition or precipitation) may lead to a catalyst with new characteristics, where some specific interaction between the two metals could produce a type of “hybrid” catalyst that can exhibit catalytic behavior that will be different from that of other catalysts that have been prepared by more conventional methods.[6]

Catalysts containing bimetallic clusters can be prepared by mixing a suitable support (alumina, silica etc.) with an aqueous solution of precursors of the two metals of interest. The catalytic material must then be dried and combined with a stream of hydrogen gas at a high enough temperature to ensure the metal precursors are reduced. The reduction reaction yields a bimetallic cluster that is dispersed on the support/carrier component.[41] Nowadays characterisation of bimetallic catalytic materials includes techniques such as X-ray photoelectron spectroscopy (XPS), transmission electron microscopy (TEM) etc.[36, 51]

Bimetallic clusters are a class of the larger group of bimetal compounds, which are defined as a combination of two different metal which is not necessarily in their metallic state. Bimetallic compounds can either be oxides of the two metals or the two metals can have an organic ligand attached to it (most probably linking the two metals together).[44, 45]

In explanation of the nature of a bimetallic catalyst, there are three basic types:

1. Alloy of two metals ($M_xM'_y$):

   For example, Ru_6Pd_6, Ru_6Sn, $Ru_{10}Pt_2$ or $Ru_{12}Ag_4$, prepared by either precipitation or wet impregnation which could be used to catalyze hydrogenation reactions at low temperatures such as the hydrogenation of polyenes, dimethyl terephthalate and/or benzoic acid (see **Scheme 2.1**).[42, 43]

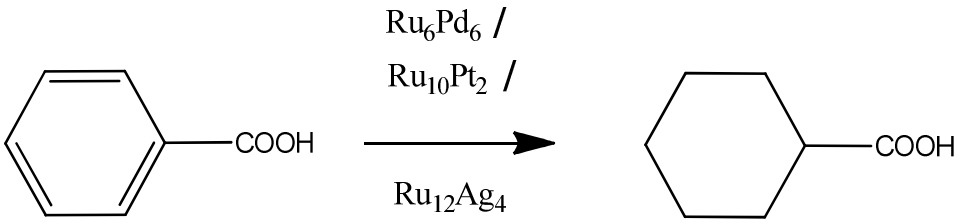

Scheme 2.1: Hydrogenation of Benzoic acid to cyclohexanecarboxylic acid.

2. Dinuclear catalysts (one metal complex containing two metal nuclei):[44]

   A dinuclear compound can be considered as a complex that contain two metals in close proximity i.e. where two of the same metal is held together by a one ligand. These bimetal compounds are well-known for their homogeneous catalytic acitivity, such as enzyme catalysed processes. It has also been shown the ability to catalyze a hydration/hydrolysis reaction of acetonitrile (see **Scheme 2.2**).[42, 43] Catalyst precusors also exist where two different metals are in the same molecule for example $[Rh(FcCOCHCOCH_3)(CO)_2]$ [45] or $[Rh(FcCOCHCOCH_3)(CO)(PPh_3)]$.[46] In the former case the iron forms part of the ligand attached to the rhodium. However, compounds where two different metals are held together by organic ligands are also known for example bimetal carboxylate compounds like Pd-Co-acetate.[47]

   $[Rh(FcCOCHCOCH_3)(CO)_2]$ has been used for oxidative addition, which is the first step of the Monsanto process. Bimetal acetates are useful for the oxidation of alcohols.[45]

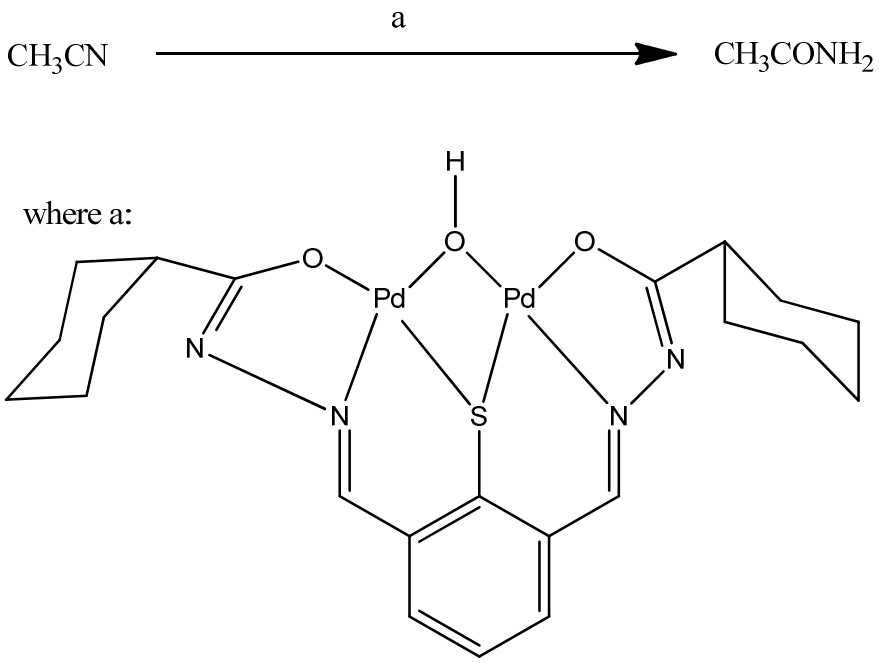

Scheme 2.2: Hydration of acetonitrile catalysed by (a) a dinuclear palladium complex.

3. Two-component catalyst (no interaction before reaction):
   For example the homogeneous mixture of two catalyst compounds i.e. $PdCl_2(PCy)_2$ and $Co_2(CO)_8$ have been used for the heterogeneously catalysed hydrogenation of triple bonds.

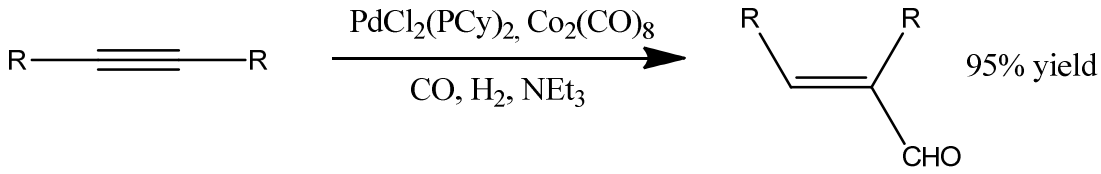

Scheme 2.3: Hydroformulation reaction of acetylene to produce an α, β-unsaturated aldehyde where R = C_3H_7.

When two-component catalysts are used, a second catalyst is needed to activate the main catalyst when the mixing takes place and the activated catalyst delivers higher catalytic activity as well as can give better selectivity. Without the second catalyst to activate the first catalyst, the yield as well as selectivity can be affected. [48]

Cross coupling reactions can successfully be catalysed by bimetallic catalysts. One such report was the Suzuki-Miyaura couplings of aryl bromides and chlorides with aryl boronic acid catalysed by Cu-Ni/C bimetallic catalysts as well as the heterogeneous reductions of aromatic chlorides. [49] Bimetallic catalysts can obtain improved performances in catalysis with respect to activity and selectivity related to hydrogen production, and show different structures (see **Figure 2.1**) according to the metals' properties, support interactions, atmosphere temperature etc. [50]

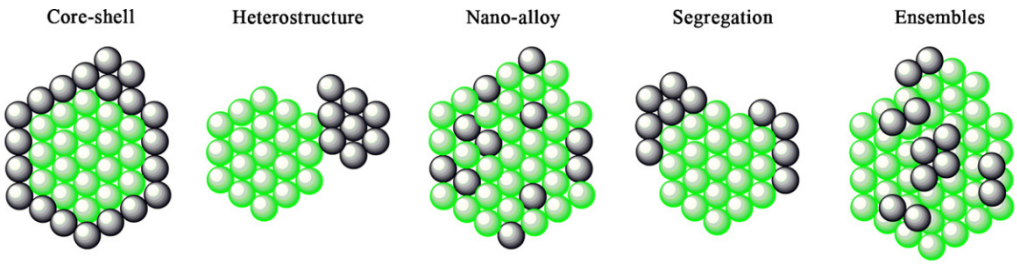

Figure 2.1: Different structure of a bimetallic catalyst. Reprinted (adapted) with permission from V. Dal Santo, A. Gallo, A. Naldoni, M. Guidotti and R. Psaro, *Catalysis Today*, 2012, **197**, 190-205. Copyright, 2016, Elsevier.

The platinum surface sites can be altered in bimetallic alloys, such as platinum-gold. In some cases it is possible that the composition of the surface of an alloy may be different from that of the bulk material. Separation of a component in bimetallic material, for instance the component responsible for the low melting point, has been shown to decrease the surface energy. There are other factors such as the preparation method and metal particle size that may also be responsible for the differences in the structure and composition of bimetallic surface sites. These sites can be used to determine the catalytic behaviour of a prepared catalyst. One difficulty that rises during the preparation of a bimetallic catalyst is the ability to bring two metals into close proximity. The co-impregnation method has shown failed attempts and it became necessary to develop new techniques. One bridging argument is to alter an existing monometallic catalyst by adding a second metal in order to promote metal-metal interactions. The second metal can be deposited by the use of a reaction that occurs on the monometallic particles. These particles are initially present on the support.[51]

During the preparation of supported bimetallic catalysts it is important to consider two aspects, firstly, how a stable close proximity can be created between two metals. Secondly, how surface reactions can be controlled that are responsible for bimetallic surface entities that are formed. When bimetallic catalysts are designed it is important to consider the reaction mechanism it is being designed for as well as the role the different types of active sites play in a catalytic reaction. An example of this is a supported bifunctional catalysts containing tin and platinum. During this study an anchoring reaction at 40 °C of tin resulted in a catalyst formation that was exclusively of an alloy type (Pt-Sn/Al_2O_3). However, tin was able to be introduced on an alumina support at higher temperatures. This catalyst has been considered to be of great industrial importance, especially in the field of fine chemistry, dehydrogenation processes and refinery technologies.[52]

For industrial applications of bimetallic catalysts, the catalytic material must be prepared to possess high surface area and it must have some resistance to the loss of surface area after it has been used. Dispersing it on a carrier provides an effective solution. The resulting catalyst is called a “bimetallic cluster” rather than an alloy, since the systems of interest include metallic combinations which do not form alloys in bulk.[53] One of the applications of these bimetallic catalysts is the nitrate concentration

reduction in drinking water. Bimetallic palladium catalysts are used to convert nitrate containing compounds in drinking water into harmless derivatives and removed.[54]

2.7 Metal Hexacyanometallates

A cyanometallate is a coordination compound, where one or more cyanide ligand is coordinated to a metal center. The cyanide ligands are considered to be ambidentate ligands with their ionic -1 charge. These cyanide ligands are small considering they only consists of one carbon atom and one nitrogen atom, thus it is easy to consider it may have a tendency to saturate the entire coordination sphere of the metal ion. Prussian blue exhibits an empirical formula of $Fe_4[Fe(CN)_6]_3$, this corresponds to a lattice structure that shows hexacoordinate, low-spin Fe(II) atoms that are bonded *via* the carbon atoms as well as hexacoordinate, high spin Fe(III) atoms that are bonded via the nitrogen atoms of the cyanide ligands (Fe^{II}-C≡N-Fe^{III}). Varying the oxidation states of the Fe atoms at different sites on the cubic structure gives different coordination compounds with different colour properties. With linkage isomerism it is also possible to vary the metal atoms that bond *via* the nitrogen bonds to other metals such as chromium, cobalt, nickel and copper.[55]

Metal hexacyanometallates has a general formula of $A_xM_y[B(CN)_6]\cdot nH_2O$ where *M* and *B* are transition metals (Fe, Co, Ni and/or Cu), *A* an alkaline metal such as potassium, *x* and *y* stoichiometric coefficients, *n* the hydration-intercalation molecules per unit formula.[56] They are also referred to as coordination polymers and are very useful and versatile due to the mixed valency of the metals.

These metal hexacyanometallates have a zeolite-like three-dimensional structure, with a cyano-bridge connecting the two different metals, creating a face-centered cubic unit cell (see **Figure 2.2**) and depending on the degree of peptization, can be described in the soluble and insoluble form.[57, 58] These metal hexacyanometallates can be prepared in bulk or different nano-sizes depending on the experimental conditions used. The shape of these nano-sized metal hexacyanometallates can be manipulated by changing the synthesis conditions.[65]

Metal-hexacyanoferrates have exceptional technological potential for their electrochromic, electrocatalytic, ion- exchanging, ion-sensing and photomagnetic properties as well as for their possible applications in charge-storage devices such as rechargeable batteries.[56]

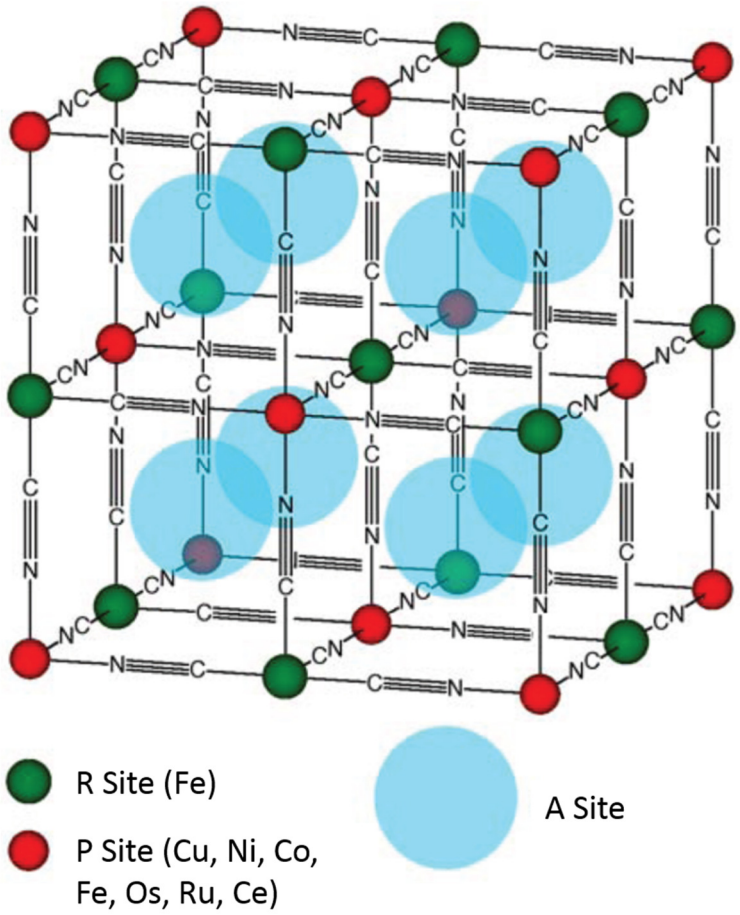

Figure 2.2: The unit cell of metal hexacyanoferrate (MHCF) exhibiting the framework of hexacyanoferrate groups with R, P and A sites. Site A represents the interstitial sites.[59] Reprinted (adapted) with permission from C. D. Wessells, M. T. McDowell, S. V. Peddada, M. Pasta, R. A. Huggins and Y. Cui, *Am. Chem. Soc.*, 2012, **2**, 1688-1689. Copyright, 2012, American Chemical Society.

As can be seen from the structure in **Figure 2.2** the material forms a three dimensional lattice structure that continues until the reagents are depleted.

2.7.1 Synthesis of Metal Hexacyanoferrates

Metal-hexacyanoferrates (MHCFs) are prepared by oxidation of ferricyanide $[Fe^{II}(CN)_6]^{4-}$ to ferrocyanide $[Fe^{III}(CN)_6]^{3-}$ in the presence of a metal(II) salt. For example Prussian blue is prepared by reaction of an iron(II) salt and a ferricyanide salt.[60]

$$4Fe^{3+} + 3[Fe^{II}(CN)_6]^{4-} \longrightarrow Fe^{III}[Fe^{III}Fe^{II}(CN)_6]_3$$

During the preparation of Prussian blue the slow photoreduction of $[Fe(C_2O_4)_3]^{3-}$ is used to produce Fe(II) ions that subsequently reacts with $[Fe(CN)_6]^{3-}$ ions to generate nuclei and clusters of Prussian blue ($[MFe^{III}\{Fe^{II}(CN)_6\}]$ (M=Li, Na, K, NH_4)) encapsulated within water droplets.[61] Growth of the molecular magnet occurs by further exchange and fusion between microemulsion droplets to produce nanoparticles encapsulated in a shell of surfactant molecules. [61]

2.7.1.1 Bulk material

The preparation reaction used in the formation of bulk-sized MHCF is a relatively easy and common precipitation reaction. Two aqueous solutions are prepared. The first aqueous solution consists of a metal nitrate, -chloride or -acetate, which is added dropwise to the second aqueous solution of $K_3[Fe(CN)_6]$. The precipitation occurs instantaneous upon mixing.

This preparation can be accomplished near room temperature from readily available (earth-abundant) materials. An advantage of this preparation procedure is that it operates in low-cost aqueous media. This easy and inexpensive preparation makes it attractive for large scale production for use as energy storage.[21, 59]

2.7.1.2 Nanoparticles

Nanoparticles with a defined geometry render some advantages in comparison to bulk materials due to the high ratio of surface-to-volume it presents. During the preparation of nanoparticles it is important to ensure that well dispersed nanoparticles are indeed prepared that possesses a uniform size and well-defined shape. It has been suggested that when one wants to ensure that the catalytic material is synthesized in nano form, the growth of metal coordination polymers must be controlled under special confinement conditions.[62] The reactions used in preparing the nano MHCF is, similar to the bulk-sized MHCF, normally a co-precipitation, however, the formation of the particle are either facilitated or the nano-particles formed are stabilised by some additive. It can also be prepared by different techniques in sol-gel or using surfactants (see **Figure 2.3**) and capping-agents, which stabilizes the nanoparticles. [59]

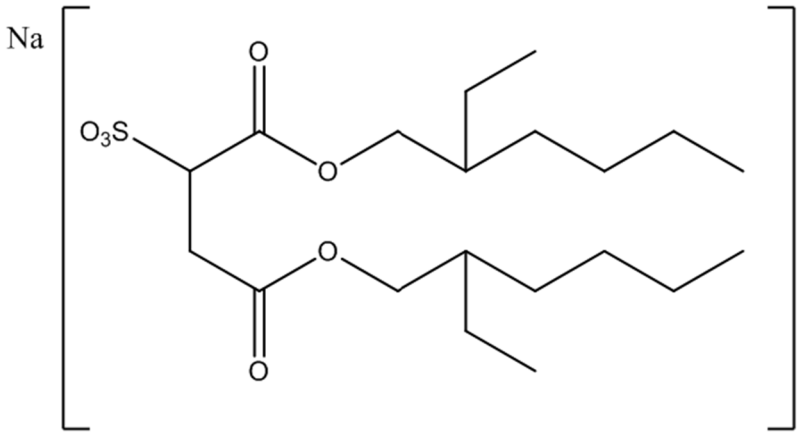

Figure 2.3: Structure of sodium Aerosol-OT (AOT), a surfactant material used to stabilize the preparation of nano-sized hexacyanoferrates. [63]

Reverse microemulsions, needed for the preparation of nano-sized metal hexacyanoferrates, formed by cetyltrimetyl ammonium ferrocyanide (*CTAFeII*), the functionalised surfactant, can be used as reaction media to prepare metal hexacyanoferrates. Spherical nanoparticles of NiHCF, CoHCF FeHCF and CuHCF (with sizes ranging from 4 nm to 6 nm) can be obtained simply by adding diluted solutions of $NiCl_2$, $CoCl_2$, $FeCl_3$ or $CuCl_2$ to the reverse microemulsions. These compounds exhibit interesting physiochemical properties such as electrochromism, photoelectrochromism, electrolytic, energy storage and sensing properties.[64]

In the early development of MHCF nano particles, reverse microemulsion (RME) systems were used that was formed by sodium bis-(2-ethylhexyl) sulfosuccinate (the surfactant, NaAOT, see **Figure 2.3** for the structure) as well as its functionalized forms, including but not limited to, $Cu(AOT)_2$ and $Co(AOT)_2$ respectively. These RME systems are transparent, thermodynamically stable, homogeneous dispersions of two immiscible liquids that are stabilized by a large amount of the surfactant. Preparation of nanoparticles *via* the use of RME method is advantageous due to the fact that not only does it produce nanoparticles with narrow size distribution, but also with the ability of controlling the particle size by simply varying one or more of the methods parameters such as droplet size, reactant concentration, etc. The use of *CTAFeII* not only makes the synthesis/preparation of different MHCF nanoparticles more convenient, but also enables the practicality of using functionalized cationic surfactants to obtain nanoparticles of other coordination compounds.[64]

It has been shown that a RME system, formed by mixing two cationic surfactants (cetyltrimetyl ammonium bromide (*CTAB*) and, its functionalized form cetyltrimetyl ammonium ferrocyanide (*CTAFeII*)) and *n*-butanol as co-surfactant in *n*-hexane or water was found to be a good method to prepare NiHCF nanoparticles. *CTAFeII* can be obtained by exchanging bromide ions (Br^-) of *CTAB* by ferrocyanide ions ($[Fe(CN)_6^{4-}$) followed by a metathesis reaction. NiHCF nanoparticles can then be

prepared by adding a diluted solution of $NiCl_2$. It needs mentioning that the most important advantage of this preparation method over those formed by $M(AOT)_2$ surfactant, is the possibility to prepare different MHCF by simply adding different salt solutions to the RME.[64] However, the AOT surfactant method has shown impressive nano-particles formation and assembling (see **Figure 2.4**). [65]

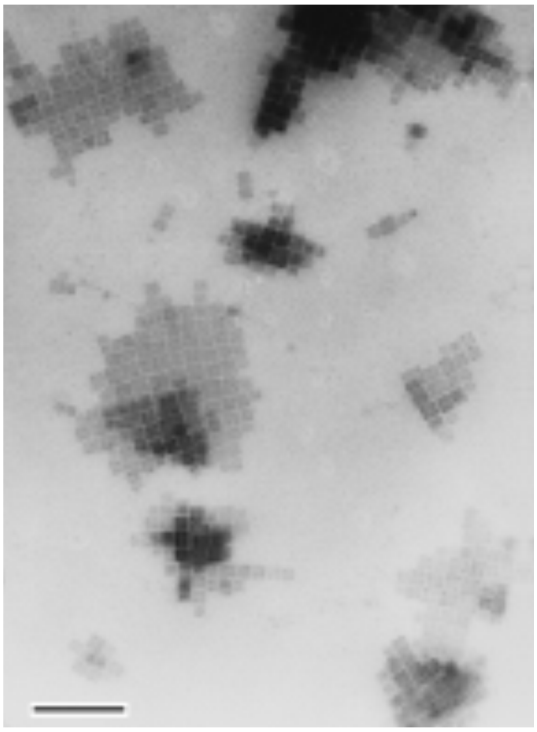

Figure 2.4: TEM image of cubic Prussian blue nanoparticles formed in AOT microemulsions. Showing self-assembling in 2-D and 3-D superlattices. (scale bar 100nm). Reprinted (adapted) with permission from *S*. Vaucher, M. Li and S. Mann, *Aangewandte Chemie International Edition*, 2000, **39**, 1793. Copyright, 2000, John Wiley and Sons.

Another study showed that nano-particles (20 nm – 50 nm in size) can be prepared by co-precipitation with no mention of using any surfactant (See **Figure 2.5**).[59] Nano-sized NiHCF can be prepared by a precipitation reaction where ethylenediaminetetraacetic acid (EDTA) is used as surfactant (see **Figure 2.6**).[57]

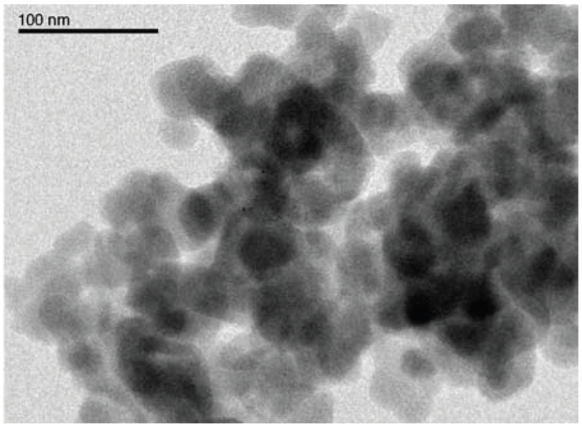

Figure 2.5: TEM image of CuNiHCF revealing that it is composed of agglomerations of 20-50nm particles. [59] Reprinted (adapted) with permission from C. D. Wessells, M. T. McDowell, S. V. Peddada, M. Pasta, R. A. Huggins and Y. Cui, *Am. Chem. Soc.,* 2012, **2**, 1688-1689. Copyright, 2012, American Chemical Societ.

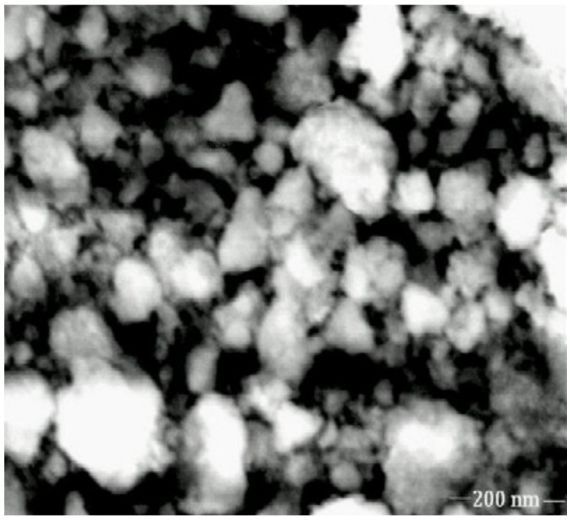

Figure 2.6: FE-SEM image of NiHCF nanoparticles prepared by precipitation and using EDTA as surfactant.[57] Reprinted (adapted) with permission from S. R. Ali, P. Chandra, M. Latwal, S. K. Jain, V. K. Bansal and S. P. Singh, *Chin. J. Catal.*, 2011, **32**, 1844. Copyright, 2011, Elsevier of Chinese Journal of Catalysis.

Reaction media that is confined, such as microemulsions, can constrain the growth of the crystal processes on a spatial level within length scales in the range of a few tens of nanometres. However, this method can also be used to prepare nano-particles with uniform shape and size. This method has been applied in the preparation of Prussian blue nanoparticles that exhibit cubic shape and monodisperse size. This is achieved by utilizing exchange reactions within the water droplets of two reverse microemulsions that are prepared in isooctane using the AOT surfactant. In general, one of the microemulsions contain a dissolved precursor of the transition metal, while the second microemulsionan contains an aqueous solution of the hexacyanometallate. [61, 65]

Morphosynthesis is a preparation method where chemically based strategies are developed with the intention to control the size, shape and organization of particles that stretches beyond the unit cell's length. The physical properties of hexacyanoferrates are inherently dependant on the relationship between the molecular building blocks, which has progressed significantly in crystal engineering as well as the well-grounded design of constructional patterns by customising the unit cell. The aim of these morphosynthetic strategies is to conquer a multilevel organisation of nano particles spontaneously *via* pure chemical process.[61]

The growth of nanoparticles within the restricted reaction field progresses in sequential stages:[61]

- Firstly, water droplets from both miroemulsions collide to produce particles with sizes smaller than 5 nm in the micelles.
- Stable suspensions of nano-particles (with uniform size of about 5 -50 nm and cubic shape) are formed *via* further crystallisation and inter-droplet exchange.

The second step accounts for the observation that the size of the nano-particles is, to some extent, independent of the water droplet size in the microemulsion. On the contrary, the size of the nano-particles depend linearly on the concentration of the reactants in the water droplets. This is consistent with a nucleation-controlled process. The spontaneous self-assembling of the nano-particles into supperlattice can be derived due to the interaction of the exposed hydrophobic tails of the capping surfactant (see **Figure 2.7** and **Figure 2.8** for TEM images).[61]

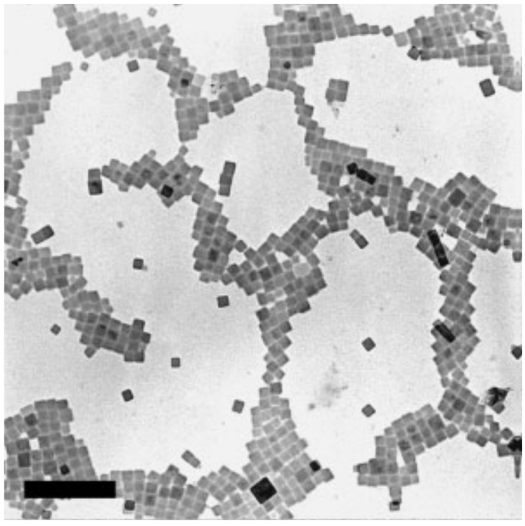

Figure 2.7: Prussian blue analogue nanoparticles with cubic shapes self-assembling into supperlattice. Scale bar = 200 nm. [61] Reprinted (adapted) with permission from E. Dujardin and S. Mann*, Adv. Mater., 2004, **16(13)**, 1125-1126.* Copyright, 2004, John Wiley and Sons.

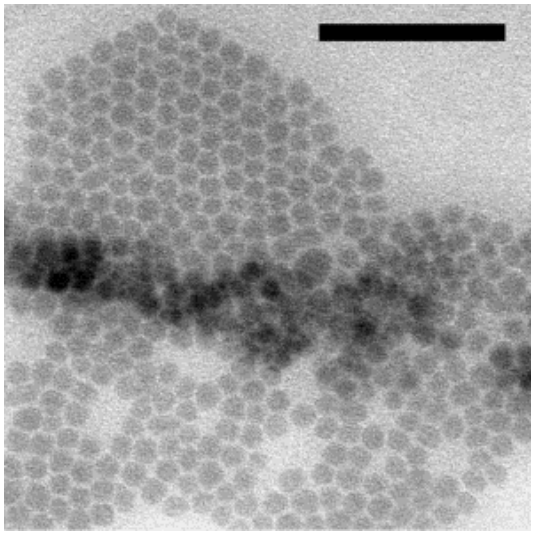

Figure 2.8: Prussian blue analogue nanoparticles with spheroidal shapes self-assembling into supperlattice. Scale bar = 200 nm. [61] Reprinted (adapted) with permission from E. Dujardin and S. Mann, *Adv. Mater.*, 2004, **16(13)**, 1125-1126. Copyright, 2004, John Wiley and Sons.

2.7.2 Properties of MHCF

Nanomaterials of MHCMs usually exhibit multiple enhanced properties such as magnetic, electrical, surface, optical, catalytic, electrochemical, chemical and biological activities. Among other inorganic materials, transition MHCFs have undergone intensive study due to their exceptional characteristics such as mixed valency, water insolubility, high ionic conductivity as well as showing exceptional redox mediator properties. [62] They also possess ion-exchange and charge storage properties.[66]

As mentioned earlier most MHCFs possess a microporous, multinuclear, open channel structure. These MHCF complexes are not dissolved upon oxidation or reduction. This is due to the fact that their zeolitic structure only allows the diffusion of ions in or out with maintaining electrical charge neutrality.[62]

These characteristic properties of MHCF make them extremely useful in the preparation of molecular magnets, photomagnets, ferromagnets, optical devices, rechargeable solid state batteries, electrochromic devices, adsorbents, ion-exchangers and catalysts.[57]

2.7.2.1 Electrochemistry

This section contains a short description of the electroanalytical techniques to be performed in this study.

Cyclic voltammetry (CV) is an electrochemical technique that studies the redox behaviour of a given compound. This method measures the current as a function of applied potential. It can also be seen as the measurement of the current in an electrochemical cell under conditions of complete concentration polarization in which the rate of oxidation or reduction of the analyte is limited by the mass transfer rate of the analyte to the electrode surface. When CV experiments are performed, quantitative data is obtained that provides significant information regarding the redox properties of the relevant compound. During such an experiment the potential of an electrode, which is immersed in an unstirred solution, is cycled while the current is measured. The potential of the above mentioned working electrode is controlled against a reference electrode (silver/silver chloride or saturated calomel electrode). This method uses a triangular voltage input that yields forward and reverse scans. The potential cycles back to the potential that was initially used to start the experiment. A typical cyclic voltammogram (see **Figure 2.9**) provides information regarding the positions of peak anodic potential (E_{pa}), peak cathodic potential (E_{pc}), peak anodic current (i_{pa}) and peak cathodic current (i_{pc}).[67, 68]

The significant experimental data that is obtained provides the following information:[69, 70]

- The formal reduction potential is calucalted as the average between the peak anodic potential (E_{pa}) and the peak cathodic potential (E_{pa}), see equation [1] below.
- The peak separation (ΔE_p, see equation [2]) is used to determine the electrochemical reversibility of the analyte. A redox couple is considered to be electrochemical reversible if the peak separation is 90 mV > ΔE_p at 25 °C for a single electron transfer process (the theoretical value is 59 mV). The electrochemical process is considered to be electrochemically quasi-reversible if the peak separation is 90 mV ≤ ΔE_p ≥ 150 mV. If the peak separation is determined to be ΔE_p > 150 mV, the electrochemical process is considered to be irreversible.
- The current ratio (i_{pc}/i_{pa}, see equation [3]) is used to determine the chemical reversibility of the analyte. If a process consists of oxidation and reduction of the analyte the current ratio will be equal to 1, which implies that the process is chemically reversible.

The process is only considered electrochemical reversible if it is able to maintain an equilibrium of the oxidised and reduced species. This constitutes the NERNST equation (E, see equation [4]).

$$E^{\circ\prime} = (E_{pa} + E_{pc})/2 \quad [1]$$

$$\Delta E_p = E_{pa} - E_{pc} = 59/n \quad [2]$$

$$i_{pc}/i_{pa} = 1 \quad [3]$$

$$E = E^{\circ\prime} + \frac{RT}{nF} Ln \left(\frac{[oxidation]}{[reduction]}\right) \quad [4]$$

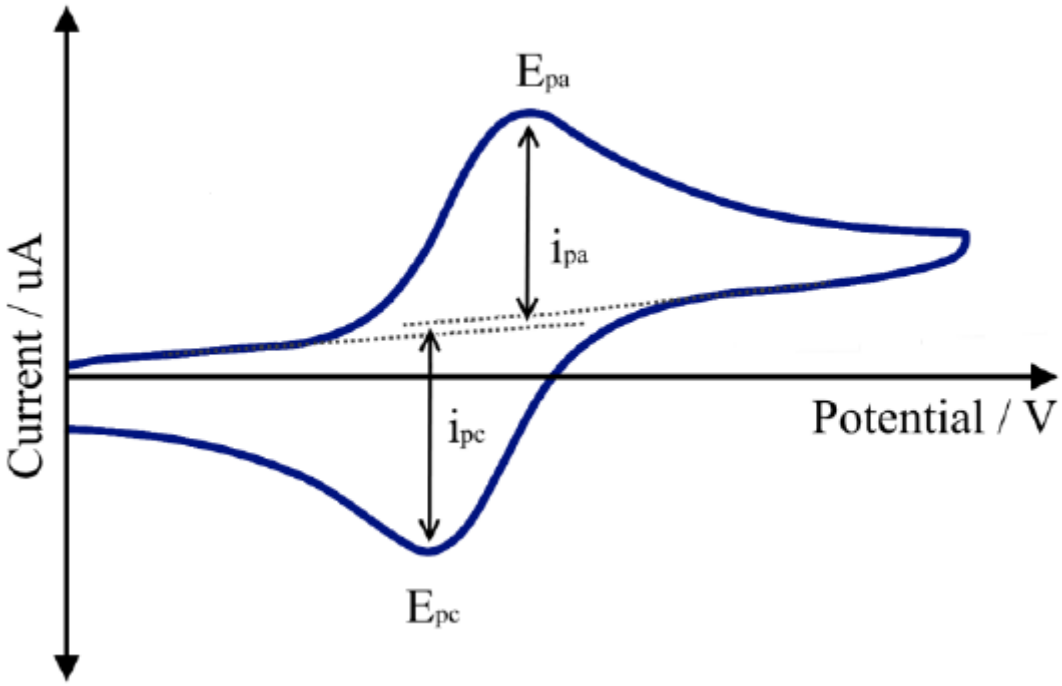

Figure 2.9: Explanatory cyclic voltammogram.[69] Reprinted (adapted) with permission from M. Govender, M. Sc. thesis, University of the Free State, 2015.

The electrochemistry of MHCMs have great significance for both fundamental research and practical application. In terms of fundamental research, since for example CoHCFs consists of multiple redox centers Co^{II}, Co^{III}, Fe^{II} and Fe^{III} in various stoichiometries, interesting electrochemical properties are expected. For practical application the electrochemistry is useful in biosensing, electrocatalysis, ion-exchange and charge storage capabilities (which will be discussed later).[66]

Considering that MHCMs are insoluble, normal solution electrochemistry cannot be conducted on these complexes. There are however two methods that can be employed to electrochemically characterise these MHCMs. The first involves the electrodeposition of the MHCMs, similar to electroplating of the MHCMs from a solution containing the starting materials of the MHCMs, and the second method is the physical coating of the electrode surface with the already formed MHCMs. Both these methods thus involve solid-state electrochemistry.

Different ways to modify the electrode surface with these compounds have been explored. Traditionally, the surface of a conductive substrate is immersed in a solution containing the hexacyanoferrates and other transition metal ions. The mixture is cycled over a range of potentials whereby the electrode is modified *via* electrochemical reaction.[71]

There has been a great amount of papers reporting on the preparation of CoHCF (cobalt hexacyanoferrate) nanoparticles by electrochemical modification of the electrode surface, such as carbon nanotubes or nanowires, by synthesis in reversed micelles or water-in-oil microemulsions.[72]

During the cycling of the potential in a typical cyclic voltammetry (CV) experiment of a solution containing a metal salt like $CoCl_2$ and the hexacyanometallate $K_3[Fe(CN)_6]$, the electro surface gets modified by electrodepositioning of cobalt hexacyanoferratte.[73] In a typical electrochemical response of this modified electrode, the electrochemical processes of both metals can be detected, giving the opportunity to investigate the electrochemical characteristic of these MHCMs.

During the reversible electrochemical cycling of these MHCM-modified electrodes, alkaline ions are inserted or removed from the A sites (see **Figure 2.2**), with a corresponding change in the valence of either the P or R site ion. **Figure 2.10** shows the Fe^{II}/Fe^{III} couple during a CV experiment of a CoHCF modified electrode. This redox reaction is accompanied by Na^+ ion movement in and out of the CoHCF framework. The symmetry is an indication of good reversibility of the redox process.

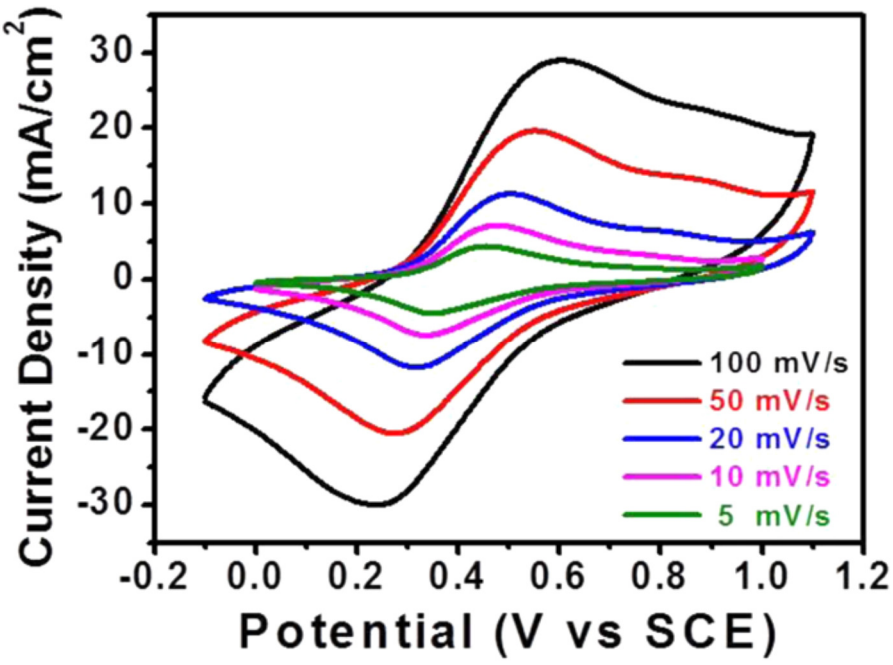

Figure 2.10: CV scans at different scan rates of CoHCF nanoparticles showing supercapacative performance. [74] Reprinted (adapted) with permission from F. Zhao, Y. Wang, X. Xu, Y. Liu, R. Song, G. Lu and Y. Li, *ACS Appl. Mater. Interfaces,* 2014, **6**, 11007 – 11012. Copyright. 2014. American Chemical Society.

A recent study found that the HCF group is electrochemically active for the intercalation of ions in both CuHCF and NiHCF, however the CuHCF exhibited a higher potential for intercalation activity than the NiHCF.[59] It has also been shown that the photoinduced magnetization and unique electrochromic properties of CoHCF are dependant not only on the oxidation states of the Co/Fe ions but also on the nature of the counter cations incorporated in the crystal structure during electroreduction

(intercalation).[74] These ions could be monovalent (Na^+, Li^+, K^+ and NH_4^+) and divalent ions (Mg^{2+}, Ca^{2+}, Sr^{2+} and Ba^{2+}).[75] The potential of the redox couple are also affected by the nature of the counter cations, which undergoes this intercalation process as well as the concentration of supporting electrolyte (see **Figure 2.11**).[66]

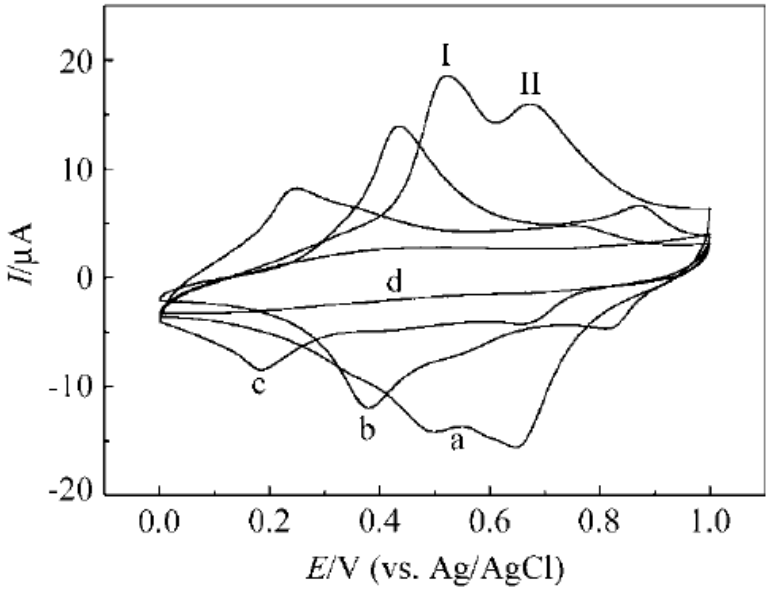

Figure 2.11: Cyclic voltammograms of nanosized CoHCF modified electrode in 0.1 mol/l in 0.1 mol•L－1 KCl (a), NaCl (b), LiCl (c) and NH_4Cl (d) supporting electrolyte solution at a scan rate of 40. Reprinted (adapted) with permission from L. Shi, T. Wu, M. Wang, D. Li, Y. Zhang and J. Li, *Chinese Journal of Chemistry*, 2005, **23**, 149 – 154.

An electrode modified by physically coating the surface of the electrode with already prepared nano-CoHCF revealed metal-to-metal charge transfer.[77] Since both Fe^{III} and Co^{III} are simultaneously present on the surface both redox couples can be detected. This electronic charge transfer occurs with a significant shortening of the Co-N bond length from 2.08 Å (Co^{II}(high spin)) to 1.91 Å (Co^{III}(low spin)) and with a significant shortening of the cell parameters from 10.3 Å to 9.96 Å, when the electronic switch is spread in a cooperative way in the solid.[76] A continuously cycling experiment of the CoHCF modified, revealed a progressive modification of the curve morphology, which was ascribed to the conversion of the starting nano-compound to a bulklike species (see **Figure 2.12**). The isoelectric point in the repeated cyclic voltammogram experiment represents a chemical cross-reaction of the substitution of some Co^{II} by Fe^{II}.[77]

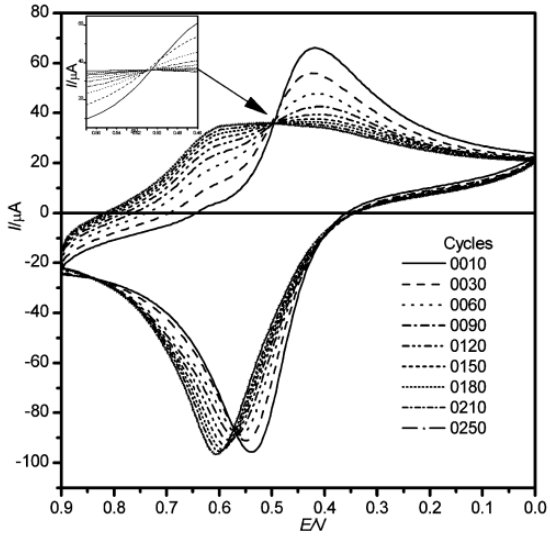

Figure 2.12: CV of the CoHCF physically coated onto an electrode, showing both redox processes for Fe and Co. Reprinted (adapted) with permission from A. Fitch and G. J. Edens, *J. Electroanal. Chem.* 1989, **267**, 1–13.

2.7.2.2 Magnetic properties

The relationship between the unit cell structure and magnetic properties have been studied extensively. However, not so much effort has gone into understanding the growth mechanism as well as controlling it. It has been shown that the growth of MHCFs can be controlled by a multistep process that involves the photoreduction of $[Fe(C_2O_4)_3]^{3-}$ that produces Fe^{2+} ions. These ions react with $[Fe(CN)_6]^{3-}$ to generate clusters as well as nuclei of Prussian blue that is encapsulated in the water droplets. Furthermore, growing of the molecular magnets occurs by exchange and fusion between the individual microemulsion droplets. This produces nanoparticles that are encapsulated in a shell of the surfactant molecules.[65] During the same study, it was shown that the formation/growth of the superlattice structure from the microemulsion reaction media, which was a mixture of iso-octane and water, was found to be time dependant. The great degree of order that is found in these preparations is a direct consequence of high concentration of the Prussian blue nanoparticles.[65] In addition, the size of each individual nanoparticle was found to be dependent on the concentrations of the precursors (ammonium iron(III) oxalate and ammonium ferricyanide) in solution as well as the photoreduction rates and ionic concentrations.[65]

Molecular magnetic material have received much attention due to the fact that they do not imitate conventional solid-state magnets, but rather offer opportunities to couple magnetism with the physical properties such as sensing and transduction. Magnetic nanoparticles have shown properties that are to be considered as intermediate between classic bulk magnetism and molecular-size paramagnetism. The ultimate magnetic systems are high-spin clusters and/or molecules, which have molecular structures

well-defined and comprise of a finite number of unit cells.[61] Thus understanding and controlling the growth mechanism of these magnetic coordination polymers is an important aspect in the study of molecular magnets due to the fact that compounds with feasible magnetic properties require further processing and fabrication if functional devices are to be produced.[65]

It has been shown that chromium hexacyanonickellate (Cr^{III}-CN-Ni^{II}) magnetic particles prepared by the reverse micelles technique leads to the formation of magnetic nanoparticles with a size distribution that is centered at 3 nm and possesses a spin state of ca. 130, which is a magnetic property value between that of magnetic clusters and metallic particles.[78] When these hexacyanonickellate magnetic particles are cooled, ferromagnetic exchange coupling interaction occurs, while at high temperature they behave like the bulk material. However, it has also been shown that there exists a divergence between the field-cooled and zero-field-cooled magnetization curves at 8 K, which is well below the Curie temperature (45 K). This indicates that the $Ni^{II}_3(Cr^{III}(CN)_6)_2$ nanocubes are single-domain superparamagnets exhibiting a blocking temperature of 5.5 K. This in turn corresponds with the maximum in the zero-field-cooled curve (see **Figure 2.13**). [61, 78]

Nanoparticles that possess magnetic moments between 100-1000 are needed to obtain an understanding of phenomena like quantum tunnelling and superparamagnetic blocking temperatures. However, at this stage their ground state magnetic moments remain small. Prepared magnetic MHCM nanoparticles can be used as the building blocks for the self-assembly of higher-order superstructures. The formation of magnetic nanoparticles that possess surface-attached ligands that are stabilizing of nature offer exceptional applications as ferrofluid materials.[61] For example, *p*-nitrobenzylpyridine can be used as a peripheral ligand to separate the particles from the micelle medium. The capped particles are dispersed in organic solvents which allows the study of the magnetic properties and/or behaviour in a diluted state. This opens the possibility to study and gain access to the properties of a single particle.[78]

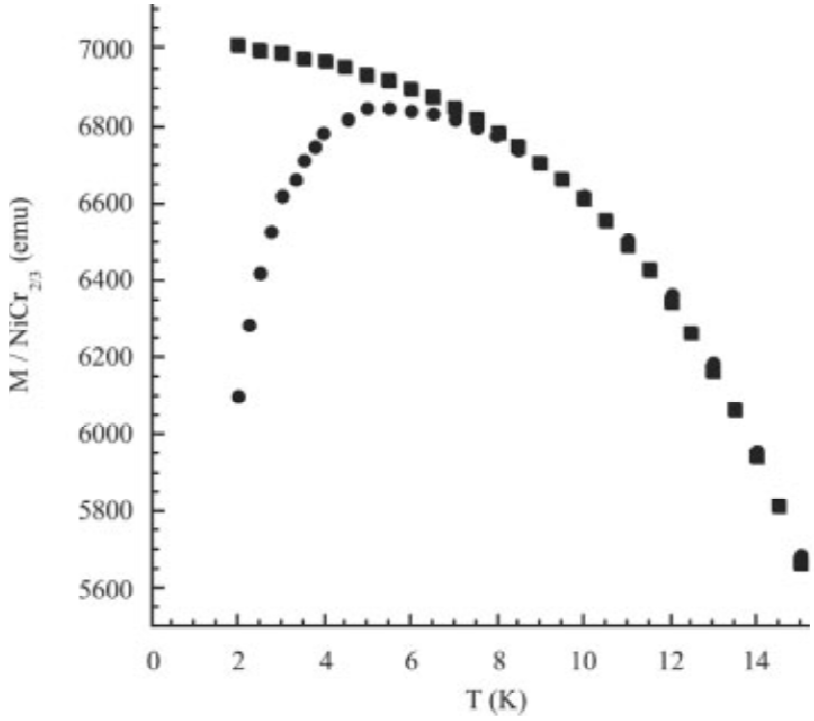

Figure 2.13: Field-cooled (black squares) and zero-field-cooled (black circles) magnetization curves with a 100 Oe direct current applied magnetic field for a non-diluted $Ni^{II}_3(Cr^{III}(CN)_6)_2$ nanocube sample.[78] Reprinted (adapted) with permission from L. Catala, T. Gacoin, J. P. Boilot, E. Riviere, C. Paulsen, E. Lhotel and T. Mallah, *Adv. Mater.* 2003, **15**, 826. Copyright. 2003. John Wiley and Sons.

In superparamagnetism, which is of technological and fundamental importance, the influence that the particle shape anisotropy exerts on the height of the energy barrier had to overcome thermal scrambling of the magnetic spins. MHCFs nanoparticles are highly anisotropic, this means that shape anisotropy has to be imposed externally. Preliminary magnetic measurements has shown that Prussian blue nano materials showed a Curie temperature (4.1 K) that is lower than in the bulk materials (5.6 K). This is possibly because of a curtailment of the average number of nearest neighbouring nanoparticles that is associated with the low dimensionality of the nanorods.[61]

2.7.2.3 Ion exchange

When spent nuclear fuel is discharged from a reactor, caesium and strontium are the primary sources of decay heat for about 50 to 100 years. These two fission products have half-lives of about 30 years. Disposing of these radionuclides in a safe and suitable manner, a method to separate ^{137}Cs and ^{90}Sr suitably, is necessary. NiHCF and KNiHCF have been considered to be selective ion exchangers for

Cs. It has been shown that potassium cobalt hexacyanoferrate (KCoHCF) as ion exchanger proved chemical stability in nitric acid solutions of pH = 1, as well as favourable selective uptake for Cs ions over Sr and Na ions. It was shown that the ion exchange capacity for Cs ions obtained, for a binary system was found to be 1.72 meq/g.[79]

Potassium nickel hexacyanoferrate (KNiHCF) is currently being employed on an industrial scale for the removal of caesium from radioactive liquid waste. Hydrated ions such as Cs^+ can penetrate the small channels in the crystal lattice of KNiHCF with diameters of approximately 0.32 nm, whereas larger hydrated ions such as Na^+ are blocked.[80] Nickel-, copper-, cobalt-, cadmium- and other MHCFs have been proposed as the selective and effective instrument for the recovery of precious metals such as silver. It has also been applied for the removal of hazardous cations, radioactive caesium, palladium, lead and strontium from the waste water of metallurgical plants.[62]

2.7.2.4 X-ray Photoelectron Spectroscopy [81]

The X-ray Photoelectron Spectroscopy (XPS) technique is based on the photoelectric effect. A sample that is irradiated with light of sufficient small wavelength emits electrons. The kinetic energy of these ejected electrons (either the core or valence electrons) are measured and converted to binding energy, which is related to the specific element. Each element has a unique set of binding energies (for each orbital) associated with it. Variations in the binding energies of a specific element arise from differences in the chemical and electronic environments. This can be used to identify the chemical state of the element and its chemical environment. During XPS analysis, the intensity of photoelectrons N(E) as a function of their kinetic energy is measured. The XPS spectrum, however, is usually a plot of N(E) vs E_b (binding energy).

The splitting of the photoelectron lines present on an XPS spectrum are a results of spin-orbit splitting. Seeing as electrons in the s-orbital have an orbital momentum of zero, electrons ejected from an s-orbital will show as a single peak on the XPS spectrum. All other orbitals (p, d and f) have orbital momentum higher than zero and due to spin being either up (s = +½) or down (s = -½), photoelectron lines generated from these orbitals display splitting into two peaks on the XPS spectra. The intensity of the ratios of the two peaks of a spin-orbit doublet is determined by its multiplicity (2j + 1). For $p_{1/2}$ and $p_{3/2}$, j is equal to 1/2 and 3/2 respectively, thus the ratio is 1:2, implying that $p_{1/2}$ is 50% of $p_{3/2}$. Similarly $d_{3/2}$ is 66% of $d_{5/3}$ and $f_{5/2}$ is 75% of $f_{7/2}$.

Not all photoelectric processes are simple, sometimes an extra peak appears or the main peak is asymmetric, with a tail to the higher binding energy side. This phenomenon is called shake-up and usually occurs in transition metals.

Although XPS is a surface characterisation technique it could be used with great efficiency to determine to ratio of elements as well as their oxidation state. This is demonstrated in a previous work where the

different iron binding energies were measured and compared to a similar adsorbed species on an electrode. It was concluded that the adsorbed species can be described as the "soluble form" of iron hexacyanoferrate, which was found to be bound to the electrode surface through the nitrogen of the cyanide group. It became evident that the presence of a higher binding energy peak was due to the nitrogen of the adsorbed iron hexacyanoferrate in the XPS.[82]

2.7.3 Applications

MHCMs have the practicability to accommodate various transition metal cations in the coordination framework, rendering them with captivating electrochemical, electric, magnetic, optical, surface, chemical, catalytic, sensing, ion-exchange, and/or photomagnetic properties. These enhanced properties of nano-MHCM have made them very useful in potential applications in various interdisciplinary areas including biological diagnosis, electrochemistry, biomedicine, controlled drug delivery, enzyme immobilization, biosensing, magnetic resonance imaging and magnetic memory devices.[62]

2.7.3.1 Energy storage

Prussian blue and related metal hexacyanoferrate salts constitute a class of zeolitic mixed-valence compounds that have been investigated for their electrocatalysis properties, ion-exchange properties and charge storage capabilities.[72] There still exists a growing need for large-scale energy storage on the power grid. The power that is stored at the moment by the use of pumped hydropower and compressed air energy storage, require extremely costly investments, deliver low energy efficiency and their use is dependent on its location. It would be advantageous to produce electrochemical energy storage devices such as batteries on a grid-wide scale, due to the fact that they offer rapid response, high energy efficiency and high energy density. Existing battery technologies do not offer the long cycle life, low cost and high power needed for use on the grid. NiHCF and CuHCF offer long life cycle, high capacity retention and low hysteresis, this allows the development of devices with high energy efficiency.[59] A copper-nickel alloy hexacyanoferrate has also been shown to reversibly intercalate Na^+ and K^+ ions for over 2000 cycles with excellent retention. This alloy can be employed to tune the reaction potential and allows for the development of fuel cells which can utilize the entire stable aqueous electrochemical window.[59]

Supercapacitors have been attracting more and more attention as novel energy storage devices due to their high power densities and long cycle lives. CoHCF has exhibited large faradaic capacitance under relative high current rates. When this compound is paired with a graphene-based negative electrode in

an asymmetrical supercapacitor, it showed a high working voltage of about 2.4V and extremely high cycling stability.[74]

2.7.3.2 Biosensing

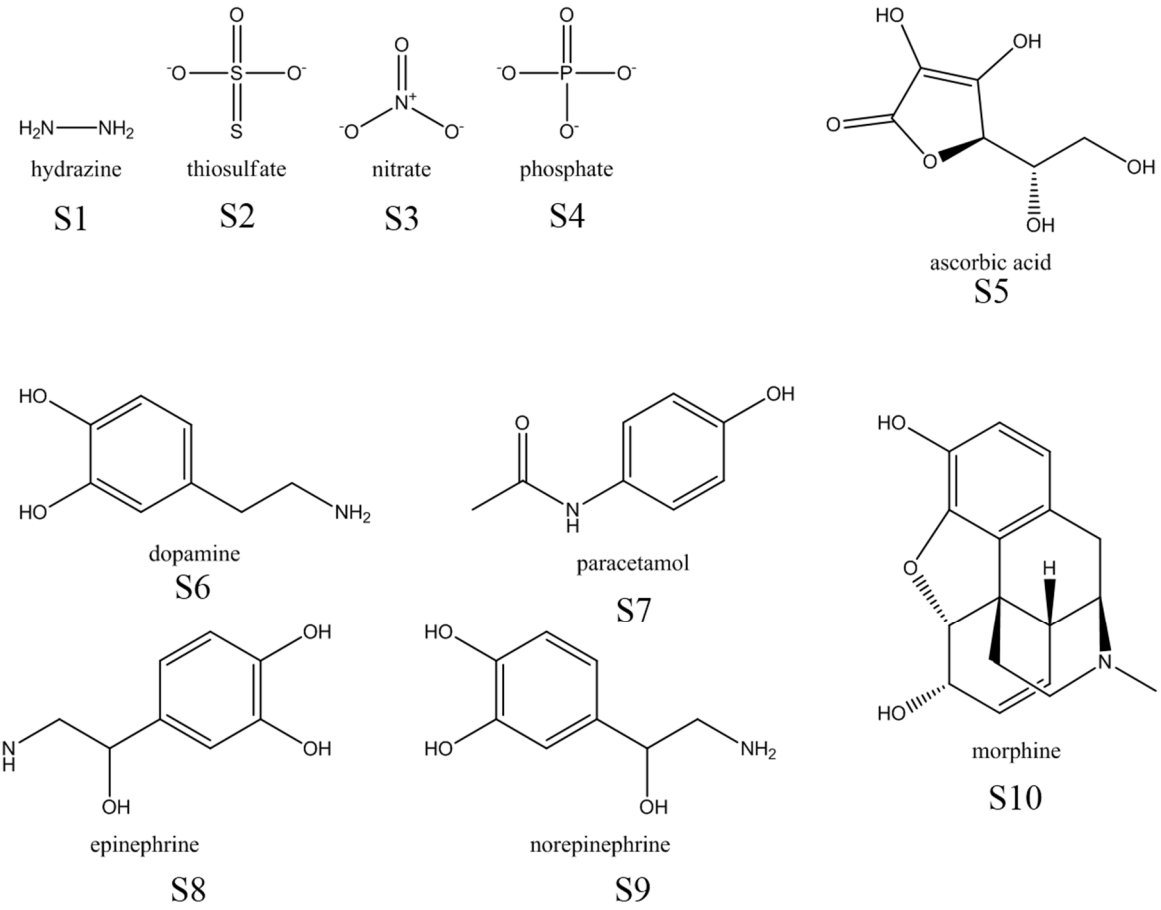

Transition metal hexacyanoferrates belong to a group of exceptional electron-transfer mediators that have attracted great attention as biosensors.[71] The high electrocatalytic activities of MHCFs have opened new possibilities in the development of electrochemical sensors for the detection of different inorganic and organic molecules.[62] Electrochemical sensors that are based on electrodes modified by MHCFs for detection of hydrazine (S1), thiosulfates (S2), nitrates (S3) and phosphates (S4) have been reported.[62, 83] Utilizing these MHCF in sensing and biosensing of molecules with environmental and biological interest, molecules such as ascorbic acid (S5), dopamine (S6), paracetamol (S7), epinephrine (S8), norepinephrine (S9) and morphine (S10) can be detected by voltammetric determination.[62, 71]

Prussian blue-based biosensors have been applied to glucose (S11) detection in whole blood samples (no dilution required). Prussian blue-based biosensors have also been used to detect cholesterol, oxalate and galactose. Prussian blue will in future be used for the assembly of oxidase-based biosensors which has a practicability in clinical, food and environmental analysis. [84]

During the redox reaction that occurs at the MHCF modified electrode, hydrogen peroxide is oxidized or reduced which can be considered as the sensor interface (see **Figure 2.14**).[84]

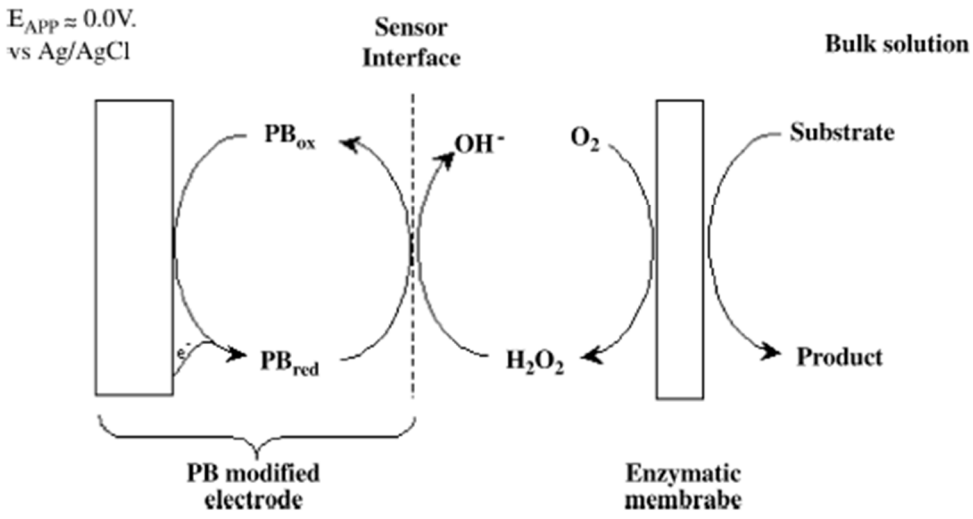

Figure 2.14: General overview for Prussian blue (PB) based biosensor with an oxidase enzyme. Reprinted (adapted) with permission from F. Ricci and G. Palleschi, *Biosensors and Bioelectronics*, 2005, **21**, 389-407. Copyright, 2005, Elsevier.

Electrodes modified with copper hexacyanoferrate demonstrated suitability for amperometric sensing of hydrogen peroxide. Glucose oxidase was immobilized on top of these copper hexacyanoferrate modified electrode to form glucose biosensors.[85]

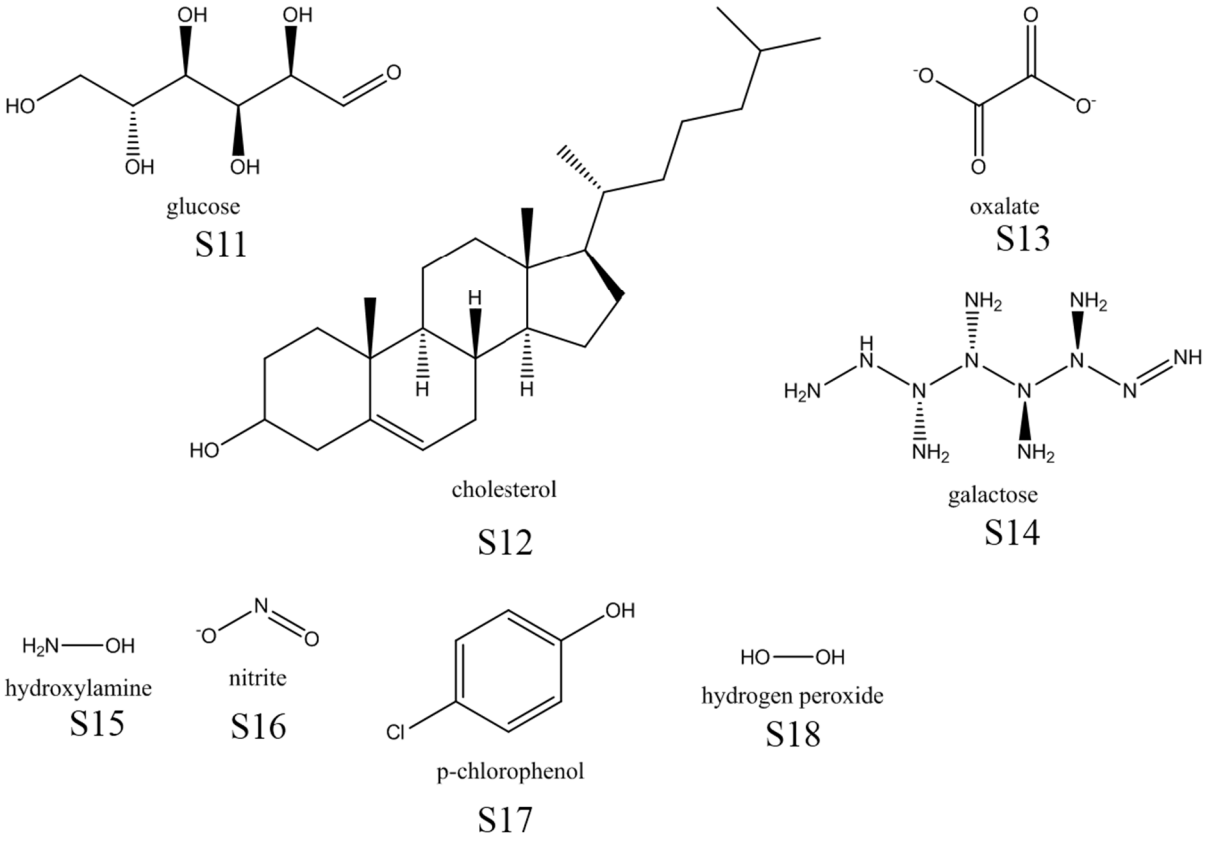

CoHCF/GC has shown high electrocatalytic activity toward the oxidation of ascorbic acid (see **Figure 2.15**). As can be seen in **Figure 2.15**, in the absence of ascorbic acid, well-defined redox peaks are observed which belongs to the CoHCF on the electrode surface. Upon the addition of 0.5 mM ascorbic acid, the anodic current increases dramatically while the cathodic current decreases significantly. It was also documented that the anodic peak potential shifts slightly in the positive direction. This shift suggests that there might exist a kinetic limitation in the reaction between ascorbic acid and CoHCF. The electrocatalytic oxidation of hydroxylamine (S15), nitrite (S16), hydrazine (S1) and *p*-chlorophenol (S17) at CoHCF modified electrodes have been reported by other authors. [86]

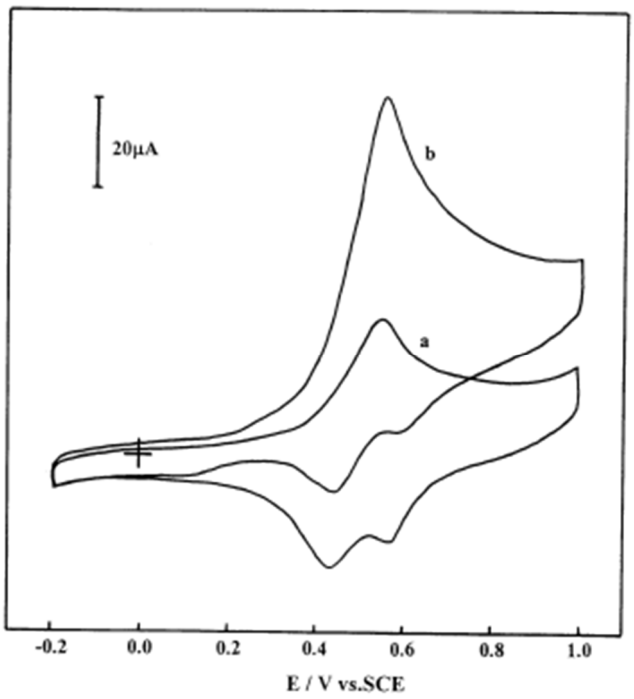

Figure 2.15: Cyclic voltammograms of a CoHCF/Glassy Carbon (GC) electrode in a phosphate buffer solution (pH 7.0) containing 0.1 M KNO_3 in the absence (a) and presence (b) of 0.5 mM ascorbic acid at scan rate of 50 mV s^{-1}. Reprinted (adapted) with permission from C. Cai, K. Xue and S. Xu, *Journal of Electroanalytical Chemistry*, 2000, **486**, 111-118. Copyright, 2000, Elsevier.

Iron hexacyanoferrate has proved to be the only hexacyanoferrate to selectively as well as sensitively detect hydrogen peroxide during the reduction of hydrogen peroxide (S18) in the presence of oxygen. The activities for copper, cobalt and nickel hexacyanoferrate in the reduction of hydrogen peroxide are far less (on average 2 orders of magnitude) than that of Prussian blue.[87]

2.7.4 Catalysis with metal hexacyanoferrates

Metal hexacyanoferrate nanoparticles have been researched for their potential in heterogeneous catalysis. Researchers have synthesized nano-sized nickel hexacyanoferrate particles and tested the material for its ability to catalyse the solvent-free oxidation of benzyl alcohol to benzaldehyde reaction. They found that nickel hexacyanoferrate nanoparticles are good heterogeneous catalysts during the solvent-free oxidation of benzyl alcohol, using hydrogen peroxide as an oxidant. It was found that the only product to form during this reaction was benzaldehyde. In general this reaction produces a mixture of benzaldehyde, benzyl benzoate and benzoic acid. They concluded that nickel hexacyanoferrate as a catalyst during the solvent-free oxidation of benzyl alcohol showed 36 % conversion with 100 % selectivity when 50 mmol benzyl alcohol was reacted with 100 mmol of H_2O_2 in the presence of 30 mg catalyst at 75 °C, over 4h.[57]

Cobalt hexacyanoferrate modified platinum, gold and glassy carbon electrodes have been applied to the oxidation of hydrazine to determine the electrocatalytic activity. It was determined that the CoHCF film that was deposited at a glassy carbon electrode indeed acts as an electrocatalyst while platinum and gold CoHCF-modified electrodes showed no significant electrocatalytic activity during the oxidation of hydrazine. This reaction was found to be pH dependent. High catalytic current was observed where the pH of the reaction ranged between 5 and 7. [83]

The oxidation and reduction of hydrogen peroxide by electrocatalysis has attracted much attention, as mentioned earlier for its sensing abilities in analytical chemistry.[87] Amongst other compounds, iron hexacyanoferrate modified electrodes showed the highest electrocatalytic activity towards the reduction of hydrogen peroxide. At one point, platinum was the most widely used material for the detection of hydrogen peroxide.[87] However, during the reduction and oxidation (in neutral media) of hydrogen peroxide, iron hexacyanoferrate has shown to be 3 orders of magnitude more active than platinum. In addition, iron hexacyanoferrate has also shown to be 3 orders of magnitude more selective than platinum during the oxidation of hydrogen peroxide in the presence of oxygen. Other Prussian blue analogues (copper-, cobalt- and nickel hexacyanoferrate) have shown good catalytic activity during the hydrogen peroxide decomposition reaction.[87]

To summarise, metal hexacyanoferrates are insoluble in water which makes heterogeneous catalysis in aqueous media eminent. Heterogeneous catalysis have practical advantages compared to homogeneous catalysis i.e. separation of the catalytic material are easier and will save time. The type of precipitation reaction that is used to prepare metal hexacyanoferrates also has its advantages i.e. it is not necessary to incorporate a support material for the catalytic material due to the fact that the metal hexacyanoferrates precipitates in a zeolite-like three dimensional crystal structure, with a cyano-bridge connecting the two different metals, creating a face-centered cubic unit cell that already has a great surface area and dispersion. Metal hexacyanoferrates can be prepared in both mono metallic and bimetallic form. However, history has taught that bimetallic catalysts have already started to replace mono metallic catalysts. The synthesis of these metal hexacyanoferrates are shown to be relatively simple. In order to prepare nano-sized particles an extra step is necessary during the preparation to stabilise the formation of the nano-sized particles. The nanomaterials of hexacyanoferrates have shown multiple enhanced properties. For example, cobalt hexacyanoferrate consists of multiple redox centers Co^{II}, Co^{III}, Fe^{II} and Fe^{III} in various stoichiometries, thus interesting electrochemical properties are expected. For practical application the electrochemistry is useful in biosensing, electrocatalysis, ion-exchange and charge storage capabilities.

References

[1] M. S. M. Laurin, PhD thesis, FU Berlin, 2005.

[2] M. E. Davis and R. J. Davis, *Fundamentals of Chemical Reaction Engineering*, Dover Publications, Inc., New York, 2012, ch. 5, p. 133.

[3] O. Deutschmann, H. Knözinger, K. Kochloefl and T. Turek, *Heterogeneous Catalysis and Solid Catalysts*, Ullmann's Encyclopedia of Industrial Chemistry, 2002, ch. 1, p. 2.

[4] R. Klaewkla, M. Arend, W. F. Hoelderich, *Mass Transfer-Advanced Aspects*, In Tech, Shanghai, 2011, ch. 29, 667-684.

[5] E. Farnetti, R. Di Monte and J. Kašper, in *Inorganic and Bio-Inorganic Chemistry*, ed. I. Bertini, EOLSS, Oxford, 2009, vol. 2, pp. 67-71.

[6] B. M. Reddy, G. M. Kumara, I. Ganesh and A. Khan, *Journal of Molecular Catalysis A: Chemical*, 2006, **247**, 81-87.

[7] J. J. Bravo-Suárez, R. V. Chaudhari and B. Subramaniam, presented in part at the ACS Symposium Series, Washington DC, June, 2013.

[8] A. Matlack, *Introduction to Green Chemistry*, 2nd Ed., CRC Press, 2010, Boca Raton, ch 5, 109-110.

[9] J. Haber, J. H. Block and B. Delmon, *Pure and Applied Chemistry,* 1995, **67**, 1260.

[10] B. Qiao, L. Liu, J. Zhang and Y. Deng. *Journal of Catalysis,* 2009, **261**, 241-244.

[11] L. De Rogatis, T. Montini, V. Gombac, M. Cargnello and P. Fornasiero, *Nanorods, Nanotubes, and Nanomaterials research Progress*, Nova Publishers, New York, 2008.

[12] D. Harvey, *Modern Analytical Chemistry,* McGraw-Hill, Boston, 2000, ISBN 0-07-237547, 238 – 239.

[13] I. M. Kolthoff, *The Journal of Physical Chemistry*, 1932, **30(3)**, 860.

[14] C. Zhu, S. Martin, R. Ford and N. Nuhfer, *Geophysical Research Abstracts,* 2003, **5**, 06552.

[15] S. D. Pradhan, S. D. Sathaye, K. R. Patil and A. Mitra, *Materials Letters,* 2001, **48,** 351.

[16] C. Bo, J. Li, Y. Han and J. Dai, *Materials Letters*, 2004, **58,** 1415.

[17] Y. Jung, W. Yoon, Y. Seo and Y. Rhee, *Catalysis Communications*, 2012, **26**, 103.

[18] W. Luhui, L. Hui, L. Yuan, C. Ying, and Y. Shuqing, *Journal of Rare Earths*, 2013, **31(10)**, 969.

[19] S. A. El-Molla, G. A. Fagal, N. A. Hassan and G. M. Mohamed. *World Applied Science Journal*, 2012, **19(9)**, 1251.

[20] G. C. Bond and D. T. Thompson, *Gold Bull.* 2006, **33**, 41.

[21] E. D. Park and J. S. Lee, *Journal of Catalysis,* 1999, **186**, 1.

[22] M. Date, Y. Ichihashi, T. Yamashita, A. Chiorino, F. Boccuzzi and M. Haruta, *Catalysis Today*, 2002, **72**, 89.

[23] F. Boccuzzi, A. Chiorino, M. Manzoli, P. Lu, T. Akita, S. Ichikawa and M. Haruta, *Journal of Catalysis,* 2001, **202**, 256.

[24] S. Minico, S. Scire, C. Crisafulli and S. Gavagno, *Applied Catalysis B*, 2001, **34**, 277.

[25] J. Lin, J. Chen, C. Hsiao, Y. Kang and B. Wan, *Applied Catalysis B*, 2002, **36**, 19.

[26] A. Wolf and F. Schuth, *Applied Catalysis A*, 2002, **226**, 1.

[27] N. A. Hodge, C. J. Kiely, R. Whyman, M. R. H. Siddiqui, G. J. Hutchings, Q. A. Pankhurst, F. E. Wagner, R. R. Rajaram and S. E. Golunski, *Catalysis Today* 2002, **72**, 133.

[28] S. J. Lee, A. Gavriilidis, Q. A. Pankhurst, A. Kyed, F. E. Wagner, P. C. L. Wong and K. L. Yeung, *Journal of Catalysis,* 2001, **200**, 298.

[29] B. Qiao and Y. Deng, *Chemical Communications*, 2003, 2192.

[30] B. Qiao and Y. Deng, *Applied Catalysis B*, 2006, **66**, 241.

[31] B. Qiao, A. Wang, X. Yang, L. F. Allard, Z. Jiang, Y. Cui, J. Liu, J. Li, T. Zhang, *Nature Chemistry,* 2011, **3**, 634.

[32] O. Sophiphun, K. Fottinger, S. Loiha, A. Neramittagapong, S. Prayoonpokarach, G. Rupprechter, J. Wittayakaun, *Reaction Kinetics, Mechanisms and Catalysis*, 2015, **116**, 549.

[33] E. Manova, T. Tsoncheva, Cl. Estournès, D. Paneva, K. Tenchev, I. Mitov and L. Petrov, *Applied Catalysis A: General*, 2006, **300**, 170 – 180.

[34] G. Li, L. Hu, and J. M. Hill, *Applied Catalysis A: General*, 2006, **301**, 16 – 24.

[35] M. Pudukudy and Z. Yaakob, *Chemical Engineering Journal*, 2015, **262**, 1009 – 1021.

[36] T. Miyake and A. Tetsuo, *Applied Catalysis A: General,* 2005, **280**, 47.

[37] M. T. Schaal, A. C. Pickerell, C. T. Williams and J. R. Monnier, *Journal of Catalysis*, 2008, **254**, 131.

[38] S. Djokic, *Modern Aspects of Electrochemistry*, 2002, **35**, 51.

[39] W. Yu, M. D. Porosoff and J. G. Chen, *Chemical Reviews*, 2012, **112**, 5780-5781.

[40] J. H. Sinfelt, *Accounts of Chemical Research*, 1977, **10(1)**, 16.

[41] J.H. Sinfelt, *Accounts of Chemical Research,* 1987, **20(4)**, 134.

[42] D. S. Shepard, T. Maschmeyer, B. F. G. Johnson, J. M. Thomas, G. Sankar, D. Ozkaya, W. Z. Zhou and R. D. Oldroyd, *Angewandte Chemie International Edition*, 1997, **36(20)**, 2242 – 2245.

[43] J. M. Thomas, B. F. G. Johnson, R. Raja, G. Sankar and P. A. Midgley, *Acc. Chem. Res.*, 2003, **36**, 20-30.

[44] E.K. Van Beuken and B.L. Feringa, *Tetrahedron*, 1998, **54**, 12985-13011.

[45] J. Conradie, T. S. Cameron, M. A. S. Aquino, G. J. Lamprecht and J. C. Swarts, *Inorganica Chimica Acta*, 2005, **358**, 2530 – 2542.

[46] J. Conradie and J. C. Swarts, *Organnometallics*, 2009, **28**, 1018 – 1026.

[47] E. Erasmus, J. W. Niemantsverdriet and J. C. Swarts, *Langmuir*, 2012, **28**, 16477.

[48] Y. Ishii, K. Miyashita, K. Kamita and M. J. Hidai. *Journal of the American Chemical Society,* 1997, **119**, 6448-6449.

[49] B. H. Lipschutz, D. M. Nihan, E. Vinogradova, B. R. Taft and Ž. V. Bošković, *Organic Letters*, 2008, **10(19)**, 4279-4280.

[50] V. Dal Santo, A. Gallo, A. Naldoni, M. Guidotti and R. Psaro, *Catalysis Today*, 2012, **197**, 190-205.

[51] G. Espinosa, G. Del Angel, J. Barbier, P. Bosch, V. Lara and D. Acosta, *Journal of Molecular Catalysis A: Chemical*, 2000, **164**, 253.

[52] S. A. Bocanegra, S. R. de Miguel, I. Borbath, J. L. Margitfalvi and O. A. Scelza, *Journal of Molecular Catalysis A: Chemical*, 2009, **301**, 52.

[53] J. H. Sinfelt, *Platinum Metals Review,* 1976, **20(4)**, 114-119.

[54] U. Prüsse and K. Vorlop, *Journal of Molecular Catalysis A: Chemical*, 2001, **173**, 313-314.

[55] J. E. Huheey, in *Inorganic Chemistry: Principles of structure and reactivity*, Harper & Row Publishers Inc., New York, 3rd edn, 1983, ch. 10, pp. 521 – 523.

[56] M. Berrettoni, M. Ciabocco, M. Fantauzzi, M. Giorgetti, A. Rossi and E. Caponetti, *Royal Society of Chemistry Advances*, 2015, **5**, 35435 -35445.

[57] S. R. Ali, P. Chandra, M. Latwal, S. K. Jain, V. K. Bansal and S. P. Singh, *Chinese Journal of Catalysis*, 2011, **32**, 1844.

[58] S.M. Golabi and F.Noor-Mohammadi, *Journal of Solid State Electrochemistry*, 1998, **2**, 30.

[59] C. D. Wessells, M. T. McDowell, S. V. Peddada, M. Pasta, R. A. Huggins and Y. Cui, *Journal of the American Chemical Society*, 2012, **2**, 1688-1689.

[60] E. Wiberg, N. Wiberg and A. F. Holleman, in *Inorganic Chemistry*, Academic Press, San Diego, 2001, p 1444.

[61] E. Dujardin and S. Mann, *Advanced Materials*, 2004, **16(13)**, 1125-1126.

[62] S. R. Ali, V. K. Bansal, A. A. Khan, S. K. Jain and M. A. Ansari, *Journal of Molecular Catalysis A: Chemical*, 2009, **303**, 60-61.

[63] J. Eastoe, G. Fragneto, B.H. Robinson, T.F. Towey, R.K. Heenan, F.J. Leng, *Journal of the Chemical Society, Faraday Transactions,* 1992, **88**, 461-471.

[64] A. Gutiérrez-Becerra, F. Martínez-Martínez, M. Bárcena-Soto, N. Casillas, I. Ceja, S. Prévost, M. Gradzielski and J. I. Escalante, *Colloids and Surfaces A: Physiochem. Eng. Aspects*, 2014, **444**, 63–68.

[65] S. Vaucher, M. Li and S. Mann, *Angewandte Chemie International Edition,* 2000, **39**, 1793.

[66] L. Shi, T. Wu, M. Wang, D. Li, Y. Zhang and J. Li, *Chinese Journal of Chemistry*, 2005, **23**, 149 – 154.

[67] D. A. Skoog, D. M. West, F. J. Holler and S. R. Crouch, *Fundamentals of Analytical Chemistry*, Brooks/Cole, 8th edition, 2004.

[68] P. T. Kissinger and W. R. Heineman, *Journal of Chemical Education,* 1983, **60**, 702 - 704.

[69] M. Govender, M. Sc. thesis, University of the Free State, 2015.

[70] E. Botha, PhD thesis, University of the Free State, 2015.

[71] M. Yang, J. Jiang, Y. Yang, X. Chen, G. Shen and R. Yu, *Biosensors and Bioelectonics* , 2006, **21**, 1791-1797.

[72] S. M. Chen, *Journal of Electroanalytical Chemistry*, 1996, **417**, 145.

[73] A. Venugopal, N. Kumar and J. Joseph, *Electrochimica Acta*, 2014, **139,** 88–95.

[74] F. Zhao, Y. Wang, X. Xu, Y. Liu, R. Song, G. Lu and Y. Li, *American Chemical Society Applied Materials & Interfaces*, 2014, **6**, 11007 – 11012.

[75] S. Liu, G. L. Pan, G. R. Li and X. P. Gao, *Journal of Materials Chemistry A*, 2015, **3**, 959.

[76] M. Berrettoni, M. Giorgetti, S. Zamponi, P. Conti, D. Ranganathan, A. Zanotto, M. L. Saladino and E. Caponetti, *The Journal of Physical Chemistry C*, 2010, **114**, 6401.

[77] A. Fitch and G. J. Edens, *Journal of Electroanalytical Chemistry,* 1989, **267**, 1–13.

[78] L. Catala, T. Gacoin, J.P. Boilot, E. Riviere, C. Paulsen, E. Lhotel, T. Mallah, *Advanced Materials,* **2003**, 15, 827.

[79] J. Moon, E. Lee and H. Kim, *Korean Journal of Chemical Engineering*, 2004, **21(5)**, 1026-1031.

[80] C. Michel, y. Barré, C. de Dieuleveult, A. Grandjean and L. De Windt, *Chemical Engineering Science*, 2015, **137**, 904-905.

[81] J. W. Niemantsverdriet, *Spectroscopy in Catalysis*, WILEY-VCH Verlag GmbH % Co. KGaA, Weinheim, 3rd edition, 2007 ch. 3, pp. 41 - 51.

[82] M. Datta and A. Datta, *Journal of Physical Chemistry*, 1990, **94**, 8203, 8207.

[83] S.M. Golabi and F. Noor-Mohammadi, *Journal of Solid State Electrochemistry*, 1998, **2**, 30 - 37.

[84] F. Ricci and G. Palleschi, *Biosensors and Bioelectronics*, 2005, **21**, 389-407.

[85] I. L. de mattos, L. Gorton, T. Laurell, A. Malinauskas and A. A. Karyakin, *Talanta*, 2000, **52**, 791-799.

[86] C. Cai, K. Xue and S. Xu, *Journal of Electroanalytical Chemistry*, 2000, **486**, 111-118.

[87] N. A. Sitnikova, M. A. Komkova, I. V. Khomyakova, E. E. Karyakina and A. A. Karyakin, *Analytical Chemistry*, 2014, **86**, 4131 – 4134.

3 Results and Discussion

3.1 Introduction

The results obtained by the author, with reference to the goals set in chapter 1, are presented in this chapter.

Four bulk- and four nano-sized metal hexacyanoferrate complexes with the general formula of $K_xM_y[Fe(CN)_6]_z \cdot qH_2O$, with M = Fe, Co, Ni and Cu, and x, y, z and q representing stoichiometric numbers, were prepared during this study. The four different metals incorporated into the metal hexacyanoferrate complexes, M = Fe, Co, Ni or Cu, were chosen to investigate the influence of changing metal (when moving to the right in the periodic table) on the physical and chemical properties of metal hexacyanoferrate complexes. A representation of the three-dimensional structure of iron hexacyanoferrate (**1**), cobalt hexacyanoferrate (**2**), nickel hexacyanoferrate (**3**) and copper hexacyanoferrate (**4**), are shown in **Figure 3.1**.

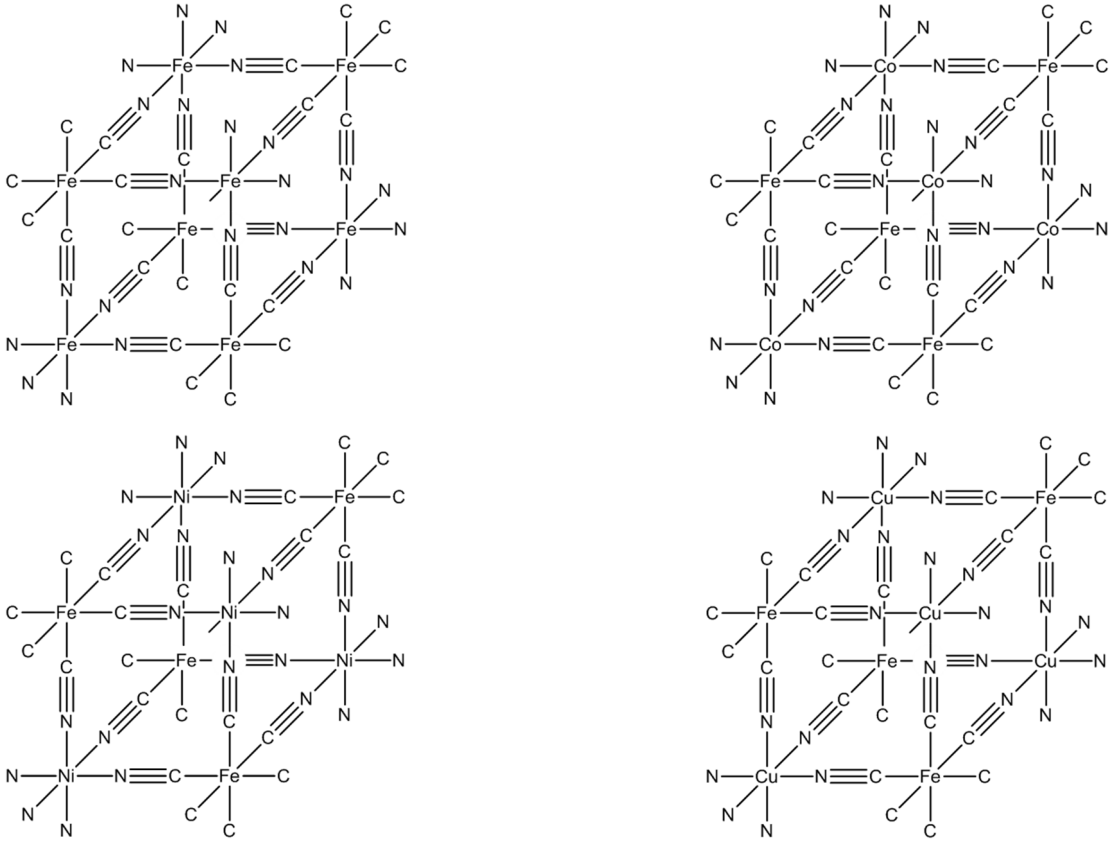

Figure 3.1: Molecular structures of the metal hexacyanoferrate complexes prepared during this study.

The complexes were characterised using multiple characterisation methods. Spectroscopic characterisation involved, attenuated total reflection Fourier transformed infrared (ATR FTIR), X-ray photoelectron spectroscopy (XPS) and transmission electron spectroscopy (TEM). Thermal analysis of the complexes was achieved by thermogravimetric analysis (TGA), and differential scanning calorimetry (DSC), electrochemical properties was investigated by using cyclic voltammetry (CV) while inductive coupled plasma optical emission spectroscopy (ICP-OES) and elemental analyses confirmed element ratios.

3.2 Synthesis

3.2.1 Preparation of bulk-sized metal hexacyanoferrates

The series of bulk-sized metal hexacyanoferrate complexes were prepared by a co-precipitation reaction according to the reaction scheme presented in **Figure 3.2**, the synthesis of **B1** (bulk-sized iron hexacyanoferrate) is shown as an example (**B1-B4** [**B2 =** bulk-sized cobalt hexacyanoferrate], [**B3 =** bulk-sized nickel hexacyanoferrate] and [**B4 =** (bulk-sized copper hexacyanoferrate] are all prepared according to the same procedure). The water soluble starting materials namely a metal halide (e.g. $FeCl_3$ for the preparation of **B1**) and the potassium hexacyanoferrate are mixed together in ambient air and at room temperature. This resulted in the formation of water soluble KCl and the water-insoluble metal hexacyanoferrate, which precipitated. The yields obtained varied significantly from 26% for **B1** to 94% for **B3** (see Experimental section, Chapter 4). The general trend appears to be that the increasing Pauling scale electronegativity, σ_M,[1] of the metal M in $K_x\underline{M}_y[Fe(CN)_6]_z{\cdot}qH_2O$, is associated with the increasing yield of the metal hexacyanoferrate that forms (see **Figure 3.3**). Thus the order of yield (from low to high) of the metal hexacyanoferrates is: **B1** (M = Fe, 26% yield, σ_M = 1.83) < **B2** (M = Co, 43% yield, σ_M = 1.88) < **B4** (M = Cu, 85% yield, σ_M = 1.90) < **B3** (M = Ni, 94% yield, σ_M = 1.91). This trend is consistent with metals that are more electron withdrawing which would be more likely to form a coordination bond with the lone pair electrons on the nitrogen atom of the cyano-group. It has previously been found that the rate of a synthetic oxidative addition reaction was a function of the electron density (electronegativity) of the metal center.[2]

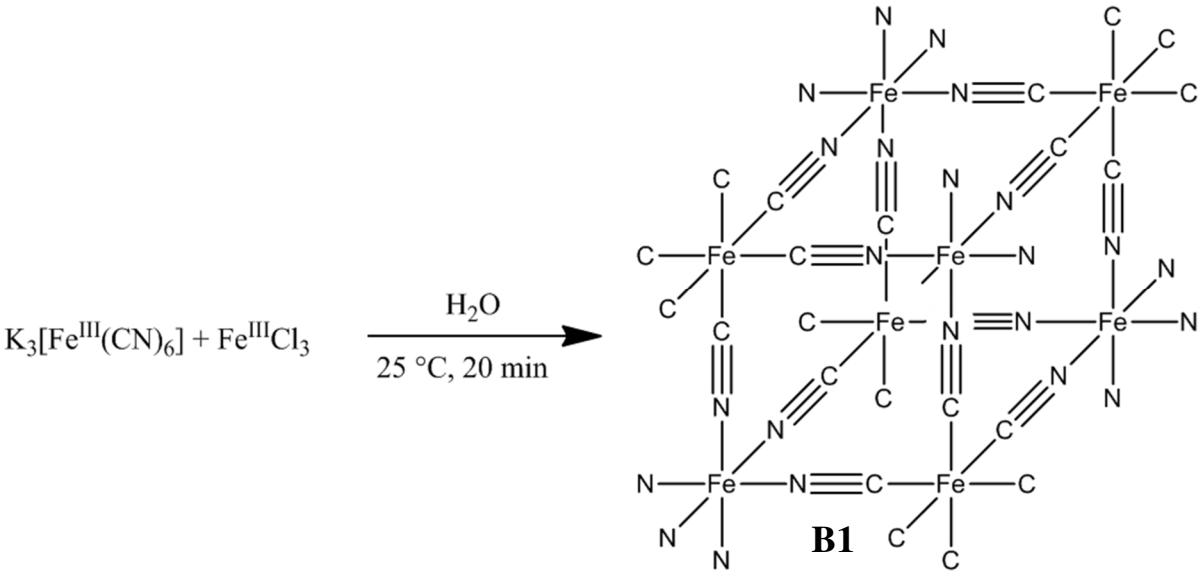

Figure 3.2: Reaction scheme for preparation of bulk sized iron hexacyanoferrate, **B1**.

3.2.2 Preparation of nano-sized metal hexacyanoferrates

Nanomaterials are of great interest due to the size effects invoked by the high surface-to-volume ratio which gives new and versatile properties to the nanomaterial as compared to the bulk-sized material. Metal hexacyanoferrates are also known as metal coordination polymers, these polymers are normally obtained in bulk form, thus special preparation methods are required to obtain nano-sized metal hexacyanoferrates.[3]

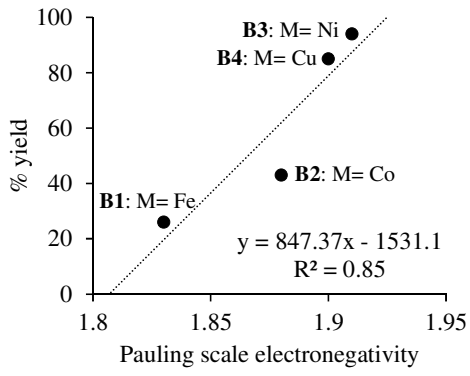

Figure 3(a)

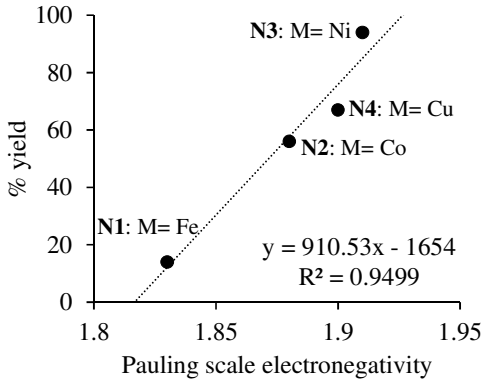

Figure 3(b)

Figure 3.3 (a) and (b): Graph showing the relationship between the yields obtained for the bulk-sized metal hexacyanoferrates, **B1-B4**, (Left) or the nano-sized metal hexacyanoferrates, **N1-N4**, (Right) and the Pauling scale electronegativity of the metal.

The nano-sized metal hexacyanoferrates, **N1-N4**, were prepared by reverse microemulsion using an anionic surfactant, sodium bis(2-ethylhexyl)sulfosuccinate (AOT). This microemulsion, confined the synthesis to occur in nanoscale droplets, which produced hydrophobic nano-sized metal hexacyanoferrates, **N1-N4**, with a uniform shape and size. The procedure involves the combination of two microemulsions, the stabilized surfactant metal, $M(AOT)_2$ where M = Fe, Co, Ni or Cu, and a potassium hexacyanoferrate-containing NaAOT microemulsion suspended in iso-octane (2,2,4-trimethylpentane). The solution immediately became intensely coloured depending on the metal in the concomitant precursor (Fe – red, Co – yellow, Ni – green and Cu – maroon), with no precipitate (bulk-sized metal hexacyanoferrates) forming. This suggests that the exchange of the reactants ($M(AOT)_2$ and $K_3Fe(CN)_6$) between different droplets (of the two different microemulsions) are sufficient to activate nucleation and growth of the surfactant stabilized nano-sized metal hexacyanoferrates, **N1-N4**.[4]

$M(AOT)_2$ (see **Figure 3.4** for the structure) is prepared by a simple cation exchange reaction between NaAOT and the desired metal halide (e.g. $Co(NO_3)_2$ to prepare $Co(AOT)_2$).

The yield for the nano-sized metal hexacyanoferrates, **N1-N4**, obtained showed the same trend as was observed for the bulk-sized metal hexacyanoferrates, **B1-B4**. The order of yield (from low to high) of the metal hexacyanoferrates is: **N1** (M = Fe, 14% yield, $\sigma_M = 1.83$) < **N2** (M = Co, 56% yield, $\sigma_M = 1.88$) < **N4** (M = Cu, 67% yield, $\sigma_M = 1.90$) < **N3** (M = Ni, 94% yield, $\sigma_M = 1.91$), see **Figure 3.3**, Right.

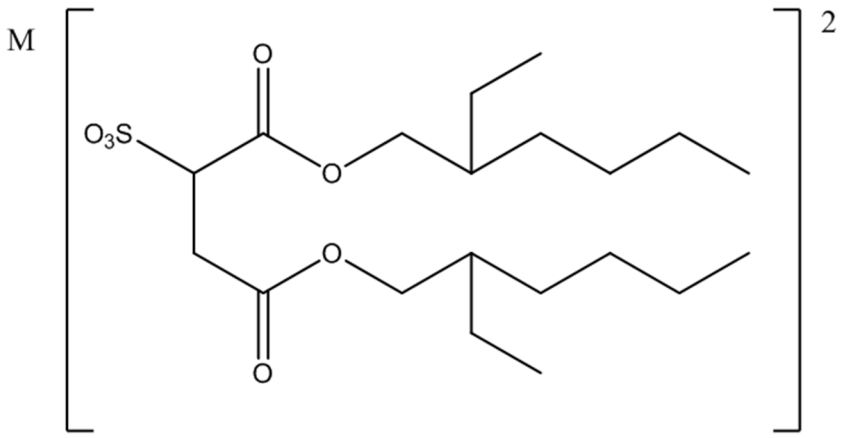

Figure 3.4: Chemical structure of stabilized surfactant material (Metal Aerosol-OT).

3.3 Characterisation

The characterisation presented and discussed in this section of the bulk- and nano-sized metal hexacyanoferrates, **B1-B4** and **N1-N4**, covers transmission electron spectroscopy (TEM), inductive coupled plasma optical emission spectroscopy (ICP-OES) attenuated total reflection Fourier transformed infrared (ATR FTIR), X-ray photoelectron spectroscopy (XPS), thermogravimetric analysis (TGA), differential scanning calorimetry (DSC) and electrochemistry *via* cyclic voltammetry (CV).

3.3.1 Transmission electron microscopy

Transmission electron microscopy was performed on all the prepared metal hexacyanoferrates, **B1-B4** and **N1-N4**, in order to determine their relative size and shape.

3.3.1.1 Transmission electron microscopy of bulk material

TEM images of the bulk-sized metal hexacyanoferrates, **B1-B4**, (see **Figure 3.5**) revealed no definite or predetermined size or shape. It is highly likely that smaller particles conglomerates to form these micro-sized particles.

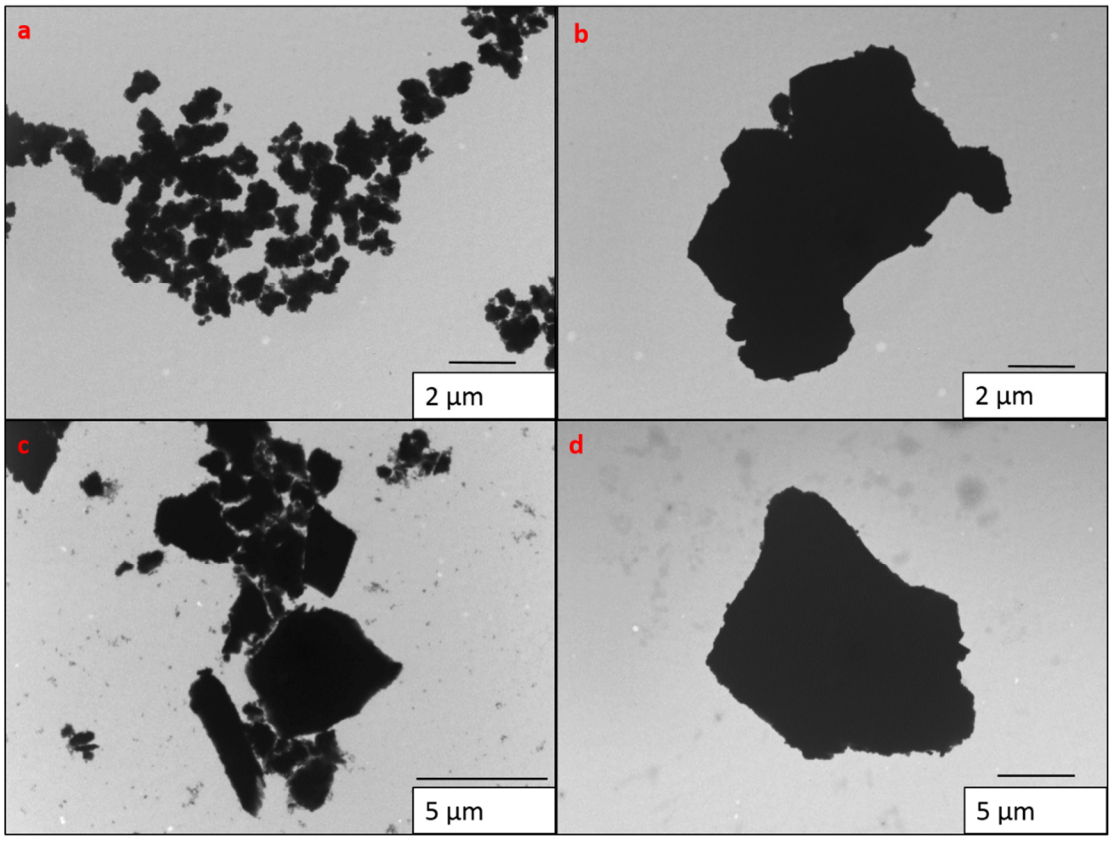

Figure 3.5: TEM images of prepared bulk sized **a**) B1, **b**) B2, **c**) B3 and **d**) B4.

3.3.1.2 Transmission electron microscopy of nano material

The different metal hexacyanoferrates, **N1-N4**, that were intentionally prepared to be nano-sized were also subjected to TEM analyses (see **Figure 3.6**). The particle size distribution curves are shown in **Figure 3.7**, while the statistical data obtained from the TEM images are given in **Table 3.1**. The TEM image of **N1**, the iron hexacyanoferrate, revealed that the particles prepared by the microemulsion reaction conditions did not afford the desired nano-particle, instead micro-sized particle formed.

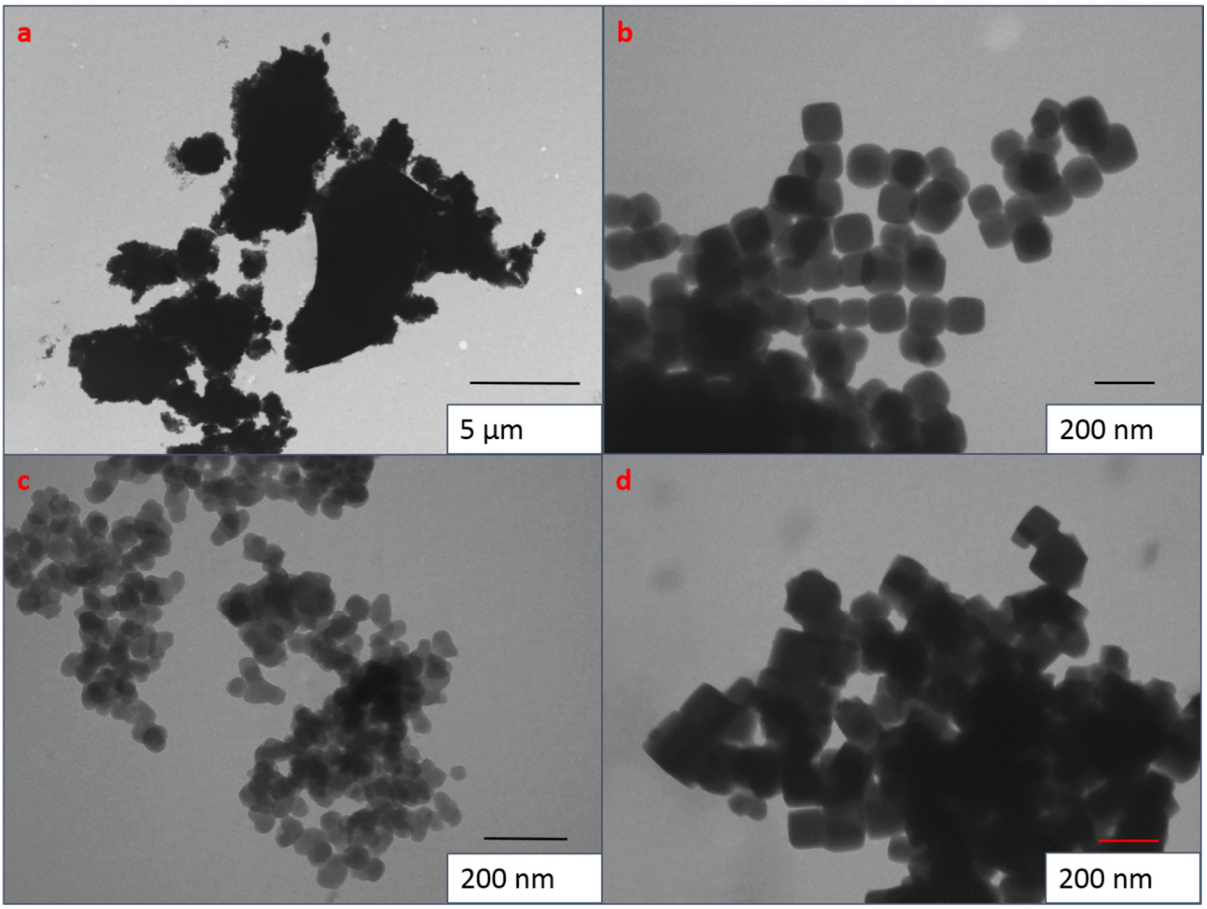

Figure 3.6: TEM images of prepared nano sized **a**) **N1**, **b**) **N2**, **c**) **N3** and **d**) **N4**.

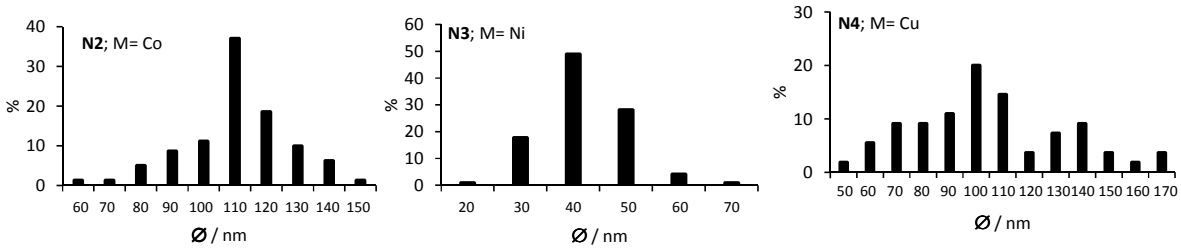

(a) **(b)** **(c)**

Figure 3.7: Particle diameter (∅) histogram of (**a**) **N2**, (**b**) **N3** and (**c**) **N4**.

Table 3.1: The mean, minimum and maximum diameter (in nm) as well as the standard deviation of the particles as measured from the TEM images.

Compound	Mean (nm)	Minimum (nm)	Maximum (nm)	Standard deviation
N2	116.18	67.63	156.31	16.35
N3	46.61	28.03	73.22	7.81
N4	124.39	70.08	179.46	29.47

The TEM image of **N2-N4**, shows that the particles have dimensions in the nanometer range (see **Figure 3.6 b-d** and **Table 3.1**). The TEM image of the cobalt hexacyanoferrate, **N2**, (see **Figure 3.6 b**) revealed that the particles are cubic in shape and the particles self-assemble into a supperlattice, where particles are stacked onto one another. This suggests that the particles are stable enough to be able to exist individually. The mean diameter of the particles of **N2** is 116.18 nm. This individuality of particles can hold great applications in heterogeneous catalysis.[5] Metal hexacyanoferrates are well known to have high surface areas with their unique microporous open channel structures, high ionic conductivities and mixed valencies. All these properties favour the heterogeneous catalytic performance of metal hexacyanoferrates. Nickel hexacyanoferrate nanoparticles have been considered to be good heterogeneous catalysts for the solvent-free oxidation of benzyl alcohol.[5]

The TEM image for the nano-sized nickel hexacyanoferrate, **N3**, (see **Figure 3.6 c**) displayed the smallest particles, with a particle mean diameter of 46.61 nm. However, the shape of the **N3** particles are not as much cubic as they are spherical, in comparison to **N2** and **N4**.

The particles of the nano-sized copper hexacyanoferrate, **N4**, (see **Figure 3.6 d**) exhibited the same characteristics with respect to size and shape as the cobalt hexacyanoferrate, **N2**, i.e. cubic particles that exhibits individuality as well as self-assembling itself into a supperlattice structure, with a mean particle diameter of 124.39 nm. No correlation could be made from the atomic or ionic radii of the metals and the diameter of the particle.

3.3.2 Inductively coupled plasma – optical emission spectroscopy

Inductively coupled plasma – optical emission spectroscopy is considered to be a reliable method to detect trace metal concentrations in sample material. It can also be used to determine the carbon and nitrogen presence in sample material in weight percentage. All the prepared samples were subjected to ICP and elemental analysis to determine the presence of certain metals (in weight percentage) as well carbon and nitrogen (in weight percentage). The results from ICP-OES and elemental analyses are summarized in the experimental section.

From the ICP experimental data, it is possible to determine the metal ratios and together with data from XPS (given in section **3.3.4**) the elemental formulas of **B1-B4** and **N1-N4**, see **Table 3.2**. The metal ratio for the bulk samples are **B2** (Fe:Co = 1:0.66), **B3** (Fe:Ni = 1:0.66) and **B4** (Fe:Cu = 1:1.29). The metal ratio for the nano samples (as determined from XPS) are **N2** (Fe:Co = 1:1.69), **N3** (Fe:Ni = 1:0.98) and **N4** (Fe:Cu = 1:1.91). From this it is clear that the metal (Co, Ni and Cu) bound to the N of the cyano-group is more abundant than the iron bound to the C of the cyano-group. Also, the N-bound metal (Co, Ni and Cu) content in the nano-sized samples are more than that of the bulk-sized sample. The stoichiometry of the prepared metal hexacyanoferrates is usually in accordance with the molar ratio of the two metal precursors. In order to maintain specific stoichiometry, a third of the ferricyanide sites are unoccupied and therefore leave vacant spaces in the crystal structure. This results in a more accessible structure. [6] This explains why the metal that is bound to the N of the cyano-group is more abundant than the iron bound to the C of the cyano group.

Table 3.2: Stoichiometric quantified formulae for all prepared complexes.

Complex	Size	No	Quantified Formulae
Fe-C≡N-Fe	Bulk	**B1**	$K_1Fe_{1.8}Fe(CN)_6$
	Nano	**N1**	$K_{0.00}Fe_1Fe(CN)_6$
Fe-C≡N-Co	Bulk	**B2**	$K_{0.24}Co_{0.66}Fe(CN)_6$
	Nano	**N2**	$K_{0.97}Co_{1.69}Fe(CN)_6$
Fe-C≡N-Ni	Bulk	**B3**	$K_{0.43}Ni_{0.66}Fe(CN)_6$
	Nano	**N3**	$K_{0.00}Ni_{0.98}Fe(CN)_6$
Fe-C≡N-Cu	Bulk	**B4**	$K_{0.10}Cu_{1.29}Fe(CN)_6$
	Nano	**N4**	$K_{0.06}Cu_{1.91}Fe(CN)_6$

3.3.3 Attenuated Total Reflection Fourier Transformed Infrared

ATR FTIR can be used to determine the presence of certain functional groups (like carbonyls or cyano-groups) and the wavenumber is also an indication of the chemical environment surrounding these functional groups. In this study ATR FTIR was used to determine the wavenumber of C≡N bonds in the different hexacyanoferrate complexes, **B1-B4** and **N1-N4**.

According to Berrettoni *et al.*, the C≡N stretching frequencies for metal hexacyanoferrates are located between 2000 cm^{-1} and 2300 cm^{-1}.[7] While according to Sheha, the OH stretching frequencies of the water molecules (adsorbed on the outside) are located at 3100 - 3600 cm^{-1} and the δ(HOH) bending vibration of coordinated water molecules that are trapped within the crystal structure can be detected at ca. 1600 cm^{-1}.[8] The wavenumbers of the strongest ATR FTIR C≡N, OH stretching and HOH bending frequencies are tabulated in **Table 3.3**. The cyanide group binds to the metal through a σ-bond by donating electrons from its weakly antibonding 5σ orbital to the metal and in a π-bond by accepting electrons from the metal in a back-donation to its antibonding π-orbital. The σ-donation has a tendency to increase the ν(CN) value, while the back bonding tends to decrease the ν(CN) value. The ν(CN) value of cyano complexes are governed by the electronegativity, the oxidation state and the coordination number of the metal bonded directly to the cyanide bond. [9, 10]

Table 3.3: Table documenting the strongest C≡N, OH stretching frequencies as well as δ(HOH) bending vibration obtained during ATR FTIR analyses of all prepared metal hexacyanoferrates.

Sample Complex	***ν*** **C≡N (cm^{-1})**	***ν*** **OH (cm^{-1})**	δ(HOH) **(cm^{-1})**
B1: bulk-FeHCF	2060	3267	1603
B2: bulk-CoHCF	2107	3382	1606
B3: bulk-NiHCF	2162, 2097	3347	1606
B4: bulk-CuHCF	2100	3374	1599
N1: nano-FeHCF	2077	3183	1621
N2: nano- CoHCF	2162, 2100	3389	1607
N3: nano-NiHCF	2165	3381	1609
N4: nano-CuHCF	2153, 2077	3389	1603

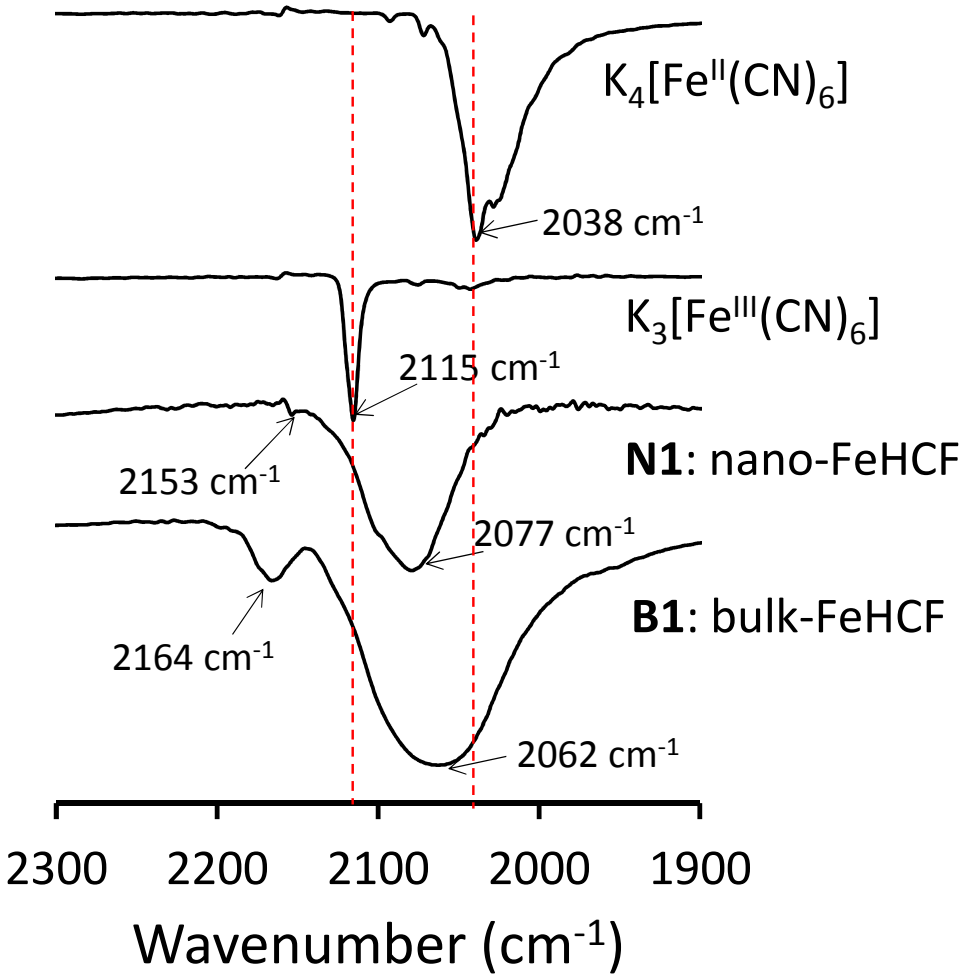

Figure 3.8: ATR FTIR spectra of bulk-FeHCF, **B1**, and nano-FeHCF, **N1**, as well as $K_4[Fe^{II}(CN)_6]$ and $K_2[Fe^{III}(CN)_6]$ in the region of CN stretching frequencies.

Figure 3.8 shows the comparative ATR FTIR C≡N stretching frequency region (1900-2300 cm^{-1}) of the bulk- and nano-sized iron hexacyanoferrates, **B1** and **N1**, as well as the infrared frequencies of Fe^{II}-C≡N (as measured from $K_4[Fe^{II}(CN)_6]$) and Fe^{III}-CN (as measured from $K_3[Fe^{III}(CN)_6]$). The Fe bound to the carbon of the C≡N group in **B1** and **N1** is not clear cut Fe^{II} or Fe^{III} (as depicted by the red dotted lines), but a combination. [11, 12] **N1** curve displays that Prussian Blue (2077 and 2153 cm^{-1}) and Berlin Green (2095 and 2152 cm^{-1}) might have overlapped or may be too weak to identify. It can thus be assumed that the Fe bound to the nitrogen of the C≡N group is also a combination of Fe^{II} or Fe^{III}. There are thus four different possible combinations of mixed valent species that are present in both **B1** and **N1**, namely Fe^{II}-C≡N-Fe^{II}, Fe^{III}-C≡N-Fe^{II}, Fe^{III}-C≡N-Fe^{III} and Fe^{II}-C≡N-Fe^{III}, each with its own chemical and electronic environment.

From literature it is known that Berlin green (Fe^{III}-C≡N-Fe^{III}) displays C≡N stretching frequencies at 2089 cm^{-1} (strong) and 2152 (weak) cm^{-1}, while Prussian blue (Fe^{II}-C≡N-Fe^{II}) displays C≡N stretching frequencies at 2078 (strong) and 2159 (weak) cm^{-1}.[13] Upon comparison of the results obtained and from that of literature, it is evident that **N1** display C≡N stretching frequencies that correlates good with Prussian blue, while **B1**'s C≡N stretching frequencies correlates more with that displayed by Berlin green. It is thus possible to conclude that the nano-sized iron hexacyanoferrate, **N1**, thus exists more in Fe^{III}-C≡N-Fe^{III} form and the bulk-sized iron hexacyanoferrate, **B1**, exists more in Fe^{II}-C≡N-Fe^{II} form, but mixed with the other possible species as well.

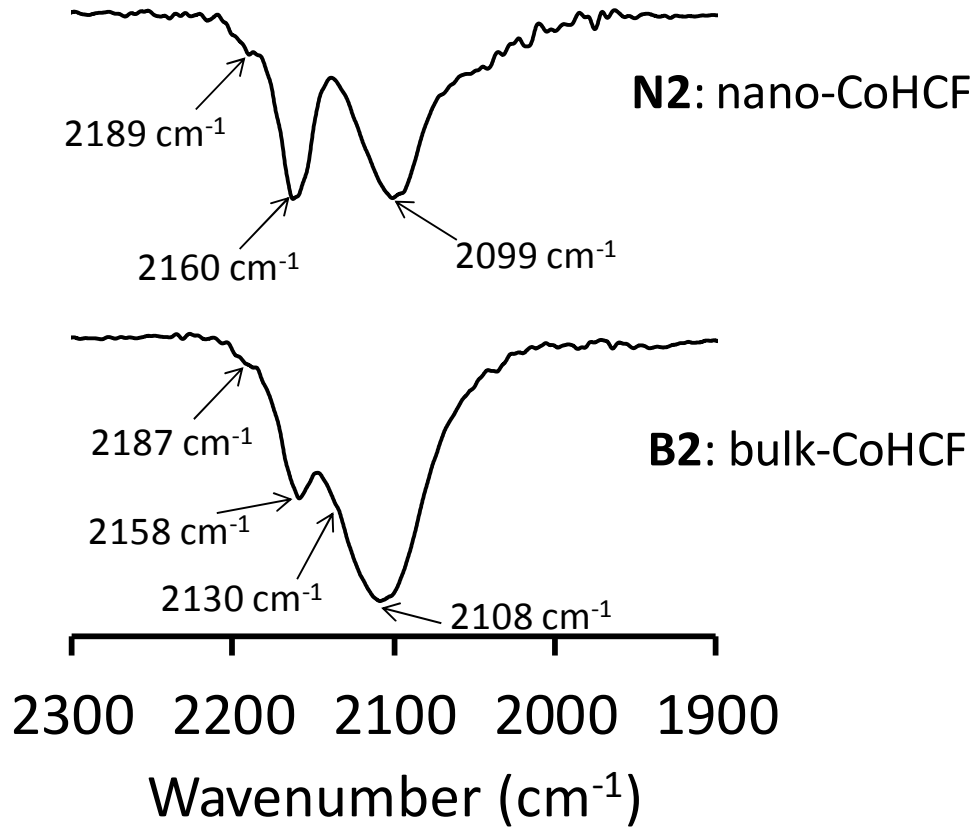

Figure 3.9: ATR FTIR of bulk-CoHCF, **B2**, and nano-CoHCF, **N2**, in the region of CN stretching frequencies.

The characteristic C≡N stretching frequencies of the bulk- and nano-sized cobalt hexacyanoferrates, **B2** and **N2**, (see **Figure 3.9**) were assigned based on reported literature.[7, 14, 15] The peak found at 2099 (for **N2**) and 2108 (for **B2**) cm^{-1} (see **Figure 3.9**) is attributed to the C≡N stretching frequency of the Fe^{II}-C≡N-Co^{II} species. While the peak found at ±2159 cm^{-1} (see **Figure 3.9**) can be assigned to Fe^{III}-C≡N-Co^{II}. The C≡N stretching frequency for Fe^{II}-

$C\equiv N\text{-}Co^{III}$ is normally located at ca. 2125 cm^{-1}, however for **B2** and **N2** the stretching frequency of the $Fe^{II}\text{-}C\equiv N\text{-}Co^{II}$ species is so strong, that the C≡N stretching frequency for $Fe^{II}\text{-}C\equiv N\text{-}Co^{III}$ is hidden underneath the peak for the $Fe^{II}\text{-}C\equiv N\text{-}Co^{II}$. The other possible species that could exist namely $Fe^{III}\text{-}C\equiv N\text{-}Co^{III}$, which according to literature is found at 2190 - 2200 cm^{-1},[14] could only be detected in very small amounts at 2187 and 2189 cm^{-1} for **B2** and **N2**, respectively.

The C≡N stretching frequency of the $Fe^{II}\text{-}C\equiv N\text{-}Co^{II}$ species was found be more intense in the bulk-size cobalt hexacyanoferrate than in the nano-sized counterpart. From ATR FTIR it is not possible to detect the amount of each species present in the sample, this might be quantified by XPS (see section **3.3.4**).

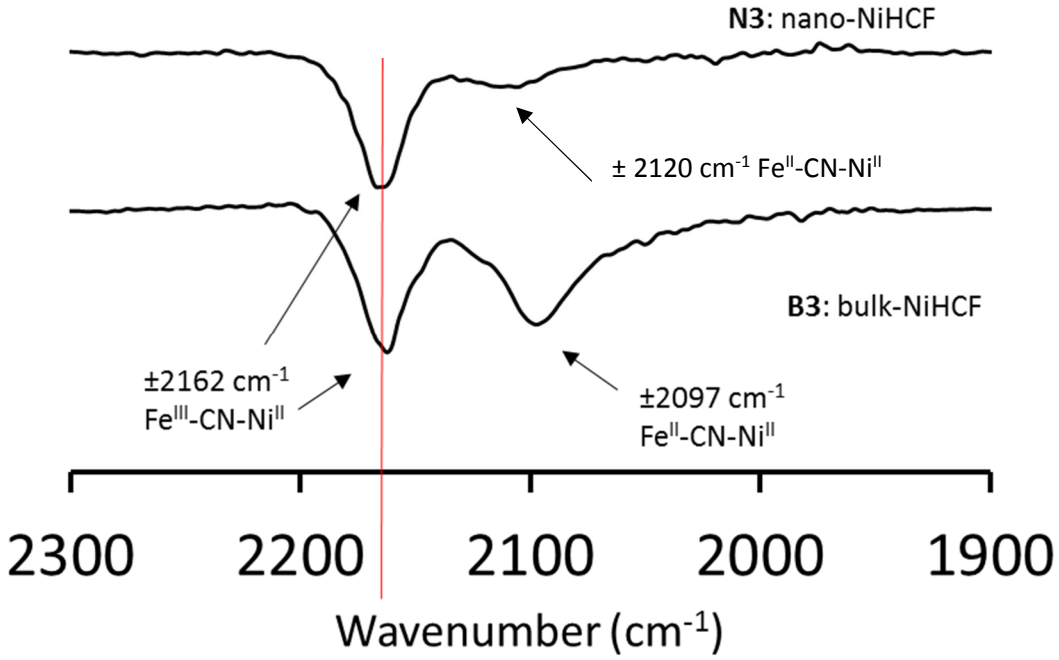

Figure 3.10: ATR FTIR of bulk-NiHCF, **B3**, and nano-NiHCF, **N3**, in the region of CN stretching frequencies.

The ATR FTIR spectra of the bulk- and nano-NiHCFs (**B3** and **N3**), see **Figure 3.10**, are very similar with the exception of the strong peak at 2097 cm^{-1} only present in **B3**. Both spectra display two peaks, a strong C≡N stretching frequencies at 2162 cm^{-1} and a weak C≡N stretching frequencies at ca. 2120 cm^{-1}. The characteristic C≡N stretching frequencies of the bulk- and nano-sized nickel hexacyanoferrates, **B3** and **N3**, (see **Figure 3.10**) were assigned based on reported literature.[5, 12] In accordance with the peak assignments made for **B2** and **N2**, the peak found at 2164 (for **N3**) and 2161 (for **B3**) cm^{-1} (see **Figure 3.10**) is attributed to the C≡N stretching frequency of the $Fe^{III}\text{-}C\equiv N\text{-}Ni^{II}$ species, while the peak with the weak intensity at ca. 2120 cm^{-1} is assigned to $Fe^{II}\text{-}C\equiv N\text{-}Ni^{III}$ species. The peak found 2097 cm^{-1} (for only **B3** see **Figure 3.10**) is attributed to the C≡N stretching frequency of the $Fe^{II}\text{-}C\equiv N\text{-}Ni^{II}$ species.

XPS analyses provided more insightful data into the prepared products (see section **3.3.4**). XPS proved that **B3** and **N3** both exhibited Fe^{II} and Fe^{III} oxidation states while simultaneously exhibiting both Ni^{II} and Ni^{III} oxidation states.

The ν(CN) value assigned to the Fe^{III}-CN-Ni^{II} (2162 cm^{-1}) moiety is red-shifted by 65 cm^{-1} more than Fe^{II}-CN-Ni^{II} (2097 cm^{-1}). It has been reported previously that this shift in frequency can be due to the change in the electronic state of the N-coordinated cations from high-spin (Co^{II}) to low-spin (Co^{III}).[11] It was suggested that the decrease in e_g electrons with antibonding character leaded to the increase in back-bonding accompanied by a partial depopulation of the π(N-C) orbital in order to compensate for the charge deficit at the central ion caused by the back bonding. The decrease of electrons in the antibonding π(N-C) results in the shift of ν(CN) toward higher frequency. [11]

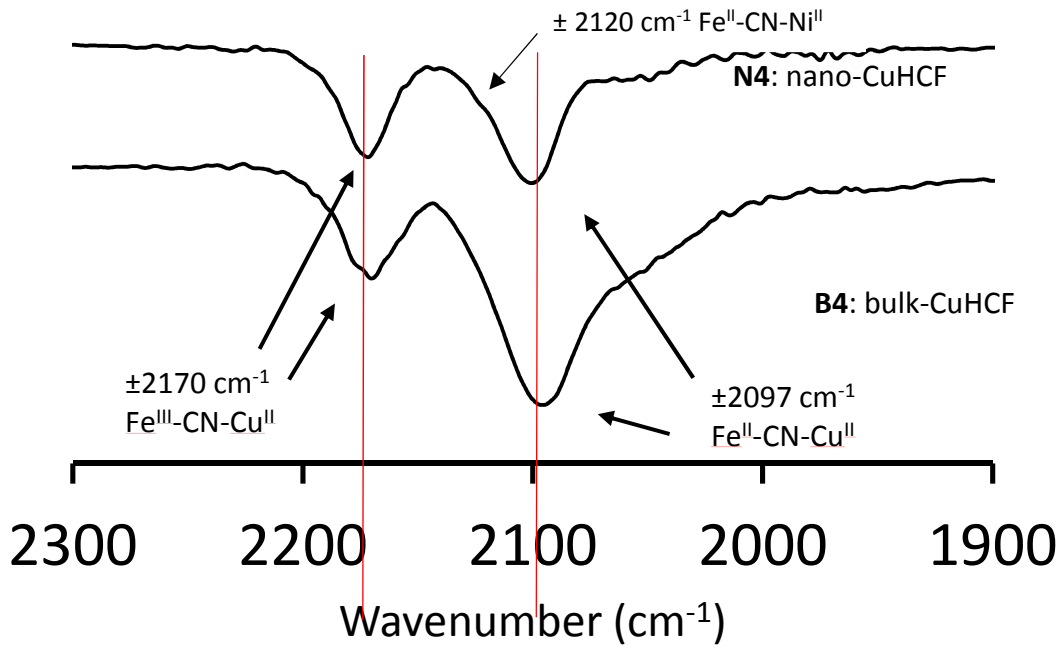

Figure 3.11: FT-IR of CuHCF-bulk and CuHCF-nano in the region of CN stretching frequencies.

The characteristic C≡N stretching frequencies of the bulk- and nano-sized copper hexacyanoferrates, **B4** and **N4**, (see **Figure 3.11**) were assigned based on reported literature.[9, 10] There seems to be an overlap of peaks at 2169 and 2172 cm^{-1} (for **B4**) which could be attributed to the C≡N stretching frequency of the Fe-C≡N-Cu species where a combination of iron and/or copper oxidation states exists simultaneously. The peak found at 2171 (for **N4**) and 2169 (for **B4**) cm^{-1} (see **Figure 3.11**) is attributed to the C≡N stretching frequency of the Fe^{III}-

$C\equiv N\text{-}Cu^{II}$ species. The peak found at 2099 (for **N4**) and 2095 (for **B4**) cm^{-1} can be attributed to the C≡N stretching frequency of either the $Fe^{II}\text{-}C\equiv N\text{-}Cu^{II}$, while the shoulder at ca. 2120 cm^{-1} of the strong peak could be assigned to the $Fe^{II}\text{-}C\equiv N\text{-}Cu^{III}$ species. The presence of Fe^{II} and Fe^{III} as well as Cu^{II} and Cu^{III} is confirmed by the XPS analyses (see section **3.3.4**) for both bulk and nano-sized copper hexacyanoferrate (**B4** and **N4**).

3.3.4 X-ray photoelectron spectroscopy

X-ray photoelectron spectroscopy (XPS) is a valuable characterisation technique used to determine the composition of a sample as well as the oxidation state of metals within the sample. It is also useful to give insight into the chemical and electronic environment of the element under investigation. Additionally, the binding energy position as well as the substructure of the photoelectron lines of the elements under investigation are affected by final-state effects, such as shake-up -, shake-down peaks and multiplet splitting. The source of these final state effects are crystal field splitting and charge transfer from an electron rich fragment of the molecule to an electron poor fragment of the molecule.[16, 17]

XPS has been performed on all prepared complexes, **B1-B4** and **N1-N4**, to determine the oxidation states and the ratios of the oxidation states of the metals in the metal complexes. The substructures of the main metal photoelectron lines will be used to explain charge transfer from the ligand to the metal as well as inner-sphere reorganisation, which occurs according to the Franck-Condon principle.

XPS data of the metal hexacyanoferrates, **B1-B4** and **N1-N4**, with respect to Fe 2p, M 2p and N 1s photoelectron lines are presented in **Tables 3.4** and **3.5**, while the comparative graphs of the different compounds are depicted in **Figures 3.12** and **3.15**.

The iron, Fe 2p photoelectron lines of all the metal hexacyanoferrates, **B1-B4** and **N1-N4**, will be discussed first. Normally the binding energy reported in literature for the Fe $2p_{3/2}$ photoelectron line of Fe^{III} in $K_3[Fe^{III}(CN)_6]$ is located at 709.60 eV,[18] and for Fe^{II} in $K_4[Fe^{II}(CN)_6]$ at 708.50 eV.[19]

The peaks of the Fe $2p_{3/2}$ and Fe $2p_{1/2}$ photoelectron lines showed splitting of the main photoelectron lines (both Fe $2p_{3/2}$ and Fe $2p_{1/2}$) into three distinct substructures. The maximum binding energy of the Fe $2p_{3/2}$ and Fe $2p_{1/2}$ photoelectron lines are located between 708.18 - 710.48 eV and 721.14 – 723.36 eV respectively, charge corrected against C 1s at 284.8 eV (the lowest binding energy of the fitted adventitious C 1s peak).[20] The three distinct substructures are assigned to the presence of Fe^{II} at ca. 708.4 eV and Fe^{III} at ca. 710.1 eV, in accordance with

the reported literature values.[19, 21] The third peak located at ca. 712.3 eV is attributed to the charge transfer from the C≡N-group ("ligand") to the Fe^{II}.

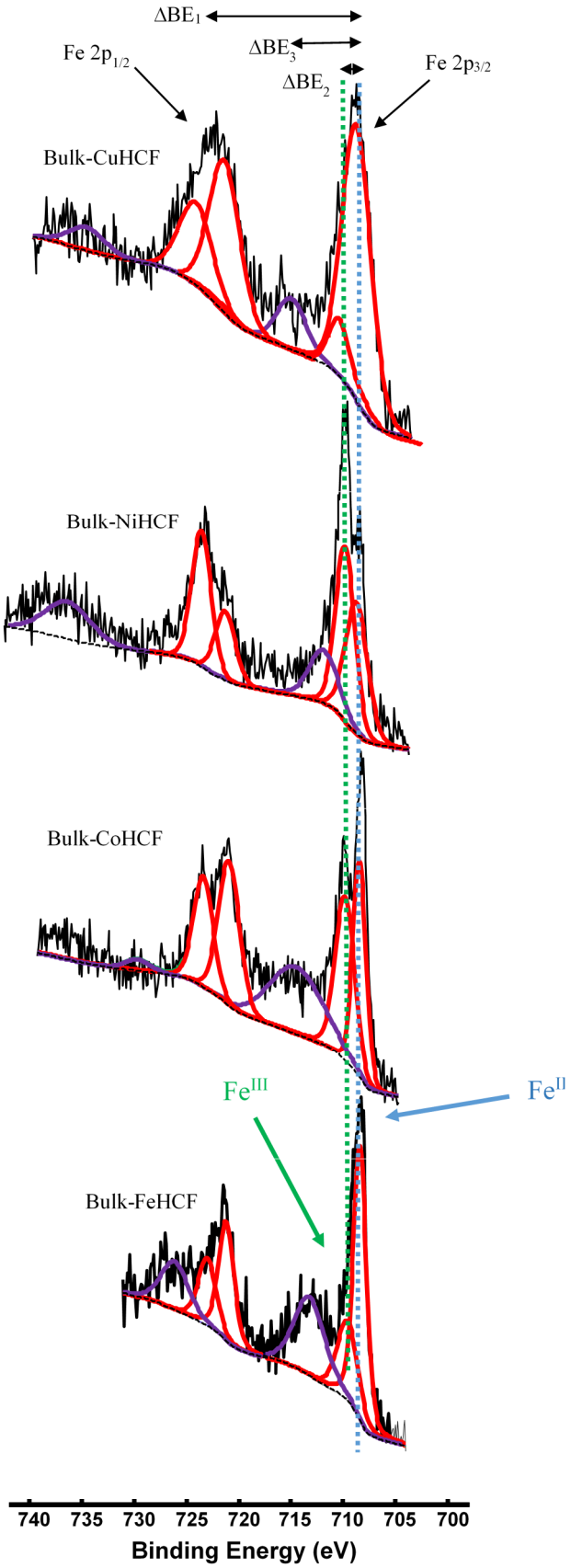

Figure 3.12: Comparative XPS spectra showing the main Fe 2p (red) as well as the satellite peaks (purple) of the bulk-sized hexacyanoferrates.

In an attempt to find a link between the binding energy of the Fe $2p_{3/2}$ photoelectron line of **B1-B4** and different metals in the metal hexacyanoferrates, a correlation graph was constructed between the binding energy of the Fe^{II} $2p_{3/2}$ and Fe^{III} $2p_{3/2}$ photoelectron lines and the Pauling electronegativity of the metal, σ_M, see **Figure 3.13** (a) and (b) respectively. It is evident that as the Pauling electronegativity of the metal increases, the binding energy of the Fe^{II} $2p_{3/2}$ and Fe^{III} $2p_{3/2}$ photoelectron lines also increases (according to: $BE_{FeII2p3/2} = 1.921\ \sigma_M + 704.92$; $R^2 = 0.982$ and $BE_{FeIII2p3/2} = 9.816\ \sigma_M + 691.5$; $R^2 = 0.974$). The higher the σ_M, the more electron density is pulled away from the iron metal, causing the iron to bind tighter to its own electrons, which triggers the higher binding energy observed for the Fe^{II} $2p_{3/2}$ and Fe^{III} $2p_{3/2}$ photoelectron lines.

A difference between the Fe^{II} $2p_{3/2}$ and Fe^{II} $2p_{1/2}$ photoelectron lines (ΔBE_1 or also known as the spin orbit splitting) of ca. 13.2 eV was obtained, the exact value is determined by the Pauling electronegativity of the metal, σ_M, see **Figure 3.13** (c). Similar to the binding energies, the spin orbit splitting also increases as the σ_M increases (according to: $\Delta BE_1 = 5.237\ \sigma_M + 3.34$; $R^2 = 0.886$). This correlation shows how the degree of delocalization of the spin density of the valence orbital rely on the electron density of the iron (indicated by the σ_M). The more electron density on the iron (lower σ_M) indicates a higher degree of delocalization of the spin density of the valence orbital (as indicated by the higher ΔBE_1).

The difference in binding energy measured for the Fe^{II} $2p_{3/2}$ and Fe^{III} $2p_{3/2}$ photoelectron lines (ΔBE_2) was again found to be controlled by the Pauling electronegativity of the metal, σ_M, see **Figure 3.13** (d), according to: $\Delta BE_2 = 5.0\ \sigma_M - 7.935$; $R^2 = 0.949$. This directly proportional correlation indicated that an increase in σ_M is accompanied by an increase in ΔBE_2. Thus as more electron density is pulled away from the iron by the other metal (Fe in **B1**, Co in **B2**, Ni in **B3** and Cu in **B4**) the difference in electronic environment between the Fe^{II} and Fe^{III} becomes larger. The electronic environment (binding energy of the Fe^{III} $2p_{3/2}$ photoelectron line) of the Fe^{III} is thus more affected by electron density (induced by σ_M) than the Fe^{II}. This tuning effect of the electronic environments of the Fe^{II} and Fe^{III} in **B1-B4**, could potentially be very useful in catalysis. By changing the M in $K_xM_y[Fe(CN)_6]_z \cdot qH_2O$, **B1-B4** could be adapted for different reactions or altering the activity and selectivity of a specific reaction.

The ratio of the amount of Fe^{II} and Fe^{III} present in **B1-B4**, varies depending on the σ_M of the other metal present in the metal hexacyanoferrate. As the electron density on the iron decreases (higher σ_M), the less Fe^{II} and the more Fe^{III} is present in the metal hexacyanoferrate according to: $I_{ratio} = -13.89\ \sigma_M - 27.26$; $R^2 = 0.835$, see **Figure 3.13** (e).

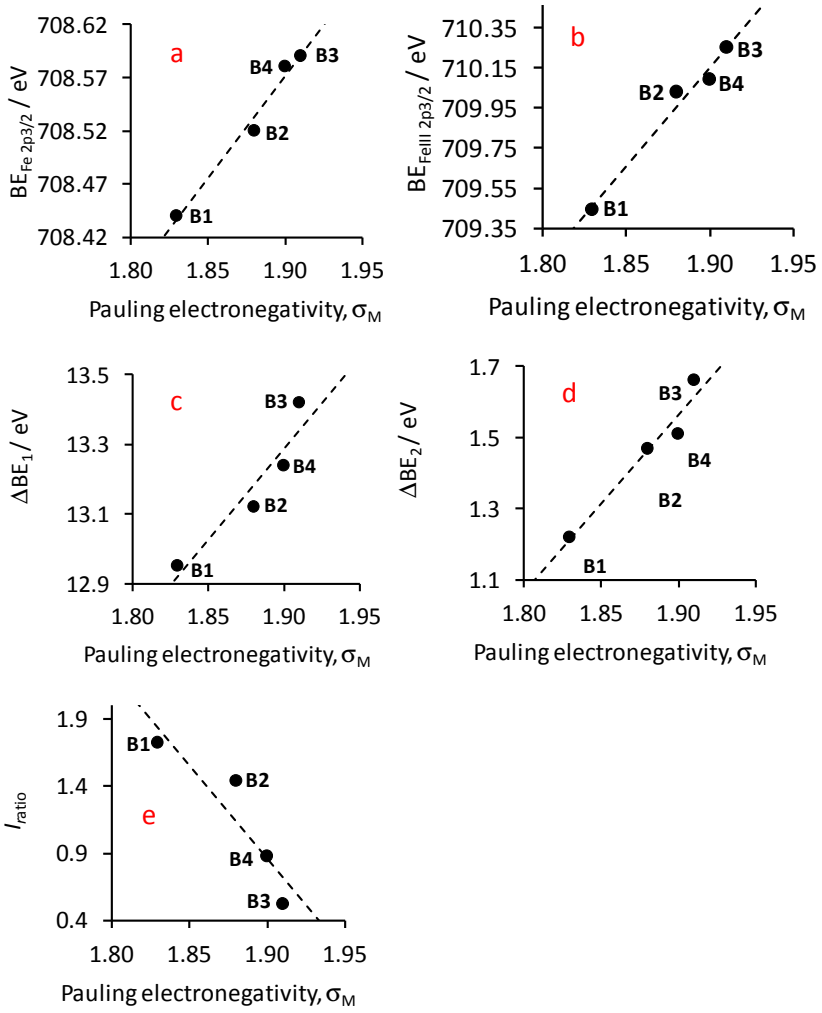

Figure 3.13: The relationships of **B1-B4** between the Pauling electronegativity of the metal, σ_M, and (a) the binding energy of the Fe^{II} Fe $2p_{3/2}$ photoelectron line, (b) the binding energy of the Fe^{III} Fe $2p_{3/2}$ photoelectron line, (c) the spin orbit splitting of the Fe $2p_{3/2}$ and Fe $2p_{3/1}$ photoelectron lines (ΔBE_1 = $BE_{Fe2p1/2} - BE_{Fe2p3/2}$ (d) the difference in binding energy of the Fe^{II} $2p_{3/2}$ and Fe^{III} $2p_{3/}$photoelectron lines ($\Delta BE_2 = BE_{FeIII\ 2p3/2\ main} - BE_{FeII\ 2p3/2\ main}$) (e) I_{ratio} = ratio between the intensities of the Fe^{II} and Fe^{III} Fe $2p_{3/2}$ photoelectron lines ($I_{ratio} = (I_{FeII\ 2p3/2\ main})/(I_{FeIII\ 2p3/2\ main})$).

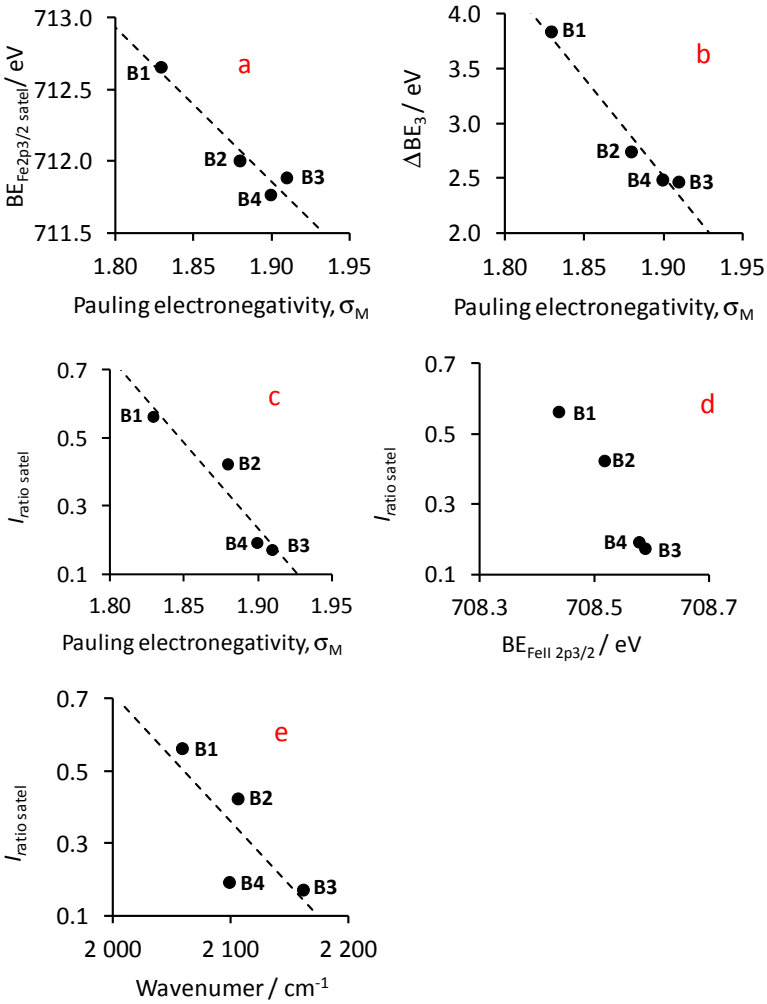

Figure 3.14: The relationships of **B1-B4** between the Pauling electronegativity of the metal, σ_M, and (a) the maximum binding energy of the satellite Fe $2p_{3/2}$ ($BE_{Fe\ 2p3/2\ satel}$) photoelectron line, (b) $\Delta BE_3 = BE_{Fe2p3/2satel} - BE_{Fe2p3/2main}$, (c) the difference in binding energy of the Fe $2p_{3/2main}$ and Fe $2p_{3/2\ satel}$ photoelectron lines. The relationships of **B1-B4** between $I_{ratio\ satel}$ = ratio between the intensities of the satellite and main Fe $2p_{3/2}$ photoelectron lines ($I_{ratio} = (I_{Fe2p3/2satel})/(I_{Fe2p3/2main})$) and the maximum binding energy of the satellite Fe $2p_{3/2}$ ($BE_{Fe\ 2p3/2\ satel}$) photoelectron line (d) and the wavenumber of the carbonyl stretching frequency (e).

The satellite peak, Fe $2p_{3/2satel}$, located at ca. 2.9 eV higher than the maximum of the main Fe $2p_{3/2}$ envelope (the combined Fe^{II} $2p_{3/2}$ and Fe^{III} $2p_{3/2}$ photoelectron lines), see **Figure 3.12**, has been reported as the result of charge transfer from the ligand to the metal in octahedral first row transition metal complexes.[22] An inversely proportional relationship has been established between the maximum binding energy of the Fe $2p_{3/2}$ satellite peak and σ_M, according to: $BE_{Fe\ 2p3/2satel} = -10.76 + 732.31$, $R^2 = 0.93$ (see **Figure 3.14** (a)).

When the orbital of a metal (in this case the Fe) and ligand (in this case the C≡N-group, in particular the carbon's orbitals) overlaps, it forms a bonding molecular orbital and an antibonding molecular orbital (the orbitals of the nitrogen in the C≡N-group overlaps with the orbital of either Fe, Co, Ni or Cu for **B1-B4**, but his will not be discussed in detail). The amount

of overlap between these orbitals determines the energy of the molecular orbitals that form. A larger overlap induces a lower energy for the bonding molecular orbital (which usually located over the metal center) and a higher energy for the antibonding molecular orbital (normally located over the ligand). The difference between the maximum binding energy of the main Fe $2p_{3/2}$ photoelectron line (which is an indication of the bonding molecular orbital) and the satellite Fe $2p_{3/2}$ photoelectron line (which is an indication of the antibonding molecular orbital), $\Delta BE_3 = BE_{Fe2p3/2satel} - BE_{Fe2p3/2main}$, can be used as a measure of the degree of covalence of the ligand-metal bond. From **Figure 3.14** (b), as σ_M increases the degree of covalency (indicated by ΔBE_3) decreases. Thus, the Fe-C≡N bond in **B3** has a lower degree of covalency than the Fe-C≡N bond in **B1**.

The $I_{ratio\ satel}$ ($I_{ratio} = (I_{Fe2p3/2satel})/(I_{Fe2p3/2main})$) is an indicator of the amount of charge transferred, the larger the satellite peak (as indicated by a large $I_{ratio\ satel}$) the more charge is transferred from the ligand (C≡N-group) to the metal (in this case the Fe). The influence of the electron withdrawing property of the other metal (Fe in **B1**, Co in **B2**, Ni in **B3** and Cu in **B4**) as measured by σ_M, shows an inversely proportional relationship according to: $I_{ratio\ satel} = -5.03 + 9.78$, $R^2 = 0.905$ (see **Figure 3.14** (c)). Thus the more electron density that is pulled towards the other metal (Fe in **B1**, Co in **B2**, Ni in **B3** and Cu in **B4**) away from the ligand (C≡N-group), the less charge is transferred by the C≡N-group towards the iron.

During an electron transfer process, such as photoemission, the sample undergoes inner-sphere reorganization to compensate for the positively charged species that formed, according to the Franck-Condon principle.[16] This principle relates electronic transitions (like photoionization) to the intensity of the vibronic transitions (e.g. $I_{ratio\ satel}$ as measured by XPS). The $I_{ratio\ satel}$ (which represents the amount of charge transferred during photoionisation) is therefore also an indication of the degree of inner-sphere reorganization. The Franck-Condon principle states that the intensities of a spectroscopic peak (in this case XPS photoelectron line) is an indication of the nuclear coordinates. A more significant change in the nuclear coordinates (higher degree of inner-sphere reorganisation) induces a higher intensity of the photoelectron line (higher $I_{ratio\ satel}$). Corresponding to the above paragraph, as σ_M increases, $I_{ratio\ satel}$ decreases. This implies that the more electron density that is moved away from the Fe bound to C≡N-group (such as in **B3**), the smaller the degree of inner-sphere reorganisation will be (small $I_{ratio\ satel}$) after photoemission.

The electronic transitions referred to by the Franck-Condon principle, also includes UV absorption and vibrational excitations (e.g. the wavenumber of the vibration peaks as measured by ATR FTIR). Since wavenumber (as measured by ATR FTIR) is directly proportional to spatial frequency and photon energy, it can also be used as a measure of the energy required for the inner-sphere reorganisation. The energy needed for the inner-sphere reorganisation (as

indicated by *v*CO) is influenced by electron transfer process and in general as the ease of photoemission increases (as indicated by a lower $BE_{Fe2p3/2}$) the energy needed for inner-sphere reorganisation (as indicated by *v*CO) also increases (see **Table 3.4**). A comparison between *v*CO (an indicator of the energy required for inner-sphere reorganisation) and $I_{ratio\ satel}$ (an indicator of the degree of inner-sphere reorganisation), see **Figure 3.14** (e), shown that as the degree of inner-sphere reorganization increases, less energy is required for this inner-sphere reorganisation.

The comparative Fe 2p area of **N2-N4** as measured by XPS is shown in **Figure 3.15**. **N1** will not be included in the discussion, seeing as the TEM images indicated that **N1** was not nano-sized. The binding energy for the Fe $2p_{3/2}$ photoelectron lines for Fe^{II} of **N2-N4** was located at ca. 708.4 eV, which is ca. 0.2 eV lower than what was found for Fe^{II} of **B1-B4**. At the same time the binding energy for the Fe $2p_{3/2}$ photoelectron lines for Fe^{III} of **N2-N4** was located at ca.710.2 eV, which is ca. 0.3 eV higher than what was found for Fe^{III} of **B1-B4**. This implies that in the nano-sized particles, stabilised by AOT, Fe^{II} is more stable (lower binding energy), while Fe^{III} is less stable (higher binding energy) compared to the bulk-size metal hexacyanoferrates. The ΔBE_2 for the nano-sized metal hexacyanoferrates, **N2-N4**, are ca. 0.2 eV higher than for the bulk-sized metal hexacyanoferrates. This shows that the difference in the electronic environment between the Fe^{II} and Fe^{III} in **N2-N4**, is more than for **B1-B4**. The ratios between Fe^{II} and Fe^{III} (I_{ratio}) for the bulk-sized metal hexacyanoferrates range from ca. 0.5 to 1.8. The ratios between Fe^{II} and Fe^{III} (I_{ratio}) for the nano-sized metal hexacyanoferrates range from ca.0.8 to1.1. These ratios give an indication of which oxidation state (Fe^{II} and Fe^{III}) in the sample, is in the majority. While the amount of charge transferred from the ligand to the metal ($I_{ratio\ satel}$) are the same at 0.33. Most of the general trends (as described for **B1-B4** above) established for **N2-N4**, are similar to what was found for **B1-B4**, when **N1**, was not considered in any of the trends, since it was found that **N1** was not nano-sized.

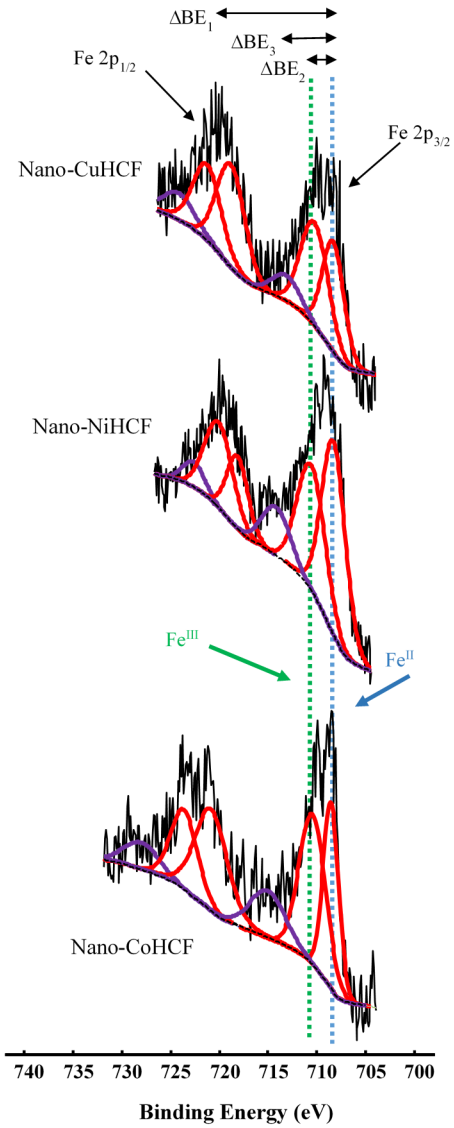

Figure 3.15: Comparative XPS spectra showing the simulated main Fe 2p (red) as well as the satellite peaks of the Fe 2p photoelectron lines (grey) of the nano-sized hexacyanoferrates.

The comparative XPS spectra of the simulated main M 2p peaks as well as the satellite peaks of M 2p photoelectron lines of the different prepared metal hexacyanoferrates can be found in the Appendix (Spectra 25 – 27). The individual XPS spectra of the simulated main N 1s and C 1s peaks as well as their satellite peaks of the different prepared metal hexacyanoferrates can be found in the Appendix (Spectra 9 – 24). The tabulated information regarding the C 1s photoelectron lines can be found in the Appendix, **Table A1**.

XPS examination of the 2p metal peaks revealed the presence of distinct substructures, see **Tables 3.4** (for Fe) and **3.5** (for Co, Ni and Cu). Regarding the Co $2p_{3/2}$ peak, the two main peaks are assigned to Co^{II} and Co^{III} based on the location of their binding energies at ca. 782.01

and 784.81 eV respectively, as well as literature.[21, 23] In reference to the position at ca. 855.77 and 858.01 eV for the two distinguishable Ni $2p_{3/2}$ peaks, they were allocated to Ni^{II} and Ni^{III}, respectively, since Ni^0 is normally positioned at ca. 852.80 eV,[24] and the allocations are also in accordance with reported values from literature.[25] As for the Cu $2p_{3/2}$ peak, the peaks found at ca. 933.00 and 935.71 eV were assigned to Cu^{I} and Cu^{II}, which correlates well reported data from literature.[26]

The XPS spectra of all non-iron metals also showed charge transfer peaks at a few eV higher than the main 2p photoelectron lines. The bulk-sized CoHCF showed a greater charge transfer ratio than the nano-sized CoHCF (values in **Table 3.5**). The same trend was observed for the CuHCF complexes. However, in the NiHCF complexes, the nano-sized NiHCF showed a greater charge transfer ratio than the bulk-sized NiHCF. In comparison to iron there exists a smaller charge transfer ratio between ligand and M than between ligand and iron. All the nano-sized complexes exhibited approximately the same charge transfer ratio between ligand and iron (ca. 0.33) and between ligand and M (ca. 0.16). The bulk-sized MHCF showed that in general the charge transfer ratio between ligand and metal was dependant on the Pauling electronegativity of the different metals.

From **Figures 3.12** and **3.15**, it is clear that in all prepared hexacyanoferrates, a mixture of Fe^{II} and Fe^{III} were found to be present.

The N $1s_{main}$ peak for the different metal hexacyanoferrates was measured between 397.13 and 398.79 eV, which correlates well with the binding energy position reported for other cyano-complexes.[18, 27, 28] The general trend (see **Table 3.4**) again shows that an increase in Pauling electronegativity of the metal, σ_M, induces an increase in the binding energy of the N $1s_{main}$ photoelectron line.

Table 3.4. The Binding energies of the maximum binding energy (BE) of the Fe $2p_{3/2\ 2}$ photoelectron lines, the spin orbit splitting of maximum BE of the Fe 2p photoelectron lines, ΔBE_1, BE of the satellite Fe $2p_{3/2}$ photoelectron line, as well as the peak separations between main Fe $2p_{3/2}$ and the satellite Fe $2p_{3/2}$, ΔBE_2, the ratio area % between main Fe $2p_{3/2}$ and the satellite Fe $2p_{3/2}$, I_{ratio}. The wavenumber of cyano group stretching frequency ν(C≡N).

Complex	Size	No	Pauling σ_M	BE Fe^{II} $2p_{3/2main}$ (eV)	BE Fe^{III} $2p_{3/2main}$ (eV)	ΔBE_1 [a] (eV)	ΔBE_2 [b] (eV)	I_{ratio} [c]	BE Fe $2p_{3/2main}$ [d] (eV)	BE Fe $2p_{3/2satel}$ [e] (eV)	ΔBE_3 [f] (eV)	$I_{ratio\ satel}$ [g]	ν(C≡N) (cm^{-1})	N $1s_{main}$ (eV)
Fe-C≡N-Fe	Bulk	**B1**	1.83	708.44	709.44	12.95	1.22	1.72	708.82	712.65	3.83	0.56	2060	397.62
	Nano	**N1**		708.38	710.5	13.15	2.12	0.78	710.25	712.87	2.62	0.58	2077	398.79
Fe-C≡N-Co	Bulk	**B2**	1.88	708.52	710.03	13.12	1.47	1.44	709.27	712.00	2.73	0.42	2107	397.87
	Nano	**N2**		708.18	709.6	13.12	1.42	0.86	709.27	711.78	2.51	0.32	2162,2100	397.70
Fe-C≡N-Ni	Bulk	**B3**	1.91	708.59	710.25	13.42	1.66	0.52	709.42	711.88	2.46	0.17	2162,2097	398.11
	Nano	**N3**		708.46	710.48	13.01	1.66	1.18	709.21	712.69	3.48	0.33	2165	398.70
Fe-C≡N-Cu	Bulk	**B4**	1.90	708.58	710.09	13.24	1.51	0.88	709.28	711.76	2.48	0.19	2100	398.45
	Nano	**N4**		708.42	710.4	13.11	1.8	1	709.2	712.5	3.3	0.34	2170,2099	397.13

[a] $\Delta BE_1 = BE_{Fe2p1/2main} - BE_{Fe2p3/2main}$. [b] $\Delta BE_2 = BE_{FeIII\ 2p3/2\ main} - BE_{FeII\ 2p3/2\ main}$. [c] I_{ratio} = ratio between the intensities of the Fe^{II} and Fe^{III} Fe $2p_{3/2}$ photoelectron lines ($I_{ratio} = (I_{FeII\ 2p3/2\ main})/(I_{FeIII\ 2p3/2\ main})$). [d] Maximum BE of the main Fe $2p_{3/2}$ envelope. [e] Maximum BE of the satellite Fe $2p_{3/2}$ envelope. [f] $\Delta BE_3 = BE_{Fe2p3/2satel} - BE_{Fe2p3/2main}$. [g] $I_{ratio\ satel}$ = ratio between the intensities of the satellite and main Fe $2p_{3/2}$ photoelectron lines ($I_{ratio} = (I_{Fe2p3/2satel})/(I_{Fe2p3/2main})$).

Table 3.5: The BE of the maximum BE of the nitrogen coordinated metal (M) $2p_{3/2}$ photoelectron lines, the spin orbit splitting of maximum BE of M 2p photoelectron lines, ΔBE_1, BE of the satellite M $2p_{3/2}$ photoelectron line, as well as the peak separations between main M $2p_{3/2}$ and the M metal $2p_{3/2}$, ΔBE_2, the ratio area % between main M $2p_{3/2}$ and the satellite M $2p_{3/2}$, I_{ratio}. M = Co, Ni or Cu.

Complex	**Size**	**No**	**Pauling σ_M**	**M**	**BE M^{II} $2p_{3/2main}$ (eV)**	**BE M^{III} $2p_{3/2main}$ (eV)**	**ΔBE_1 [a] (eV)**	**ΔBE_2 [b] (eV)**	**I_{ratio} [c]**	**BE M $2p_{3/2main}$ [d] (eV)**	**BE M $2p_{3/2satel}$ [e] (eV)**	**ΔBE_3 [f] (eV)**	**I_{ratio} [g]**
Fe-C≡N-Co	Bulk	**B2**	1.88	Co	782.01	784.81	15.46	2.80	2.89	782.16	786.42	4.25	0.29
	Nano	**N2**		Co	781.45	784.57	15.83	3.12	2.00	781.46	784.17	2.71	0.16
Fe-C≡N-Ni	Bulk	**B3**	1.91	Ni	855.78	856.97	17.53	1.19	0.48	856.20	863.19	6.98	0.13
	Nano	**N3**		Ni	855.77	858.01	17.67	2.24	1.11	856.70	862.67	5.97	0.19
Fe-C≡N-Cu	Bulk	**B4**	1.90	Cu	933.00	935.71	19.73	2.71	1.24	933.97	943.71	9.74	0.24
	Nano	**N4**		Cu	932.52	935.18	19.64	2.66	0.51	934.64	944.71	19.64	0.13

[a] $\Delta BE_1 = BE_{M2p1/2main} - BE_{M2p3/2main}$. [b] $\Delta BE_2 = BE_{MIII\ 2p3/2\ main} - BE_{MII\ 2p3/2\ main}$. [c] I_{ratio} = ratio between the intensities of the M^{II} and M^{III} Fe $2p_{3/2}$ photoelectron lines ($I_{ratio} = (I_{MII\ 2p3/2\ main})/(I_{MIII\ 2p3/2\ main})$).[d] Maximum BE of the main M $2p_{3/2}$ envelope. [e] Maximum BE of the satellite M $2p_{3/2}$ envelope. [f] $\Delta BE_3 = BE_{M2p3/2satel} - BE_{M2p3/2main}$. [g] I_{ratio} = ratio between the intensities of the satellite and main M $2p_{3/2}$ photoelectron lines ($I_{ratio} = (I_{M2p3/2satel})/(I_{M2p3/2main})$).

3.3.5 Thermal gravimetric analysis

From TGA it is possible to measure the weight loss as a function of increase in temperature. During this study the thermal stability of the prepared compounds were measured over a temperature range of 25 °C – 500 °C. All samples were heated at a rate of 10 °C·min^{-1}, whilst an inert argon atmosphere was maintained over the system. **Figure 3.16** and **3.17** depicts the TGA of **B1-B4** and **N2-N4**, respectively, while the weight loss and decomposition data are tabulated in **Tables 3.6** and **3.7**. The TGA curve for **N1** can be found in the appendix (Spectrum 5), it is not part of the discussion since it was found not to be nano-sized according to the TEM images (in section **3.3.1.2**). The detailed and integrated TGA spectra of all individual complexes can be found in the appendix (Spectra 1 – 8).

The weight loss of the different metal hexacyanoferrates (**B1-B4** and **N2-N4**) upon heating could be categorised into three stages, room temperature to ~200 °C (stage 1), ~200 to ~300 °C (stage 2) and from ~300 °C onwards. These three stages is grouped as three global pyrolytic processes, each comprising of a few overlapping steps. The total weight loss for **B1-B4** and **N2-N4** ranged between 18 % and 75%, while the weight loss for the three individual stages ranged from 2 % to 34 %. The weight loss during each stage is explained in accordance with literature.[8] The first stage (up to ~200 °C) is due to the evaporation of water adsorbed onto the external surface of the particles. During the second stage (~200 to ~300 °C) water, which was trapped inside the interstitial spaces, is removed (see **Table 3.6** for the exact amounts of water that evaporated). The third stage (extending from ~300 °C up to 500 °C - it was only measured up to 500 °C), was found to be due to the decomposition of the organic binder, causing further weight loss especially in the bulk-sized material.

Table 3.6: Amount of water lost due to evaporation.

Sample	Mass loss		Water evaporated during stage 1 (mole)	Water evaporated during stage 2 (mole)
	Stage 1	Stage 2		
B1	0.00148	0.0019	8.22222 X10^{-5}	0.000105556
B2	0.00212	0.00068	0.000117778	3.77778 X10^{-5}
B3	0.0014	0.00065	7.77778 X10^{-5}	3.61111 X10^{-5}
B4	0.00124	0.00016	6.88889 X10^{-5}	8.88889 X10^{-5}
N1	0.00171	0.00251	0.000095	0.000139444
N2	0.00096	0.00012	5.33333 X10^{-5}	6.66667 X10^{-5}
N3	0.00033	0.00012	1.83333 X10^{-5}	6.66667 X10^{-5}
N4	0.000791	0.001065	4.39444 X10^{-5}	5.91611 X10^{-5}

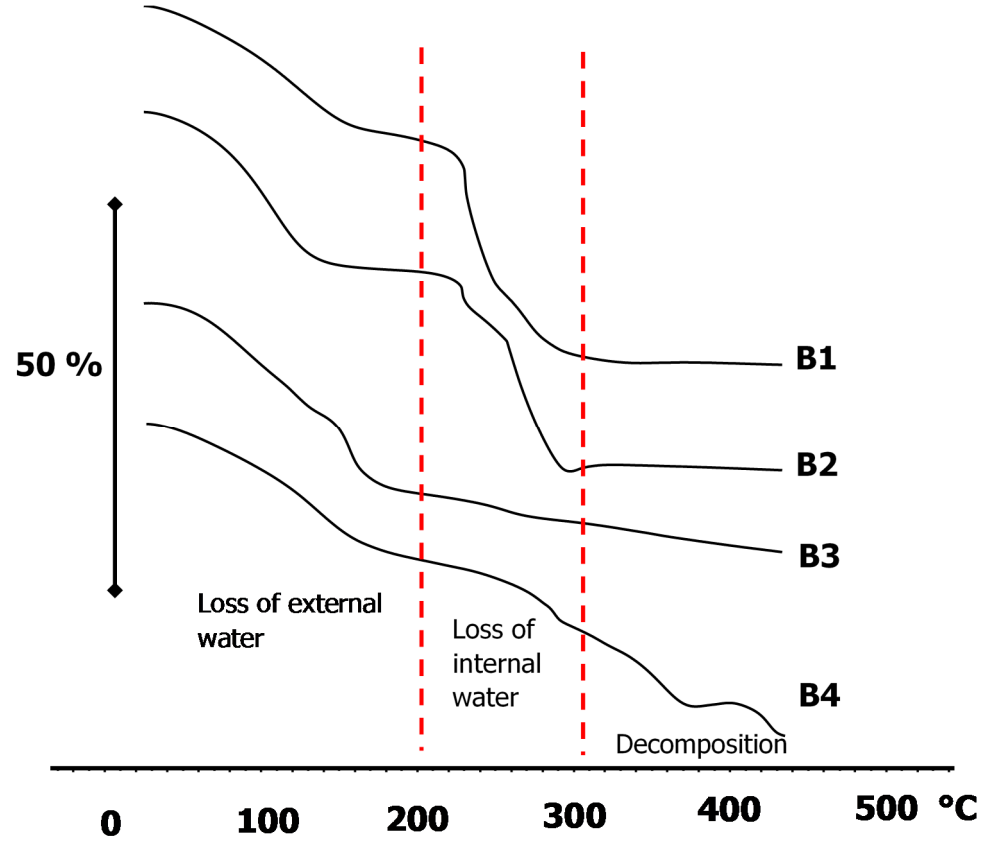

Figure 3.16: The comparative TGA thermograms of the metal hexacyanoferrate bulk composites **B1**-**B4**.

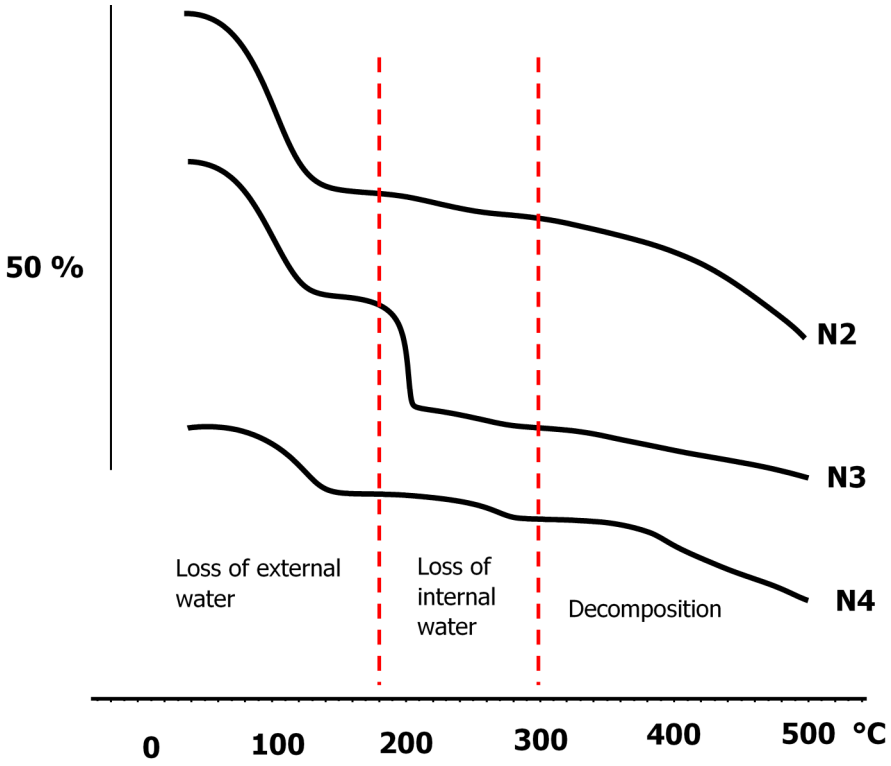

Figure 3.17: The comparative TGA thermograms of the metal hexacyanoferrate nanocomposites **N2**-**N4**.

The total percentage mass loss of each prepared compound during thermal gravimetric analysis can be found in the Appendix under the TGA section as well as **Tables 3.7** and **3.8**.

As mentioned in section **3.3.3**, external water can be detected between 3100 - 3600 cm^{-1}, which is the OH stretching frequencies of the water molecules adsorbed on the outside, while the internal water can be detected at ca. 1600 cm^{-1}, which is the δ(HOH) bending vibration of water molecules that are trapped within the interstitial spaces.[8] It should thus be possible to confirm the three different stages of mass loss by ATR FTIR. As an example, **B4** will be discussed, the ATR FTIR measured after heating to different temperatures are shown in **Figure 3.18**. After **B4** was subjected to temperatures up to 200 °C the broad peak at ca. 3500 cm^{-1} disappeared. Since the OH stretching frequencies detected at 3100 - 3600 cm^{-1} is associated with water molecules adsorbed on the outside, stage one of the mass loss is confirmed to be loss of the external water from the metal hexacyanoferrate. After **B4** was subjected to temperatures up to 300 °C the peak indicating internal water molecules at ca. 1500 cm^{-1} disappeared,[29] validating that stage two is the removal of the water trapped inside the metal hexacyanoferrate polymer structure.

The third stage starting at ca. 300 °C was only measured up to ca 500 °C. Following the heating of **B4** at 500 °C for 0.2 h, the ATR FTIR revealed that the C≡N stretching frequencies between 2050 and 2200 cm^{-1} disappeared, thereby confirming that the third stage of mass loss during the TGA belongs to the decomposition of the metal hexacyanoferrate and the CN organic linker. Comparing the measured % weight left (100% - total weight loss %) and the calculated amount of metal oxide that remains after heating, it was found that for **B1** and **B4** not all the metal hexacyanoferrate sample decomposed to the metal oxide, and that some CN-groups still remain. For **B2** and **B3** decomposition to a combination of the different possible oxides, are within experimental error the same as the calculated %. The % metal oxide calculated for **N1-N4**, was calculated assuming that for every metal hexacyanoferrate there is one AOT molecule (the stabilizing surfactant). Even when the AOT molecule was omitted from the calculations, the measured % left and the calculated % metal oxides that can form are far apart, the measured % is 6-8 times more than the calculated value (excluding **N1**). It can thus be assumed that AOT still remains as part of the % measured weight.

Table 3.7: Total weight loss determined by thermogravimetric analysis.

Complex	Size	No	Total weight loss %	Measured % weight left	% Metal oxide calculated	
Fe-C≡N-Fe	Bulk	**B1**	46.23	53.77	40.9 FeO 44.6 Fe_2O_3 43.9 Fe_3O_4	
	Nano	**N1**	74.46	25.54	21.2 FeO 23.1 Fe_2O_3 22.8 Fe_3O_4	
Fe-C≡N-Co	Bulk	**B2**	46.29	53.71	27.6 FeO 30.1 Fe_2O_3 29.7 Fe_3O_4	28.8 CoO 31.9 Co_2O_3 30.8 Co_3O_4
	Nano	**N2**	34.74	65.26	9.5 FeO 10.3 Fe_2O_3 10.2 Fe_3O_4	9.8 CoO 10.9 Co_2O_3 10.6 Co_3O_4
Fe-C≡N-Ni	Bulk	**B3**	40.58	59.42	26.8 FeO 29.3 Fe_2O_3 28.9 Fe_3O_4	27.9 NiO 30.9 Ni_2O_3
	Nano	**N3**	18.68	81.32	10.6 FeO 11.6 Fe_2O_3 11.4 Fe_3O_4	11.0 NiO 12.2 Ni_2O_3
Fe-C≡N-Cu	Bulk	**B4**	32.43	67.57	24.1 FeO 26.3 Fe_2O_3 26.0 Fe_3O_4	24.0 Cu_2O 26.7 CuO 29.4 Cu_2O_3
	Nano	**N4**	33.93	66.07	6.9 FeO 7.5 Fe_2O_3 7.4 Fe_3O_4	5.6 Cu_2O 7.6 CuO 8.4 Cu_2O_3

Table 3.8: Specific weight loss determined by thermogravimetric analysis of the different stages of heating.

Complex	Size	No	Temperature (°C)	% mass loss	Temperature (°C)	% mass loss	Temperature (°C)	% mass loss
Fe-C≡N-Fe	Bulk	**B1**	0 – 199.19	16.28	199.19 – 292.43	20.85	292.43-496.61	9.10
	Nano	**N1**	0 – 204.83	23.33	204.83 – 294.02	34.22	294.02 – 494.69	16.91
Fe-C≡N-Co	Bulk	**B2**	0 – 178.75	19.92	178.75 – 273.28	6.42	274.23 – 493.56	19.95
	Nano	**N2**	0 – 169.04	19.15	169.04 – 274.27	2.39	274.27 – 492.33	13.20
Fe-C≡N-Ni	Bulk	**B3**	0 – 235.77	18.02	235.77 – 337.40	8.45	337.40 – 496.38	14.11
	Nano	**N3**	0 - 166	7.19	166 – 297.12	2.71	297.12 – 493.76	8.78
Fe-C≡N-Cu	Bulk	**B4**	0 – 226.49	24.7	226.49 – 317.12	3.27	317.12 – 493.52	4.46
	Nano	**N4**	0 – 146.51	14.46	146.51 – 490.58	19.47	N.A.	N.A.

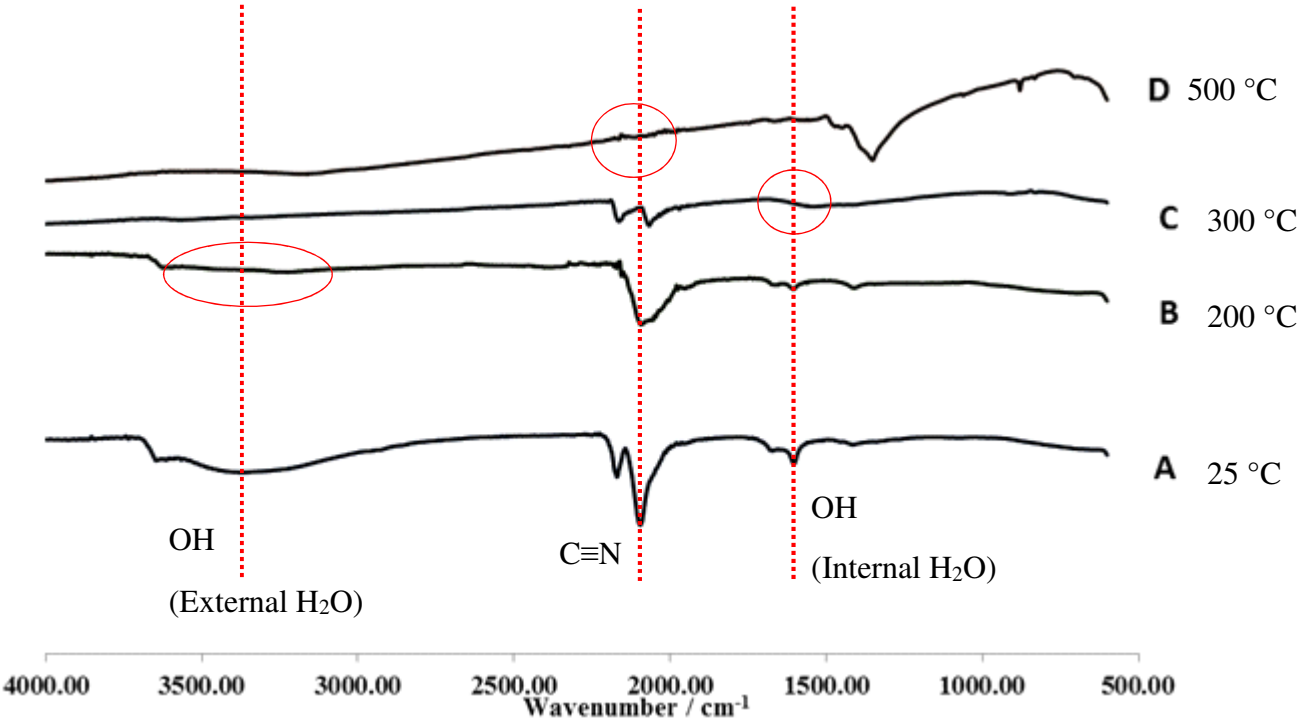

Figure 3.18: Comparative FT-IR spectra of bulk-sized copper hexacyanoferrate (B4) at (A) room temperature, (B) 200 °C, (C) 3200 °C and (D) 500 °C.

3.3.6 Differential Scanning Calorimetry

The DSC of **B1-B4** and **N1-N4** was measured (heating and cooling at a rate of 10 °C min^{-1} under inert argon atmosphere) to investigate the structural variations that occurred upon thermal change. Complexes **B1-B2** and **N1** showed no thermal activity, while **N2** only showed one endothermic peak in the heating cycle at 434.78 °C, which is the onset of decomposition. Since no thermal activity (as measured by DSC) could be detected around the temperature where loss of water (external and internal, as measured by TGA) occurred, it can be assumed that there are no structural changes during the loss of water in **B1-B2** and **N1**. From the TGA data of **B1**, it was concluded that there are still CN-groups present (decomposition was not complete), which is supported by the DSC data which shows no structural changes.

The DSC curve of nano-CuHCF (**N4**), is shown as an example in **Figure 3.19** (the DSC curves of **B1-B4** and **N1-N3** are shown in the Appendix, Spectra 28 - 34). During the heating cycle of **N4**, two endothermic peaks was observed at 173.05 °C and 290.1 °C, respectively. The peak at 173.05 °C (onset temp 101.29 °C) is assigned to the evaporation of water molecules on the outside of the particles, while the peak at 290.12 °C (onset temp 242.11 °C) is assigned to the loss of water which was trapped in the interstitial spaces, also discussed in thermal gravimetric analysis (see section **3.3.5**). An additional exothermic peak is observed at 426.6 °C, which is assigned to some decomposition starting to occur. During the cooling cycle an exothermic (397.30 °C) and endothermic (161.50 °C) solid state transition occurred, this is probably due to the structural changes that occur after the loss of internal and external water. **B3** showed a similar thermal activity pattern as **N4**, the two endothermic peaks at 204.21°C and 332.45 °C are assigned to the loss of external and internal water, while the endothermic peak at 417.82 °C is the start of decomposition. The cooling cycle showed two exothermic solid state transitions at 408.02 °C and 214.10 °C.

N3 and **B4** showed on peak in the heating cycle (endothermic at 409.73 °C for **N3**, and exothermic at 435.40 °C for **B4**), which is assigned to the onset of decomposition. The absence of thermal activity at lower temperatures during the heating cycle indicates that the loss of water does not induce structural change within **N3** and **B4**. During the cooling cycle both **N3** and **B4** showed an endothermic peak at 446.97 °C and 409.62 °C, respectively, which is attributed to some decomposition products. The exothermic peak at 136.12°C for **N3**, and the endothermic peak at 319.34°C for **B4** is associated with a solid state transitions occurring due to the loss of water (internally and externally).

Table 3.9: DSC data obtained during the heating cycles of all prepared hexacyanoferrates.

Complex	Size	No	Temp. (°C)	Energy (mJ)	Temp. (°C)	Energy (mJ)	Temp. (°C)	Energy (mJ)
Fe-C≡N-Fe	Bulk	**B1**	-	-	-	-	-	-
	Nano	**N1**	-	-	-	-	-	-
Fe-C≡N-Co	Bulk	**B2**	-	-	-	-	-	-
	Nano	**N2**	-	-	-	-	434.78	-328.07
Fe-C≡N-Ni	Bulk	**B3**	204.21	-199.50	332.45	-0.62	417.82	-52.92
	Nano	**N3**	-	-	-	-	409.73	-129.40
Fe-C≡N-Cu	Bulk	**B4**	-	-	-	-	435.40	51.86
	Nano	**N4**	173.05	-72.79	290.12	-3.15	426.66	22.53

Table 3.10: DSC data obtained during the cooling cycles of all prepared hexacyanoferrates.

Complex	Size	No	Temp. (°C)	Energy (mJ)	Temp. (°C)	Energy (mJ)
Fe-C≡N-Fe	Bulk	**B1**	-	-	-	-
	Nano	**N1**	-	-	-	-
Fe-C≡N-Co	Bulk	**B2**	-	-	-	-
	Nano	**N2**	-	-	-	-
Fe-C≡N-Ni	Bulk	**B3**	408.02	67.08	214.10	4.87
	Nano	**N3**	446.97	-17.33	136.21	11.45
Fe-C≡N-Cu	Bulk	**B4**	409.62	-0.41	319.34	-14.97
	Nano	**N4**	397.30	21.20	161.50	-32.62

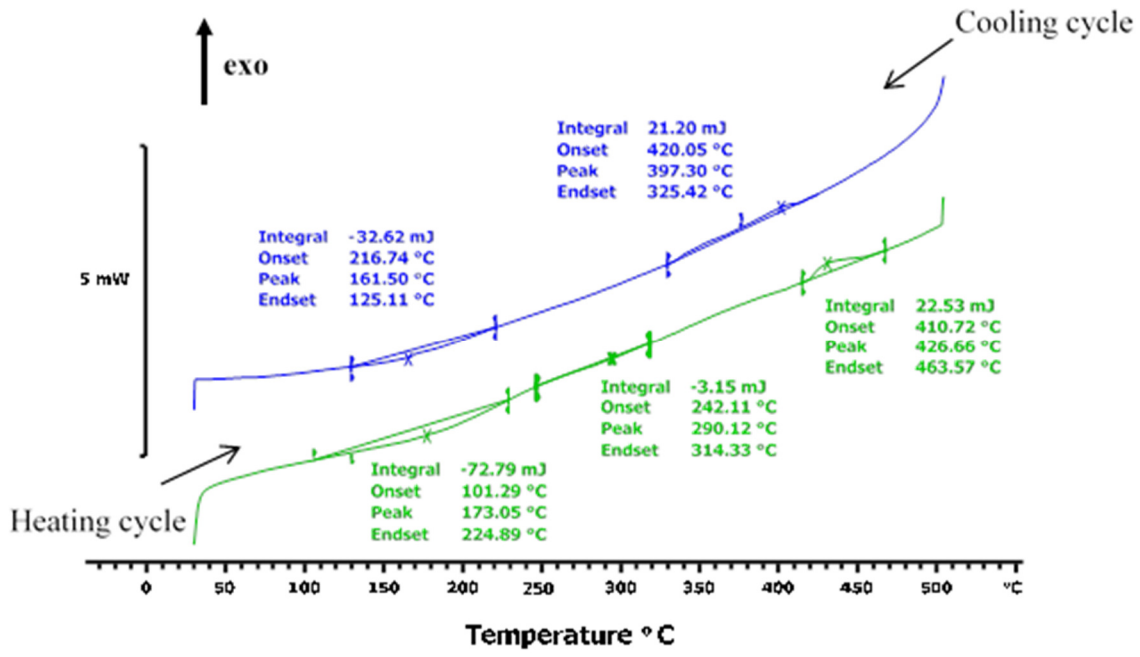

Figure 3.19: Single DSC heating/cooling cycle of **N4** (nano-CuHCF).

3.3.7 Electrochemistry

Normal solution electrochemistry could be not conducted on these metal hexacyanoferrates since they are insoluble in water and organic solvents. Therefore "solid state" electrochemistry needed to be employed to investigate the electrochemical properties of these metal hexacyanoferrates. As an example, cobalt hexacyanoferrate (both **B2** and **N2**) was electrochemically evaluated. The electrochemical properties of cobalt hexacyanoferrate was investigated by the physical coating of a glassy carbon electrode surface with the cobalt hexacyanoferrates **B2** and **N2** (followed by nafion coating, to ensured that the sample material was firmly kept in place while still maintaining electrical conductance for the duration of the electrochemical experiments), to yield electrode **GCB2** and **GCN2**. The electrochemical property of cobalt hexacyanoferrate was further investigated by electrodeposition, similar to electroplating from a solution containing the starting materials (potassium hexacyanoferrate and cobalt nitrate) to yield electrode **GCED**. Modified carbon paste electrodes were also prepared from a mixture of graphite and **B2** or **N2** to yield electrodes **CPB2** and **CPN2**. All these modified electrodes will involve solid-state electrochemistry of **B2** and **N2**. The background of these electrodes was recorded in both water and acetonitrile and the influence of the modified electrode on the fast electron transfer process of ferrocene (in acetonitrile) was also investigated. Lastly, the electrocatalytic oxidation of hydrazine will also be reported.

3.3.7.1 Electrochemical characterisation of modified glassy carbon electrodes

To determine the electrochemical properties of both the **GCB2** and **GCN2** electrodes, a background was recorded in a water/KCl mixture (0.1 M KCl, acting as the supporting electrolyte) and acetonitrile/tetra-*n*-butylammonium hexafluorophosphate (0.1 M $TBAPF_6$, acting as the supporting electrolyte) to find the electrochemical response of the cobalt hexacyanoferrate modified electrode itself (the cobalt hexacyanoferrate).

Tables 3.11 and **3.12** summarises the electrochemical data recorded of **GCB2** and **GCN2** in H_2O/KCl and CH_3CN/ $TBAPF_6$, respectively (see **Figure 3.20** left (a) and right (b)).

Table 3.11: Electrochemical response data recorded of **GCB2** and **GCN2** in H_2O/KCl, (from **Figure 3.20** left).

Electrode	E_{pa} (mV)	E_{pc} (mV)	ΔE (mV)	i_{pa} (μA)	i_{pc} (μA)	i_{pc}/i_{pa}	$E°'$ (mV)
GCB2+ nafion	608	425	183	5.2	2.75	0.53	516.5
GCN2+ nafion	381.5	157	224.5	61	51	0.84	269.25

Table 3.12: Electrochemical response data recorded of **GCB2** and **GCN2** in CH_3CN/ $TBAPF_6$ (from **Figure 3.20** right (b)).

Electrode	E_{pc1} (mV)	E_{pc2} (mV)	i_{pc1} (μA)	i_{pc2} (μA)
GCB2 + nafion	**306**	**-451**	**40**	**-**
GCN2 + nafion	**-**	**-**	**-**	**-**

As expected the neat glassy carbon electrode does not show any electrochemical response in both the H_2O/KCl and CH_3CN/ $TBAPF_6$ solutions (See **Figure 3.20** left and right). Reported data of cobalt hexacyanoferrate paraffin-impregnated graphite electrode, showed only one redox couple (at 585 mV) which was assigned to the Fe^{II}/Fe^{III} couple,[30] in accordance with this, the electrochemical response for both **B2** and **N2** modified glassy carbon electrodes, in water/0.1 M KCl, was also assigned to the Fe^{II}/Fe^{III} couple. This redox process indicated an electrochemical irreversible Fe^{II}/Fe^{III} couple with ΔE > 150mV. However, in both cases (**GCB2** and **GCN2**) the Fe^{II}/Fe^{III} couple was found to be chemically reversible with $i_{pa}/i_{pc} \approx 1$. No cobalt oxidation or reduction could be detected, this Co^{II}/Co^{III} couple is

normally found at ca. 0.52 mV.[31, 32] Literature has shown that the redox process related to the Co^{III}/Co^{II} couples only occurs for compounds that crystallised in the insoluble form. The insoluble form presents defects caused by the absence of ¼ of the $Fe(CN)_6$ groups, replaced by water molecules. This allows swelling of the structure with the contraction of the Co-N bond while reducing to Co^{II}.[32] This implies that the modified glassy carbon electrodes prepared in this study did not crystallise in the insoluble form. The current response of the **GCN2** electrode was ca. ten times larger than was found for the GC**B2** electrode. This significant increase in current response is attributed to the larger surface area of the nano-sized cobalt hexacyanoferrate in comparison to the bulk-size. A larger surface area would lead to more charge being transferred, which causes this large current at the maximum oxidation potential peak.[31, 32] It would also seem that referenced to a standard Ag/AgCl electrode that the **GCN2** electrode is easier to oxidise than the **GCB2** electrode by about 210 mV. This can be due to the presence of surface defects that act as a local trap for electrons, thereby allowing oxidation and reduction at milder potential values.[33]

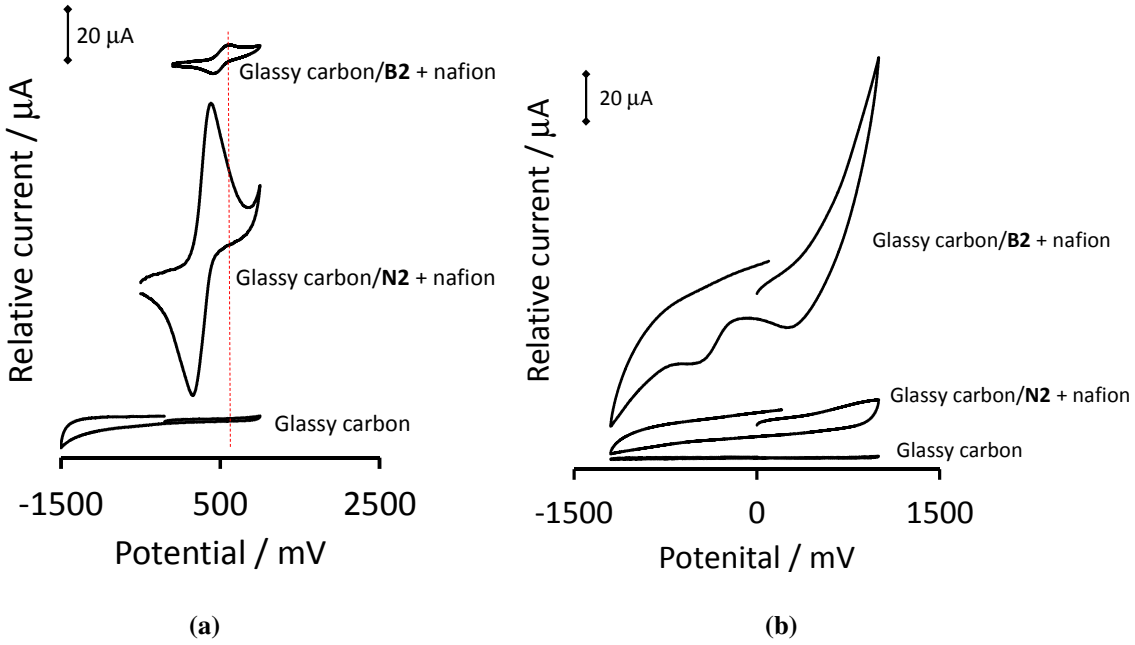

Figure 3.20. Left (a): Comparative cyclic voltammogram showing the background in water/0.1 M KCl at 25°C and scan rate of 100 mV.s-1 of (top) **GCB2** electrode (top coated with nafion), (middle) **GCN2** electrode (top coated with nafion) and (bottom) a neat glassy carbon electrode. Right (b): Comparative cyclic voltammogram showing the background in acetonitrile/0.1 M $TBAPF_6$ at 25°C and scan rate of 100 mV.s-1 of (top) **GCB2** electrode (top coated with nafion), (middle) **GCN2** electrode (top coated with nafion) and (bottom) a neat glassy carbon electrode.

In acetonitrile the neat glassy carbon electrode does not show a current response to the change in potential. The **GCN2** electrode showed a very small oxidation peak at 87 mV with a reduction peak at -272 mV. It is known from normal liquid phase electrochemistry that different solvents leads to a shift

in the oxidation potential, for the data obtained here, it can be seen that referenced against Ag/AgCl (in both water and acetonitrile) the Fe^{II}/Fe^{III} couple is oxidised much easier in acetonitrile than in water, but in acetonitrile the current response is very poor. The CV of **GCB2** electrode however reveal two reduction peaks at ca. 304 mV and -461 mV with no oxidation peaks. Seeing as in water the oxidation of the bulk-size is more difficult than the nano-size, it might be concluded that the oxidation of the bulk-sized would again be at higher potentials. Thus it might be that the oxidation is outside the potential window of the acetonitrile, and that the large increase in current before cycling to lower potentials indicates either the solvent decomposition and/or the start of the oxidation peak of the Fe^{II}/Fe^{III} couple. The first of the two reduction peaks at ca. 304 mV is attributed to the reduction peak of the Fe^{II}/Fe^{III} couple (of the small amount which was oxidised and/or the Fe^{III} which is also present), and the second peak at ca. -461 mV could possibly be attributed to the reduction of an *insitu* formed species between the oxidised cobalt hexacyanoferrate and the acetonitrile, which is known to form coordination to oxidised species during the CV experiment.[34]

The difference in current response of the modified electrodes in different solvents are due to the interaction of the applicable solvent with the dissolved species. These interactions between solvent and solute can be considered as donor-acceptor interactions. Solvent molecules can act as donors towards acceptors such as cations in solution and as acceptors toward donors such as anions. Different solvents can lower the oxidation potential.[35] It has also been shown that peak currents tend to decrease when different electrolyte containing solutions (NaCl or LiCl instead of KCl) was used, suggesting less reversibility of the voltammetric behaviours of the CoHCF films.[31]

Figure 3.21 shows the CV of **GCN2** electrode at different scan rates ranging from 10 – 1000 $m.s^{-1}$. The peak current for the oxidation and reduction of the Fe^{II}/Fe^{III} couple is described by the Randles-Sevcik equation:[36]

$$i_p = (2.69x10^5)n^{\frac{3}{2}}AD^{\frac{1}{2}}C\upsilon^{\frac{1}{2}}$$

where n is the amount of electrons transferred (one electron per phosphorus moiety), A is the area of the electrode in cm^2, D is the diffusion coefficient in $cm^2.s^{-1}$, C is the concentration of the analyte and υ is the scan rate measured in $V.s^{-1}$. Even though the Fe^{II}/Fe^{III} couple ligand system was electrochemical irreversible, a linear relationship was obtained between i_p and $\upsilon^{1/2}$ (see **Figure 3.21**, middle **(b)**). This showed that no major structural changes occurred in the cobalt hexacyanoferrate during the oxidation

and reduction processes. The slope of the graph for the cathodic and anodic peak *vs* (scan rate)$^{1/2}$ = 6.87 and -5.92 µA.(mV.s^{-1})$^{1/2}$ respectively.

The stability of the **GCN2** modified glassy carbon electrode was tested by cycling the potential forty times (see **Figure 3.21**, right **(c)**) in a water/0.1 M KCl solution, which indicates that no decomposition occurs and that the **N2** modified glassy carbon electrode is stable. There is however a small shift to lower potentials as the cycling continues. This occurrence can be ascribed to the presumption that some (very little) starting nano-compound is converted to a bulk-like species. This leads to a shift in the potential values as well as some differences in the current values.[32]

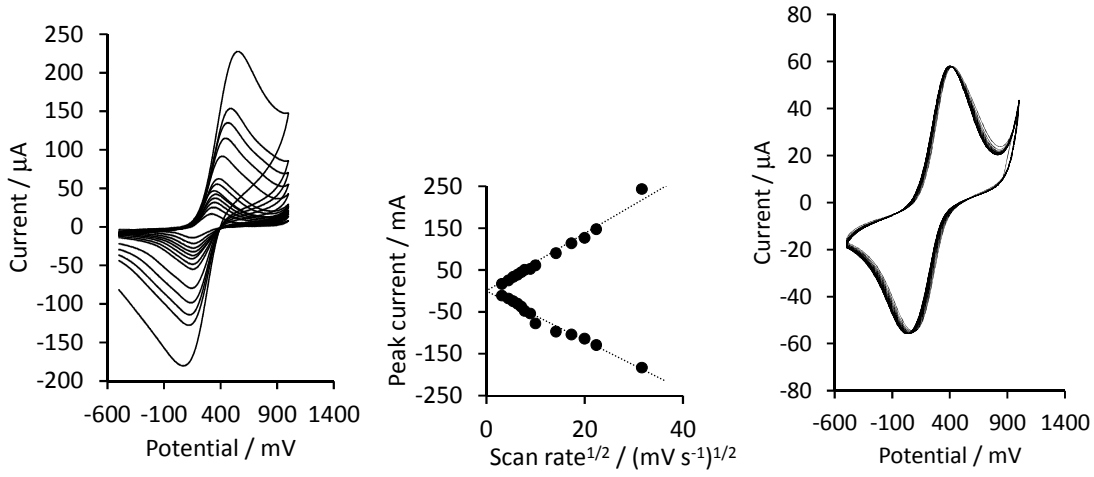

Figure 3.21: Left **(a)**: Stability scan at 100 mV.s-1 for 40 scans. CV of N2 at scan rate ranging from 10 mV.s^{-1} to 1000 mV.s^{-1}. Middle **(b)**: Graph illustrating the linear relationship between the anodic and cathodic peak currents and (scan rate)$^{1/2}$. Right **(c)**: Stability scan at 100 mV.s^{-1} for 40 scans.

3.3.7.2 Electrochemical characterisation of electrodeposited cobalt hexacyanoferrate on glassy carbon electrode

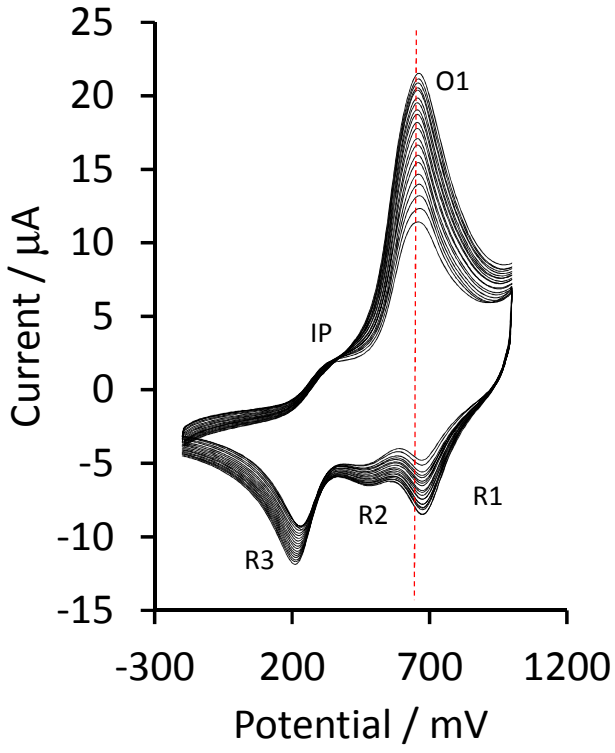

Figure 3.22: Cyclic voltammogram of CoHCF electrodeposited from a solution of $K_3[Fe(CN)_6]$ and Cobalt nitrate in water. 40 cycles at 100 $mV.s^{-1}$ scan rate to yield electrode **GCED**.

The electrochemical behaviour of CoHCF-electrodeposited modified glassy carbon electrode (**GCED**) was investigated and characterised by cyclic voltammetry. **Figure 3.22** shows consecutive CV scans of the electrodeposition of CoHCF material from $K_3(Fe(CN)_6)$ and $Co(NO3)_3$ in a 0.1 M KCl electrolyte solution in water onto the glassy carbon electrode surface. Table 3.12 summarises the electrochemical data recorded in H_2O/KCl of the electrodeposited CoHCF glassy carbon electrode (**GCED**).

Table 3.13: Electrochemical response data recorded of **GCED** in H_2O/KCl (from **Figure 3.22**).

Complex	Peak No	E_{pa} (mV)	E_{pc} (mV)	ΔE (mV)	i_{pa} (μA)	i_{pc} (μA)	i_{pc}/i_{pa}	$E°'$ (mV)
CoHCF electrodeposited	IP	322	-	-	2.4	-	-	-
	O1	656	472 (R2)	184	4.6	0.9	0.2	564
	R1	-	675	-	-	0.9	-	-
	R2	-	472	-	-	0.9	-	-
	R3	-	231	-	-	3.9	-	-

As the number of cycled scans increased, the current for both the reduction and oxidation peaks also increased, which is indicative of a deposited film that grows in thickness.

The peak marked IP at 322 mV is an isopotential point, which is the result of an allowed cross reaction (the formation of the cobalt hexacyanoferrate) and/or the interconversion of two electroactive surface adsorbates (in this case the $K_3[Fe(CN)_6]$ and $Co(NO_3)_3$).[37]

The background scan of the freshly prepared **GCED** (by electrodeposition) in a water/0.1 M KCl solvent mixture together with the background scans of an unmodified (neat) glassy carbon electrode are shown in **Figure 3.23**. Literature has shown that CoHCF can produce two redox couples for Co^{III}/Co^{II} and Fe^{III}/Fe^{II}. The Co^{III}/Co^{II} reduction occurs at a lower potential whereas the Fe^{III}/Fe^{II} transition occurs at a higher potential.[31] Reported data for a similar CoHCF modified glassy carbon electrode in a water/KCl solvent system, revealed two redox couples with the Epa at 510 and 660 mV for:

$$K_2Co^{II}[Fe^{II}(CN)_6] \leftrightarrow KCo^{III}[Fe^{II}(CN)_6] + K^+ + e^- \quad \text{(at 510 mV)}$$

$$KCo^{II}_{1.5}[Fe^{II}(CN)_6] \leftrightarrow Co^{II}_{1.5}[Fe^{III}(CN)_6] + K^+ + e^- \quad \text{(at 660 mV)}$$

Based upon these reported data peaks O1 and R1 (at 667 mV) was assigned to the Fe^{II}/Fe^{III} couple, while the reduction peak R2 (at 474 mV) was assigned Co^{II}/Co^{III} couple. Our CoHCF-electrodeposited modified glassy carbon electrode did not show an oxidation peak for the Co^{II}/Co^{III} couple, which could

be attributed to the possibility that crystallisation of the CoHCF in the soluble form on the glassy carbon electrode. The Co^{II}/Co^{III} redox couples only occurs when it is crystallised in the insoluble form.[32]

In acetonitrile the unmodified glassy carbon electrode again does not show a current response to the change in potential. The **GCED** electrode showed one oxidation peak (O1 at 788 mV) and three reduction peaks (R1 at 926 mV, R2 at 239 mV and R3 at -800 mV). Considering that for metal hexacyanoferrates, the Fe^{II} and/or Fe^{III} centers is always electrochemically active,[32] while Co^{III}/Co^{II} couple are only electrochemically active in its insoluble form, O1 are assigned to the Fe^{II}/Fe^{III} couple. In accordance with the assignments made in section 3.3.8.1 for the **GCB2** and **GCN2** electrodes, peak R2 is assigned to the reduction of Fe^{III} back to Fe^{II} and is thus coupled to O1. Under these circumstances this FeII/FeIII couple is chemically and electrochemically irreversible. Peak R3 in correlation with section **3.3.8.1** is assigned to the reduction of Co^{III}, similar to the data recorded in water/KCl, this reduction peak does not display an oxidation peak, again confirming that the insoluble crystal form. The reduction peak at 926 mV marked R1 has not been reported in literature, but it might be attributed to a Co^{III}/Co^{IV} couple.

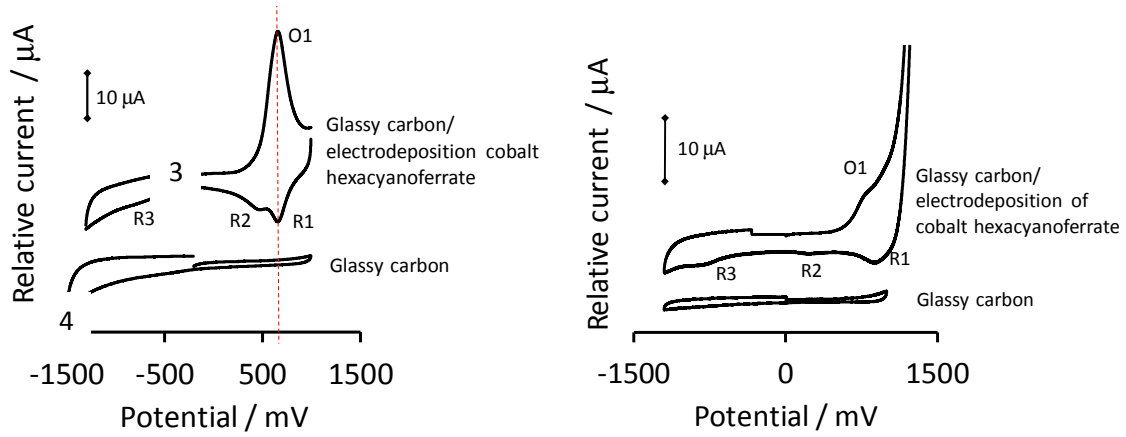

Figure 3.23: Left: Comparative cyclic voltammogram showing the background in H_2O/0.1 M KCl at 25°C and scan rate of 100 $mV.s^{-1}$ of (top) the **GCED** electrode, and (bottom) neat glassy carbon electrode. Right: Comparative cyclic voltammogram showing the background in acetonitrile/0.1 M $TBAPF_6$ at 25°C and scan rate of 100 $mV.s^{-1}$ of (top) the **GCED** electrode, and (bottom) neat glassy carbon electrode.

Table 3.14: Electrochemical data of the **GCED** electrode in H_2O/0.1 M KCl and acetonitrile/0.1 M $TBAPF_6$.

Solvent system	**O1 (mV)**	i_{pa} **(μA)**	**R1 (mV)**	i_{pc} **(μA)**	**R2 (mV)**	i_{pc} **(μA)**	**R3 (mV)**	i_{pc} **(μA)**
water/0.1 M KCl	**668**	**31**	**667**	**5**	**474**	**1**	**-844**	**3**
acetonitrile/0.1 M $TBAPF_6$	**788**	**5**	**926**	**1**	**239**	**0.2**	**-800**	**1**

3.3.7.3 Electrochemical characterisation of modified carbon paste electrodes

A series of carbon paste electrodes modified with, **B2** (to yield electrode **CPB2**) and **N2** (to yield electrode **CPN2**), were also prepared and their electrochemical response evaluated.

To determine the electrochemical properties of the metal hexacyanoferrate modified carbon paste electrodes, **CPB2** and **CPN2**, a background was recorded in a H_2O/KCl mixture (0.1 M KCl, acting as the supporting electrolyte) and acetonitrile/tetra-*n*-butylammonium hexafluorophosphate (0.1 M $TBAPF_6$, acting as the supporting electrolyte) to find the electrochemical response of the electrode itself.

Table 3.15, and **3.16**, summarises the electrochemical data recorded in H_2O/KCl and CH_3CN/ $TBAPF_6$, for the carbon paste electrodes, respectively.

Table 3.15: Electrochemical response data for the **CPB2** and **CPN2** electrodes in H_2O/KCl.

Electrode	E_{pc1} **(mV)**	E_{pc2} **(mV)**	**ΔE (mV)**	i_{pc1} **(μA)**	i_{pc2} **(μA)**	i_{pc}/i_{pa}	**E°' (mV)**
CPB2	687	48	-	-	33	-	-
CPN2	663	495	168	352.5	333	0.94	579

Table 3.16: Electrochemical response data for the **CPB2** and **CPN2** electrodes in $CH_3CN/TBAPF_6$.

Electrode	E_{pc1} (mV)	E_{pc2} (mV)	i_{pc1} (µA)	i_{pc2} (µA)
CPB2	304	-469	-	31.3
CPN2	-	-	-	-

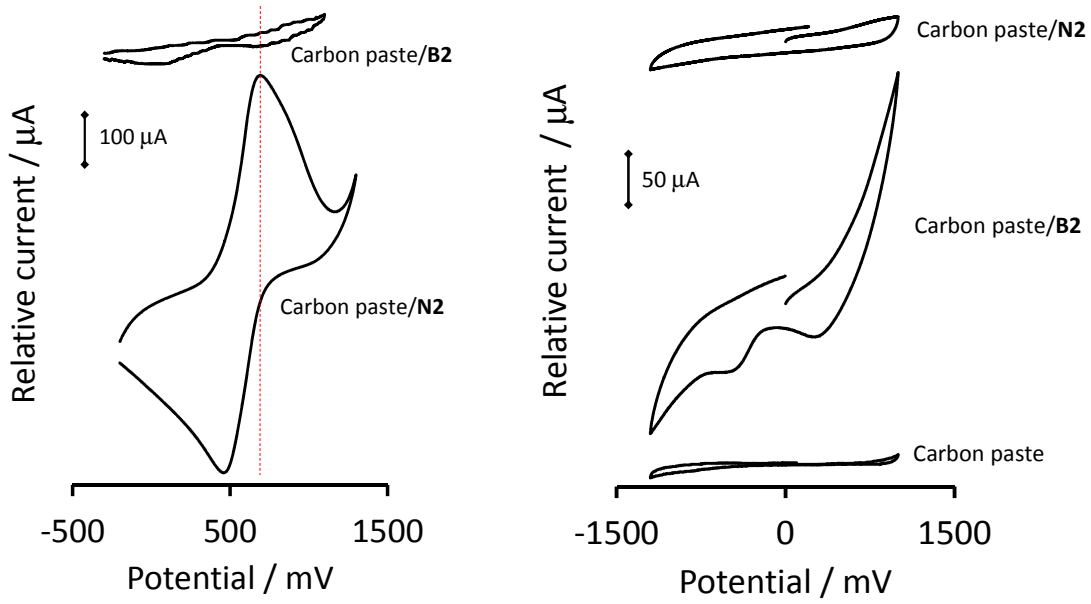

Figure 3.24: Left: Comparative cyclic voltammogram showing the background in H_2O/0.1 M KCl at 25°C and scan rate of 100 $mV.s^{-1}$ of (top) **CPB2** electrode, and (bottom) **CPN2** electrode. Right: Comparative cyclic voltammogram showing the background in acetonitrile/0.1 M $TBAPF_6$ at 25°C and scan rate of 100 $mV.s^{-1}$ of (top) **CPN2** electrode, (middle) **CPB2** electrode and (bottom) a neat carbon paste electrode.

From **Figure 3.24** it is clear that the cyclic voltammogram of the nano-sized cobalt hexacyanoferrate carbon paste modified electrode exhibited a relatively large current compared to the bulk-sized carbon paste. When the two CoHCF carbon paste modified electrodes (**CPN2** and **CPB2**) are subjected to a cyclic voltammety experiment in water/KCl, the currents (ip) of the peaks obtained are ca. 5-6 times larger than that found with glassy carbon modified electrodes, **GCB2** and **GCN2** from section **3.3.8.1**. This could be attributed to the significantly large amount of CoHCF present in the carbon paste electrode, than what was coated onto the glassy carbon electrode surface. Further, this is considered normal since the current response obtained from carbon paste electrodes are normally much larger than that normally found for a smooth surface glassy carbon electrode. It has been found that glassy carbon

modified electrodes exhibit larger resistance values than carbon paste modified electrodes. Indirectly proving that carbon paste modified electrodes exhibit larger current values than glassy carbon modified electrodes.[38] The current response observed for the bulk-sized CoHCF carbon paste modified electrodes (**CPB2**) is about ten time less than for the nano-sized CoHCF carbon paste modified electrodes (**CPN2**). This is due to much larger surface area of the nano-sized particles in the **CPN2** than in **CPB2**. The peak potentials in the **B2** modified carbon paste electrode is poorly resolved and ΔE is very large and the Fe^{II}/Fe^{III} couple is defined as being chemically and electrochemically irreversible. In contrast, the nano-sized CoHCF carbon paste modified electrodes (**CPN2**), gave well-defined peaks and the Fe^{II}/Fe^{III} couple are chemically reversible but electrochemically irreversible. The carbon paste electrodes also showed that iron was more difficult to oxidise than in the glassy cabon electrodes, for the bulk-size CoHCF by ca. 80 mV, while for the nano-size CoHCF by ca. 280 mV. This can possibly be explained by the presumption that glassy carbon electrodes have improved electroactivity due to its exposure of higher density surface oxygenated groups.[39]

When the same cyclic voltammetry experiment was performed in CH_3CN/ $TBAPF_6$, **CPN2** showed no electrochemical response while **CPB2** maintained two reduction peaks with no oxidation peaks. The electrochemical response (in CH_3CN/ $TBAPF_6$) of the **CPN2** and **CPB2** electrodes were almost the same as that found for **GCB2** and **GCN2** electrodes (from section **3.3.8.1**). **CPN2** and **GCN2** both yielded no current response on change in potential, while Epc1 and Epc2 of **CPB2** and **GCB2** differed by 2 mV and 18 mV, respectively. This similarity of the electrochemical response of **CPN2** and **CPB2** implies that electrochemical investigation of cobalt hexacyanoferrate (**B2** and/or **N2**) by either a modified glassy carbon or carbon paste electrode yielded the same data, with the exception that the carbon paste electrode offers a larger current response.

3.3.7.4 Evaluation of ferrocene oxidation on all the modified electrodes

The electrochemical behaviour of ferrocene exhibits a well-defined reversible one-electron redox process,[34, 40] which makes it a good candidate to investigate the influence of the electrode on its electrochemical response.

The electrochemical data obtained from the oxidation and reduction of ferrocene with the bulk (**GCB2**) and nano-sized (**GCN2**) CoHCF modified glassy carbon electrodes, the unmodified glassy carbon electrode and the electrodeposited CoHCF modified glassy carbon electrode (**GCED**) were recorded in **Table 3.17**. The electrochemical response of ferrocene as recorded by the unmodified glassy carbon electrode in an acetonitrile/0.1 M $TBAPF_6$ at 25°C and scan rate of 100 $mV.s^{-1}$ referenced against a

saturated Ag/AgCl electrodes, showed the expected chemical and electrochemical reversible Fe^{II}/Fe^{III} couple, with ΔE = 88 mV, $\boldsymbol{i_{pc}/i_{pa}}$ = 1 and $E^{0'}$ = 390 mV. This data will be used as a standard to compare the electrochemical response of the Fe^{II}/Fe^{III} couple measured with **GCB2** and **GCN2**.

During ferrocene oxidation, the Fe^{II}/Fe^{III} couple measured on **GCN2** and **GCED** displayed electrochemical reversibility (ΔE = 65 and 62 mV, respectively) while also being a chemical reversible redox process ($\boldsymbol{i}_{pc}/\boldsymbol{i}_{pa} \approx 0.9$). The ΔE of the two modified glassy carbon electrodes **GCN2** and **GCED** are smaller than that found for the unmodified glassy carbon electrode, which shows that the modification enhance electron transfer. The Epa of **GC** and **GCED** are within experimental error the same (434 and 440 mV), showing the modification does not affect the ease of ferrocene oxidation. However, the current response is significantly influenced and **GCN2** oxidised ferrocene at ca. 100 mV higher. The **GCED** electrode has the smallest current response when using the same concentration ferrocene at 8 mA compared to **GC** electrode which has i_{pc} of 39 mA, while **GCN2** displays the largest current response with $\boldsymbol{i}_{pa}$ = 306 mA. The **GCB2** electrode displayed a quasi-reversible electrochemical process (ΔE = 117 mV, quasi reversibility is defined as: 90 mV < ΔE > 150 mV) while displaying a chemical reversible redox process ($\boldsymbol{i}_{pc}/\boldsymbol{i}_{pa}$ = 1) for the oxidation of ferrocene. **GCN2** seems to enhance the electrochemical reversibility of ferrocene oxidation while **GCB2** diminishes the electrochemical reversibility, as can be seen from the ΔE, but the E_{pa} is the same as that found for **GC** and **GCED**. Thus depending on the electrochemical system one wishes to investigate, an electrode can be modified to suit the need for the experiment. For example, if a higher than normal current is required (when the analyte has a poor current response or when very little analyte is available), the glassy carbon electrode surface can be modified with **N2**, but the oxidation is more difficult (higher ΔE values). However, when using the **B2** modified electrode, slightly better current response and easier oxidation is achieved in comparison with the unmodified glassy carbon electrode.

Table 3.17: Electrochemical response data recorded for **GCN2**, **GCB2**, **GCED** and neat glassy carbon electrodes during ferrocene oxidation.

Electrode	E_{pa} (mV)	E_{pc} (mV)	ΔE (mV)	i_{pc} (μA)	i_{pa} (μA)	i_{pc}/i_{pa}	E°' (mV)
GCED	440	378	62	8	9	0.9	409
GCN2	535	470	65	306	325	0.94	502.5
GCB2	439	322	117	54	53.5	1	380.5
GC neat	434	346	88	43	46	0.93	390

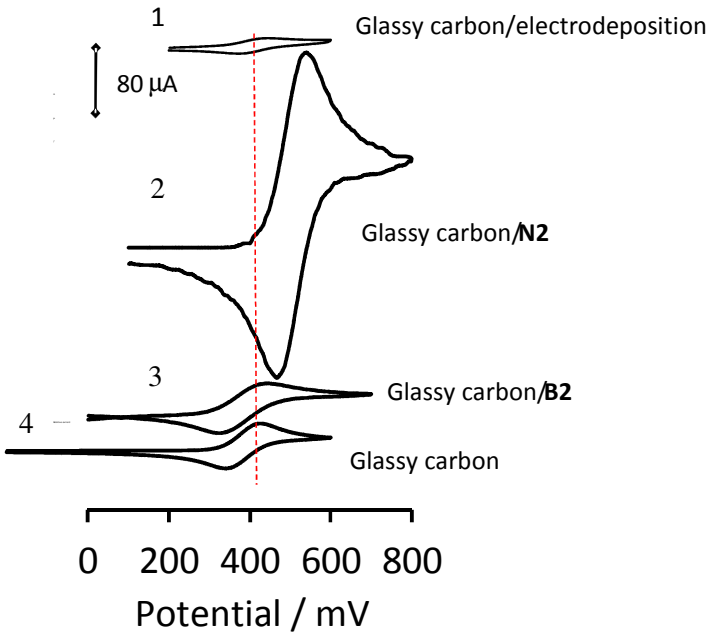

Figure 3.25: Comparative cyclic voltammograms during the oxidation of ferrocene using (1) **GCED** electrode, (2) **GCN2** electrode, (3) **GCB2** electrode and (4) a neat glassy carbon electrode.

From the electrochemical data obtained from **Figure 3.25 -** the oxidation of ferrocene with the carbon paste electrodes, **GCB2** and **CPN2**, compared to an unmodified carbon paste electrode were recorded in **Table 3.18** as measured from **Figure 3.26**. Modification of the carbon paste electrode cause the oxidation of ferrocene be achieved at lower potential in comparison to the unmodified carbon paste electrode, however the peak resolution is very poor, reversibility is impaired and additional peaks appear, thus is concluded that carbon paste electrode is not useful for investigating ferrocene's electrochemical properties.

Table 3.18: Electrochemical response data recorded for **CPN2**, **CPB2** and **CP** electrodes during ferrocene oxidation.

Electrode	**O1 (mV)**	**O2 (mV)**	**R1 (mV)**	**R2 (mV)**	**ΔE (mV)**	**i_{pc} (µA)**	**$i_{pc(2)}$ (µA)**	**i_{pa} (µA)**	**i_{pc}/i_{pa}**	**E°' (mV)**
CPN2	145	526	24	-	121	40	56	40	1	84.5
CPB2	61	-	-126	-612	187	38	37.2	40	0.95	-32.5
CP neat	572	-	500	-	72	30	-	30	1	536

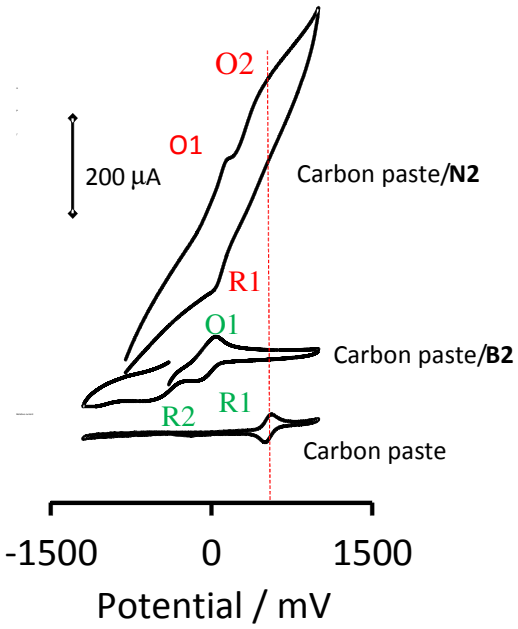

Figure 3.26: Comparative cyclic voltammograms during the oxidation of ferrocene using (top) **CPN2** electrode, (middle) **CPB2** electrode and (bottom) a neat carbon paste electrode.

3.3.7.5 Electrocatalytic oxidation of hydrazine on all the modified electrodes

The cyclic voltammetric response of the electrocatalytic oxidation of 0.1 M hydrazine with the different modified electrodes, are shown in **Figure 3.27** and the data are tabulated in Table PP.

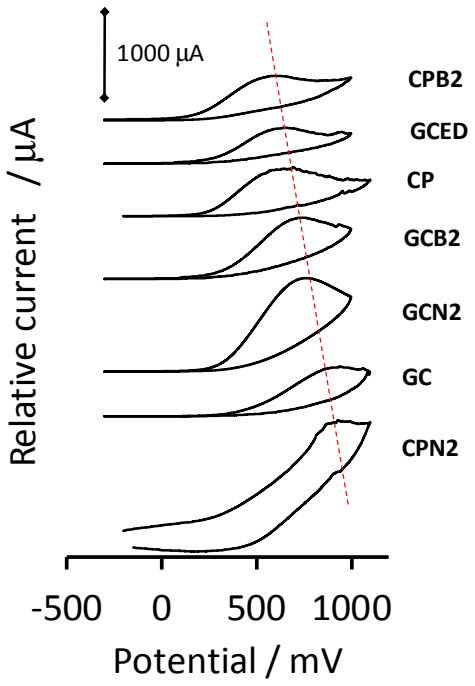

Figure 3.27: Comparative cyclic voltammograms of the electrocatalytic oxidation 0.1 M hydrazine utlitiling the modified electrodes, from the top to the bottom: bulk-sized CoHCF carbon paste (**CPB2**), electrodeposited potassium hexacyanoferrate glassy carbon electrode (**GCED**), carbon paste (**CP**), bulk-sized CoHCF modified glassy carbon electrode (**GCB2**), nano-sized CoHCF modified glassy carbon electrode (**GCN2**), glassy carbon electrode (**GC**) and nano-sized CoHCF carbon paste (**CPN2**).

The electrocatalytic oxidation of hydrazine occurs according to the following reaction:[41]

$$N_2H_4 + 4H_2O \rightarrow N_2 + 4H_3O^+ + 4e^-$$

Thus an oxidation peak is expected but no reverse reduction peak should be visible, since the reaction is irreversible. All electrodes showed very large anodic currents ranging from 378 µA (measured with **GCED**) to 924 µA (measured with **GCN2**). As can be seen from **Table 3.19**, the nano-sized modified cobalt hexacyanoferrate electrodes (both glassy carbon and carbon paste) showed the largest current response, this is due to larger surface area associated with the nano-size of the particles which gives more place for the electrocatalysis to occur causing this high current. On the other hand the bulk-size and electrodeposited cobalt hexacyanoferrate modified electrodes showed the smaller currents due to smaller surface area (for the bulk-size) available for electrocatalysis. **GCED** exhibited the smallest current which is ascribed to the very thin layer of cobalt hexacyanoferrate which electrodeposited on the surface of the glassy carbon electrode.

According to literature hydrazine is electrocatalytically oxidized at ca. 800 – 900 mV with an unmodified electrode (glassy carbon).[42] The modified electrodes oxidized the hydrazine at various potentials ranging from 562 mV (measured with **CPB2**) to 881 mV (measured with **CPN2**). In general it seems like the bulk-sized and electrodeposited cobalt hexacyanoferrate modified electrodes

electrocatalytically oxidized hydrazine at lower potentials than the nano-sized cobalt hexacyanoferrate modified electrodes. This implies that the smaller surface are (for the bulk-sized cobalt hexacyanoferrate modified electrodes) and the thin layer of cobalt hexacyanoferrate which electrodeposited on the surface of the glassy carbon electrode enhances electron transfer. Thus it seems like bulk-size cobalt hexacyanoferrate are better electron transfer mediators than the nano-size cobalt hexacyanoferrate.

Table 3.19: Anodic peak potentials of all employed electrodes during hydrazine oxidation (mV).

Electrode	**CPB2**	**GCED**	**CP neat**	**GCB2 + nafion**	**GCN2 + nafion**	**GC neat**	**CPN2**
E_{pa} (mV)	562	608	620	726	749	872	881
i_{pa} (mA)	441	378	462	630	924	504	903

3.3.8 Heterogeneous catalysis

To investigate the potential heterogeneous catalytic properties of the metal hexacyanoferrate complexes, a simple hydrogenation reaction was chosen as a model reaction. Nano-sized NiHCF (**N3**) and CoHCF (**N2**) was tested for the heterogeneous catalytic hydrogenation of 1-octene, see **Figure 3.28** for a schematic representation of the catalytic reaction.

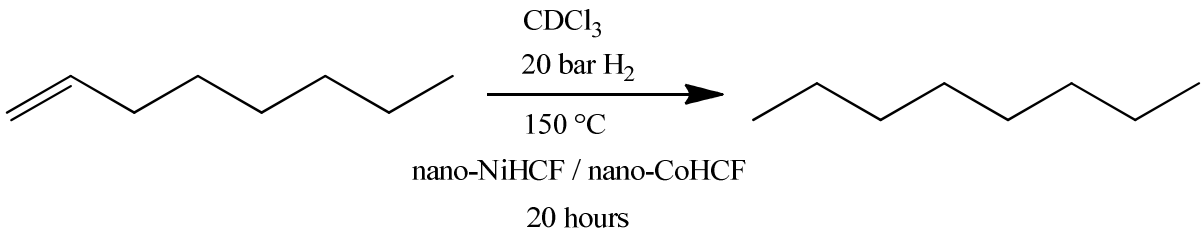

Figure 3.28. The catalytic reaction of the hydrogenation of 1-octene with either **N2** or **N3**.

From the comparison of the ^{1}H NMR of the staring material, 1-octene (see **Figure 3.29**), and the ^{1}H NMR of the crude reaction mixture (see **Figure 3.30** for the hydrogenation using **N2** as an example, **N3** is shown in the Appendix, Spectrum 35), it was clear that all the starting material was consumed during the catalytic hydrogenation of 1-octene (looking at the peaks at 5.0 and 5.8 ppm that disappear). From the resulting ^{1}H NMR's of the crude reaction mixtures it was determined that no single product was formed in isolation. Rather a mixture of different products, a few possible products that could have formed are namely the hydrogenation-, rearrangement-, double bond migration- and possible cyclisation products (see **Figure 3.31**), whose ^{1}H NMR positions corresponds with the peaks obtained from the ^{1}H NMR of the crude reaction mixtures. Since separation of organic products is outside the scope of this study, the different products was not isolated and characterised. However, the consumption of the starting material and the formation of new products does show that the metal hexacyanoferrates has the potential to act as a heterogeneous catalyst. The inclusion of the H^{1} NMR results in this dissertation were merely to indicate that the prepared material can possibly be used in an in depth organic heterogeneous catalysis study. In future studies the catalysed double bond migration, will be investigated in detail using piperylene (see **Figure 3.32** for the structure) as the starting and/or product material as well as the double bond migration in a range of alkenes.

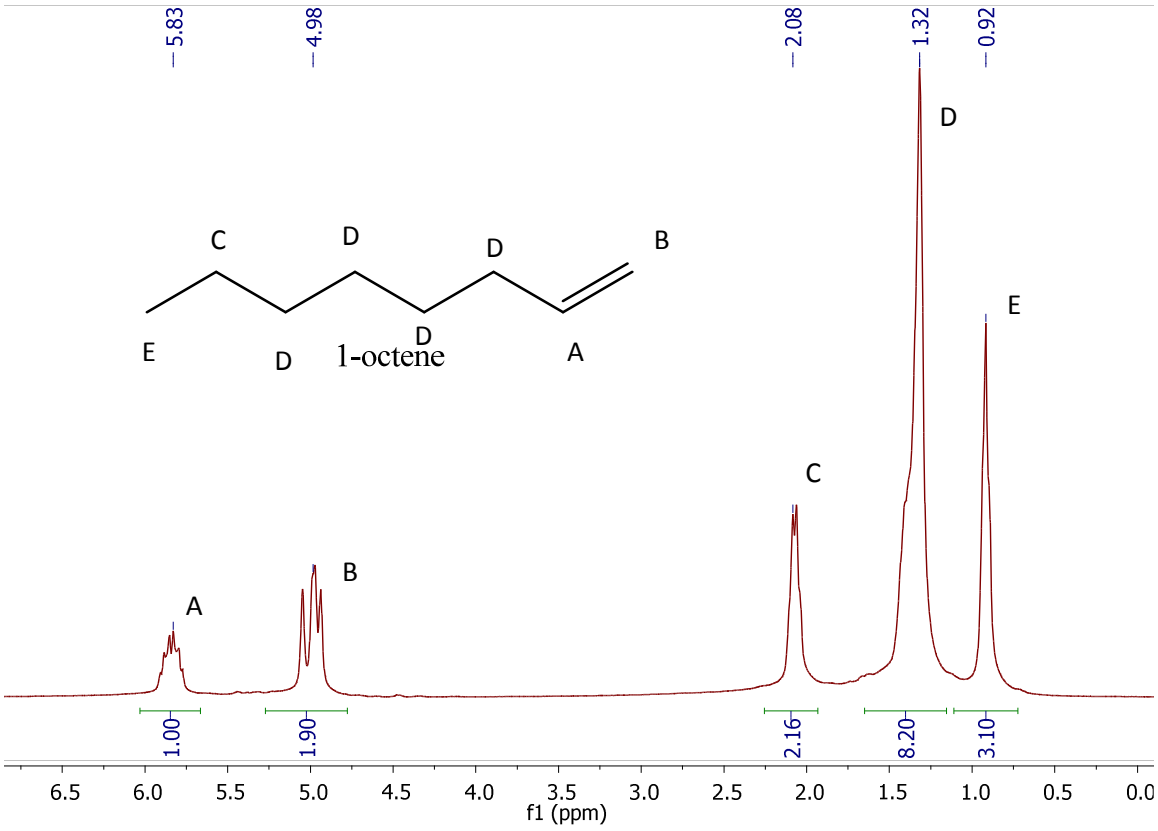

Figure 3.29: ^{1}H NMR of 1-octene as starting material generated using a Bruker Avance DPX 300 NMR spectrometer.

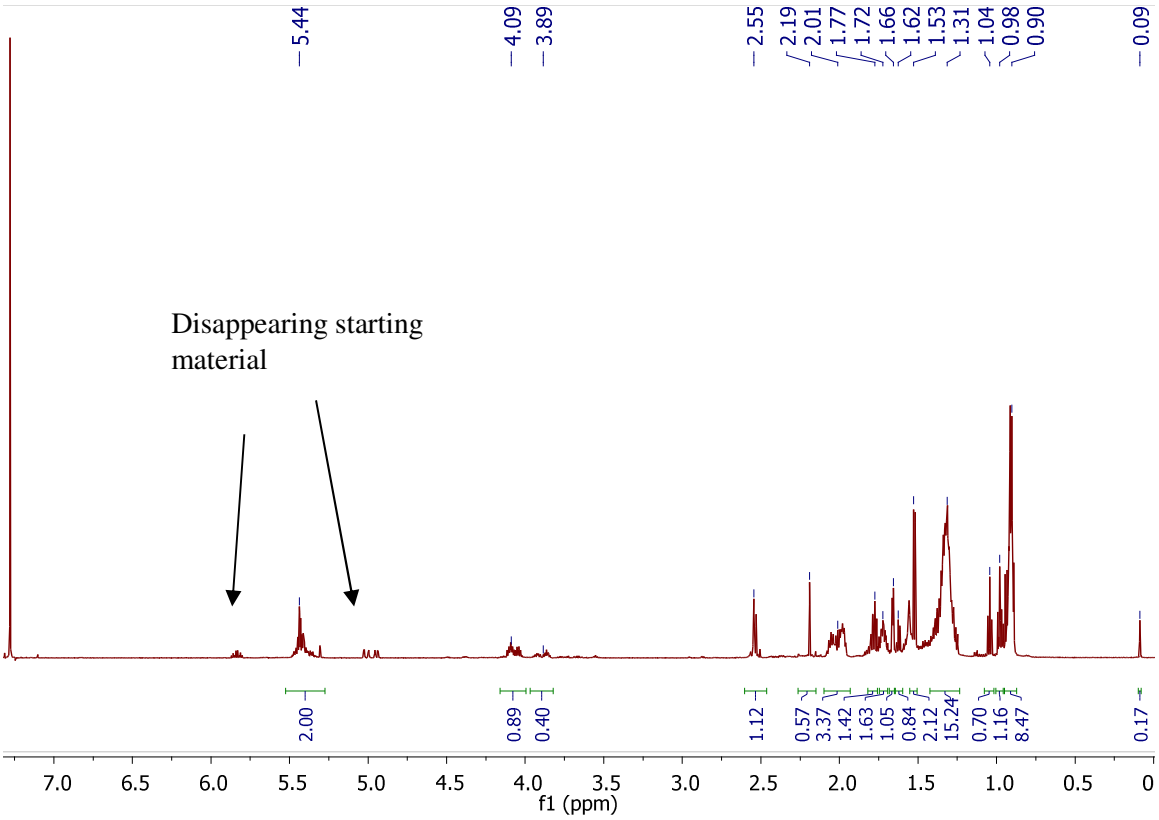

Figure 3.30: ^{1}H NMR spectrum of hydrogenation of 1-octene after 20 hours using **N2** generated using a Bruker Avance DPX 300 NMR spectrometer.

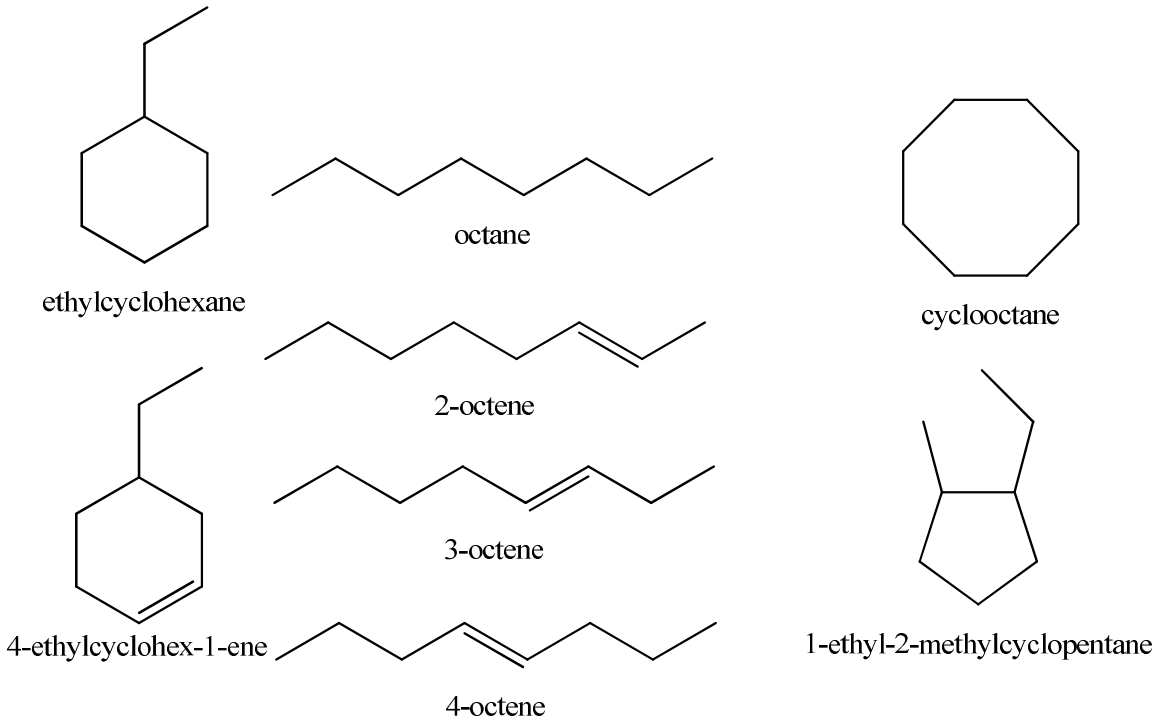

Figure 3.31: List of possible products formed from the hydrogenation of 1-octene and/or side reactions during the abovementioned hydrogenation.

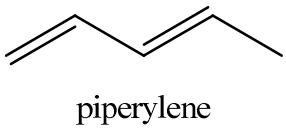

Figure 3.32: Structure of piperylene.

This concludes the discussion on the results obtained from this study as outlined by the goals set in Chapter 1. All objectives have been met. Chapter 4 gives all the experimental details that were adhered to in obtaining the researcher described in this chapter while Chapter 5 summarises all the results of this study.

References

[1] L. Pauling, *Journal of the American Chemical Society,* 1932, **54**, 3570.

[2] J. Conradie and J. C. Swarts, *Organometallics*, 2009, **28**, 1025.

[3] S. Vaucher, J. Fielden, M. Li, E. Dujardin and S. Mann, *Nano Letters*, 2002, **2**, 225.

[4] J. Eastoe, G. Fragneto, B.H. Robinson, T.F. Towey, R.K. Heenan, F.J. Leng, *Journal of the Chemical Society, Faraday Transactions,* 1992, **88**, 461-471.

[5] S. R. Ali, P. Chandra, M. Latwal, S. K. Jain, V. K. Bansal and S. P. Singh, *Chinese Journal of Catalysis,* 2011, **32**, 1844 – 1849.

[6] F. Zhao, Y. wang, X. Xu, Y. Liu, R. Song, G. Lu and Y. Li, *Applied Materials Interfaces*, 2014, **6**, 11007 – 11012.

[7] M. Berrettoni, M. Ciabocco, M. Fantauzzi, M. Giorgetti, A. Rossi and E. Caponetti, *Royal Society of Chemistry Advances*, 2015, **5**, 35435 -35445.

[8] R. R. Sheha, *Journal of Colloid and Intersurface Science*, 2012, **338**, 21-30.

[9] D. O. Ojwang, J. Grins, D. Wardecki, M. Valvo, V. Renman, L. Häggström, T. Ericsson, T. Gustafsson, A. Mahmoud, R. P. Hermann and G. Svensson, *Inorganic Chemistry*, 2016, **55**, 5928.

[10] C. W. Ng, J. Ding, Y. Shi and L. M. Gan, *Journal of Physics and Chemistry of Solids*, 2001, **62**, 769 - 770.

[11] O. Sato, Y. Einaga, A. Fujishima and K. Hasimoto, *Inorganic Chemistry*, 1999, **38**, 4405 - 4412.

[12] E. Reguera, J. Fernández-Bertrán and J. Balmaseda, *Transition Metal Chemistry*, 1999, **24**, 648 – 654.

[13] L. Xia, R.L. McCreery, *Journal of the Electrochemical Society,* 1999, **146**, 3696 - 3701.

[14] R.O. Lezna, R. Romagnoli, *The Journal of Physical Chemistry B,* 2002, **106**, 3612 - 3621.

[15] S. Chen, *Electrochimica Acta*, 1998, **43(21-22)**, 3364.

[16] J. W. Niemantsverdriet, *Spectroscopy in Catalysis*, WILEY-VCH Verlag GmbH & Co. KGaA, Weinheim, 3rd edition, 2007 ch. 3, pp. 50 - 51.

[17] B. E. Buitendach, E. Erasmus, J. W. Niemantsverdriet and J. C. Swarts, *Molecules*, 2016, **21**, 1427.

[18] N.G. Vannerberg, *Chemica Scripta,* 1976, **9**, 122.

[19] K. B. Yatsimirskii, V. V. Nemoshalenko, Y. P. Nazarenko, V. G. Aleshin, V. V. Zhilinskaya, N. A. Tomashevsky, *Journal of Electron Spectroscopy and related Phenomena,* 1977, **10**, 239.

[20] F. Moulder, W. F. Stickle, P. E. Sobol and K. D. Bomben, *Handbook of X-ray Photoelectron Spectroscopy: a reference book of standard spectra for identification and interpretation of XPS data,* ULVAC-PHI, Inc., Enzo, Chigasaki, Japan, 1995, pp. 45, 57, 143.

[21] S. Sauter, G. Wittstock and R. Szargan, *Physical Chemistry Chemical Physics*, 2001, **3**, 562 – 569.

[22] J. S. H. Q. Perera, D. C. Frost, C. A. McDowell, *The Journal of Physical Chemistry,* 1980, ***72***, 5151–5158.

[23] M. M. Kaplun, Y. E. Smirnov, V. Mikli and V. V. Malev, *Russian Journal of Electrochemistry*, 2001, **37**, 918.

[24] A. B. Mandale, S. Badrinarayanan, S. K. Date, A. P. B. Sinha, *Journal of Electron Spectroscopy and related Phenomena*, 1984, **33**, 61.

[25] T. R. I. Cataldi, R. Guascito and A. M. Salvi, *Journal of Electroanalytical Chemistry*, 1996, **417**, 89.

[26] Riyanto and M. R. Othman, *International Journal of Electrochemical Science*, 2015, **10**, 4917.

[27] H. Inoue, E. Fluck, *Z. Naturforsch.*, 1984, **39b**, 185.

[28] B. Folkesson, R. Larsson, *Journal of Electron Spectroscopy and related Phenomena*, 1982, **26**, 157.

[29] M. S. Rather, K. Majid, R. K. Wanchoo and M. L. Singla, *Journal of Thermal Analysis and Calorimetry*, 2013, **112**, 897.

[30] P. J. Kulesza, M. A. Malik, M. Berrettoni, M. Giorgetti, S. Zamponi, R. Schmidt and R. Marassi, *The Journal of Physical Chemistry B,* 1998, **102**, 1870-1876.

[31] L. Shi, T. Wu, M. Wang, D. Li, Y. Zhang and J. Li, *Chinese Journal of Chemistry*, 2005, **23**, 152.

[32] M. Berrettoni, M. Giorgetti, S. Zamponi, P. Conti, D. Ranganathan, A. Zanotto, M. L. Saladino and E. Caponetti, *The Journal of Physical Chemistry C*, 2010, **114**, 6404.

[33] M. Amelia, S. Impellizzeri, S. Monaco, I. Yildiz, S. Silvi, F. M. Raymo and A. Credi, *ChemPhysChem*, 2011, **12**, 2284.

[34] J. Conradie, T. S. Cameron, M. A. S. Aquino, G. J. Lamprecht and J. C. Swarts, *Inorganica Chimica Acta*, 2005, **358**, 2530 – 2533.

[35] G. Gritzner, *Journal of Electroanalytical Chemistry,* 1983, **144**, 260.

[36] M. Yang, J. Jiang, Y. Yang, X. Chen, G. Shen and R. Yu, *Biosensors and Bioelectronics*, 2006, **21**, 1794.

[37] A. Fitch and G. J. Edens, *Journal of Electroanalytical Chemistry,* 1989, **267**, 1.

[38] R. Antiochia, I. Lavagnini, F. Magno, F. Valentini and G. Palleschi, *Electroanalysis*, 2004, **16**, 1452 -1453.

[39] M. C. Rodriguez and G. A. Rivas, *Analytica Chimica Acta*, 2002, **459***,* 46.

[40] a) A. Hildebrandt, T. Ruffer, E. Erasmus, J. C. Swarts, and H. Lang, *Organometallics*, 2010, ***29,*** 4900.

b) V. N. Nemykin, G. T. Rohde, C. D. Barrett, R. G. Hadt, C. Bizzarri, P. Galloni, B. Floris, I. Nowik, R. H. Herber A. G. Marrani, R. Zanoni and N. M. Loim, *Journal of the American Chemical Society*, 2009, **131**, 14696.

c) A. Auger and J. C. Swarts, *Organometallics*, 2007, **26**, 102.

d) E. Erasmus, J. Conradie, A. Muller and J. C. Swarts, *Inorganica Chimica Acta*, 2007, **360**, 2277.

e) J. Conradie and J.C. Swarts, *European Journal of Inorganic Chemistry*, 2011, **13**, 2439.

f) J. Conradie and J.C. Swarts, *Dalton Transactions*, 2011, **40**, 5844.

[41] Y. Wang, Y. Wan and D. Zhang, *Electrochemistry Communications,* 2010, **12**, 187–190.

[42] A. Abbaspour and M. A. Kamyabi, *Journal of Electroanalytical Chemistry*, 2005, **576**, 77.

4 Experimental

4.1 Introduction

This section provides an in depth description of the materials, equipment, experimental procedures and techniques that were used in this study.

4.2 Materials

Solid reagents (Merck and Aldrich) for preparative purposes were used without further purification. Liquid reagents (Merck and Sigma Aldrich) were also used as received without further purification thereof. Filtration and vacuum evaporation were conducted using a water aspirator.

4.3 Spectroscopic measurements

4.3.1 Nuclear Magnetic Resonance

^{1}H NMR spectra were measured at 298 K on a Bruker Avance DPX 300 NMR spectrometer. Some specified ^{1}H NMR spectra were measured using a Bruker Avance II 600 NMR spectrometer. Chemical shifts are reported relative to $SiMe_4$ (TMS) at 0.00 ppm. The ^{1}H NMR peak for deuterated chloroform ($CDCl_3$) is at 7.28 ppm and the peak for trace amounts of water is at 1.60 ppm.

4.3.2 Attenuated Total Reflection Fourier Transformed Infrared

Attenuated Total reflection Fourier transformed infrared (ATR FTIR) spectroscopy of neat samples were performed using a Nicolet iS50 with ATR, running Omnic software (Version 9.2.86).

4.3.3 Thermogravimetric Analysis

Thermogravimetric analyses (TGA) were performed under an Argon environment on a Mettler Toledo TGA/SDTA851 and analysed with STAR SW v8.10 software.

4.3.4 X-ray Photoelectron Spectroscopy

X-ray photoelectron spectroscopy (XPS) measurements were recorded on a PHI 5000 Versaprobe system with a monochromatic A1K alpha X-ray source. Spectra were obtained using the aluminium anode (A1 Kα = 1486.6 eV) operating at 50 µm, 12.5 W and 15 kV energy (97 X-ray beam). A low energy neutraliser electron gun was used to minimise the charging of the samples the survey scans were recorded at constant pass energy of 187.85 eV and region scans at constant pass energy of 29.35 eV with the analyser resolution ≤ 0.5 eV. The background pressure was 2 x 10^{-8} mbar. The XPS data were analysed utilising Multipak version 8.2c software using Gaussian-Lorentz.; Gaussian/Lorentz ratios were always > 95%.

4.3.5 Transmission Electron Spectroscopy

Transmission electron microscopy (TEM) was performed with a Phillips (FEI) CM100 equipped with a Megaview III digital camera and coupled to an Oxford X-Max (80nm^2), energy-dispersive X-ray spectroscope (EDS). The digital images were analysed utilizing Soft Imaging System (analySIS) software. Multiple dispersions were prepared by mixing the powder with methanol and deposited on a 300-mesh nickel grid. Digital images were obtained after preparation.

4.3.6 Differential Scanning Calorimetry

Differential scanning calorimetry (DSC) measurements were performed with a Mettler Toledo DSC 822e/700. DSC data of samples were analysed with STARe SW v8.10 software. Minimal amounts (4 mg – 12 mg) of the neat sample were subjected to a temperature controlled program that was created. The program consisted of several segments. The first segment was an isothermal segment at 25 °C for 2 minutes to allow the instrument to stabilize. This was followed by a heating segment to 500 °C at a heating rate of 10 °C·min^{-1}. The heating segment was followed by a cooling segment from 500 °C to 25 °C at a cooling rate of 10 °C·min^{-1}. The heating and cooling cycles were performed three times consecutively. Constant N_2 gas flow of 3.5 ml·min^{-1}.

4.3.7 Inductive Coupled Plasma - Optical Emission Spectroscopy

ICP-OES analysis was performed with a Shimadzu ICPS-7510 Inductively Coupled Plasma – Optical emission spectroscopy with a radical-sequential plasma spectrometer for the wet chemical analysis. The vertically orientated ICP-OES with the radical viewing plasma was found to be suitable due to its better detection limits. The emission intensity measurements were made using the default conditions as indicated in (see **Table 4.1**).

Table 4.1: ICP-OES operating conditions.

Parameter	Condition
RF power	1.2 kW
Coolant gas flow rate	14.0 $L.min^{-1}$
Plasma gas flow rate	45 $L.min^{-1}$
Auxiliary gas flow rate	0.5 $L.min^{-1}$
Carrier gas flow rate	0.7 $L.min^{-1}$
Sample uptake method	Peristaltic pump
Type of spray chamber	Glass cyclonic
Type of nebulizer	Concentric
Injector tube diameter	3.0 mm

The neat samples (~0.01 g) were accurately weighed and quantitatively transferred. Sodium phosphate salts (flux) (1.0 g) were added and mixed thoroughly. The mixture was placed in an oven at 900 °C and fused for 5 minutes and left to cool to room temperature and dissolved in distilled water. These dilute solutions were analysed for C, N, Fe, Co, Ni and Cu concentrations or percentiles using ICP-OES.

4.4 Preparation of bulk sized metal hexacyanoferrate

4.4.1 Iron hexacyanoferrate

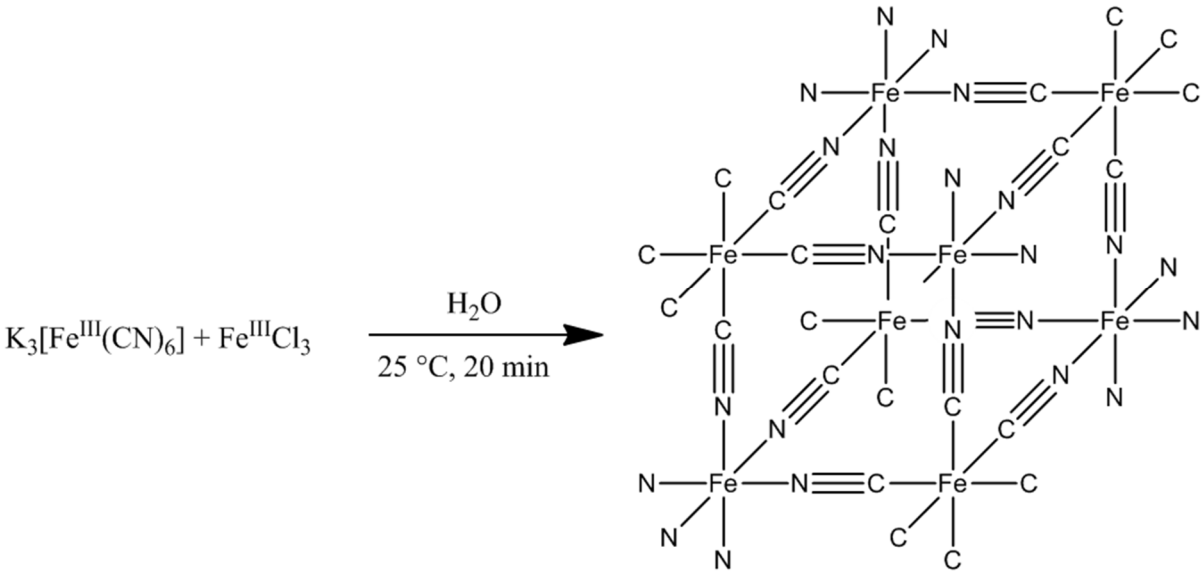

Potassium hexacyanoferrate/ferricyanide (491 mg, 1.5 mmol, 0.1 M, 1 e.q.) was dissolved in water (15.2 ml), creating an aqueous solution with a concentration of 0.1 M. To this solution was added an 15 ml aqueous solution of iron(III)chloride (0.258 g, 1.59 mmol, 0.1 M, 1.06 e.q.). The combined solution was stirred at room temperature for 15 minutes. The resulting mixture was centrifuged at 8500 rpm for 30 minutes at 15 °C. The excess water was discarded and the precipitate dried overnight *in vacuo* at 60 °C. The dried powder was crushed to yield 0.344 g (26.69 %) of pure bulk-FeHCF (**B1**).

ATR FTIR *v* (CN) = 2060 cm^{-1}.

***XPS of bulk-FeHCF* (B1):** Binding energy, eV 708.82 (Fe $_{2p3/2}$), 397.62 (N 1s).

ICP: 30 % Fe (calculated), 30.18733 % Fe (found).

Elemental analysis: 20 % C (calculated), 19.61 % C (found), 20 % N (calculated), and 20.75 % N (found).

4.4.2 Cobalt hexacyanoferrate

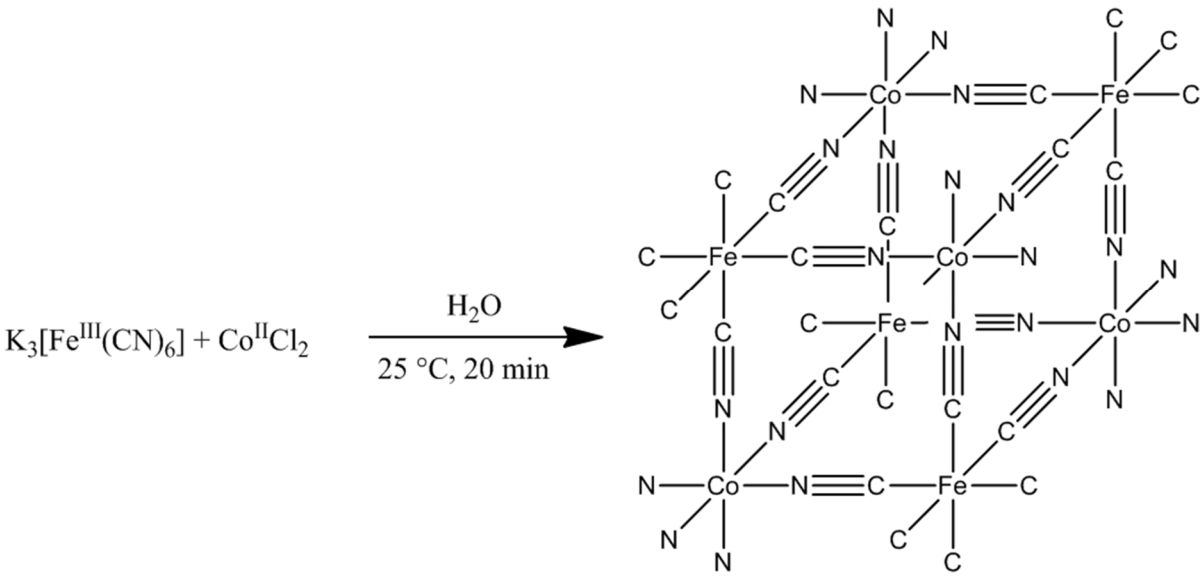

Potassium hexacyanoferrate/ferricyanide (500 mg, 1.5 mmol, 0.1 M, 1 e.q.) was dissolved in water (15.2 ml), creating an aqueous solution with a concentration of 0.1 M. To this solution was added an 15 ml aqueous solution of cobalt(II)chloride hexahydrate (0.371 g, 1.56 mmol, 0.1 M, 1.06 e.q.). The combined solution was stirred at room temperature for 15 minutes. The resulting liquid was centrifuged at 8500 rpm for 30 minutes at 15 °C. The excess water was discarded and the precipitate dried overnight *in vacuo* at 60 °C. The dried powder was crushed to yield 0.386 g (42.84 %) of pure bulk-CoHCF (**B2**).

ATR FTIR *ν* (CN) = 2107 cm^{-1}.

***XPS of bulk-CoHCF* (B2):** Binding energy, eV 709.27 (Fe $_{2p3/2}$), 397.87 (N 1s).

ICP: 15 % Fe (calculated), 14.97 % Fe (found), 15 % Co (calculated), and 20.39 % Co (found).

Elemental analysis: 20 % C (calculated), 17.07 % C (found), 20 % N (calculated), and 19.44 % N (found).

4.4.3 Nickel hexacyanoferrate

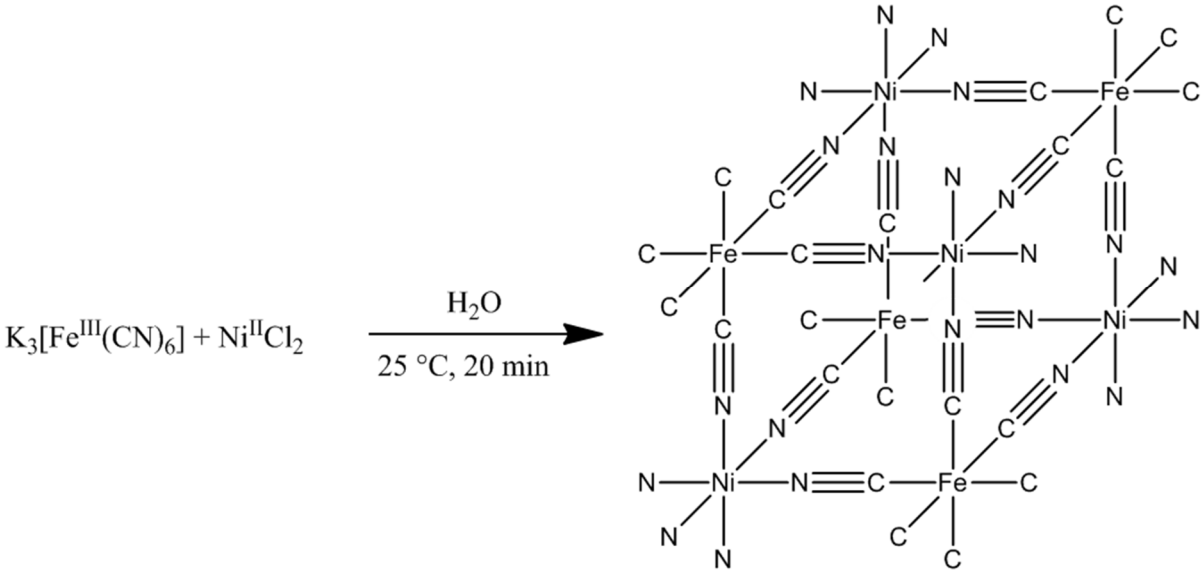

Potassium hexacyanoferrate/ferricyanide (495 mg, 1.5 mmol, 0.1 M, 1 e.q.) was dissolved in water (15.2 ml), creating an aqueous solution with a concentration of 0.1 M. Added to this solution was an aqueous solution of nickel(II)chloride (0.378 g, 1.50 mmol, 0.1 M, 1.06 e.q.) that was dissolved in water (15 mL). The combined solution was stirred at room temperature for 15 minutes. The resulting liquid was centrifuged at 8500 rpm for 30 minutes at 15 °C. The excess water was discarded and the precipitate dried overnight *in vacuo* at 60 °C. The dried powder was crushed to yield 0.382 g (94.01 %) of pure bulk-NiHCF (**B3**).

ATR FTIR *v* (CN) = 2097, 2162 cm^{-1}.

XPS of bulk-NiHCF* (B3)*: Binding energy, eV 709.42 (Fe $_{2p3/2}$), 397.66 (N 1s).

ICP: 15 % Fe (calculated), 14.97 % Fe (found), 15 % Ni (calculated), and 19.89 % Ni (found).

Elemental analysis, 20 % C (calculated), 16.29 % C (found), 20 % N (calculated), and 19.54 % N (found).

4.4.4 Copper hexacyanoferrate

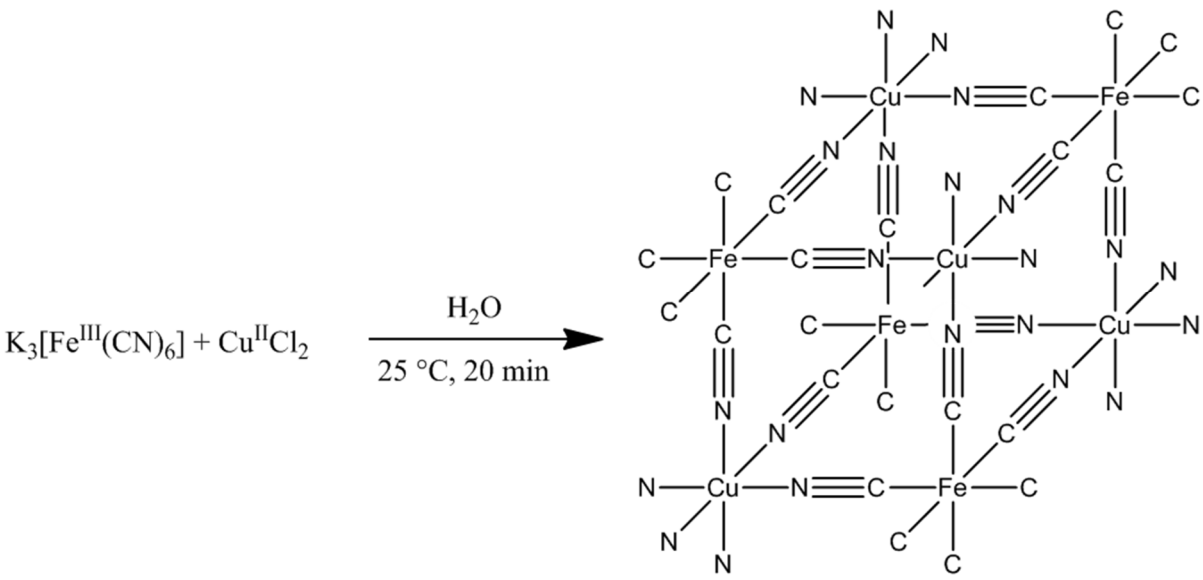

Potassium hexacyanoferrate/ferricyanide (500 mg, 1.5 mmol, 0.1 M, 1 e.q.) was dissolved in water (15.2 ml), creating an aqueous solution with a concentration of 0.1 M. Added to this solution was an aqueous solution of copper(II)chloride (0.211 g, 1.57 mmol, 0.1 M, 1.06 e.q.) that was dissolved in water (15 mL). The combined solution was stirred at room temperature for 15 minutes. The resulting liquid was centrifuged at 8500 rpm for 30 minutes at 15 °C. The excess water was discarded and the precipitate dried overnight *in vacuo* at 60 °C. The dried powder was crushed to yield 0.349 g (84.45 %) of pure bulk-CuHCF (**B4**).

ATR FTIR *ν* (CN) = 2100 cm^{-1}.

***XPS of bulk-CuHCF* (B4):** Binding energy, eV 709.28 (Fe $_{2p3/2}$), 398.45 (N 1s).

4.5 Preparation of nano sized metalhexacyanoferrate

4.5.1 Metal Aerosol-OT

In order to synthesize the nano sized metal hexacyanometallate, the surfactant material, $M(AOT)_2$, had to be prepared. M = Fe, Co, Ni or Cu. The four $M(AOT)_2$ compounds were prepared according to the same general procedure as reported by Eastoe *et. al.*

1

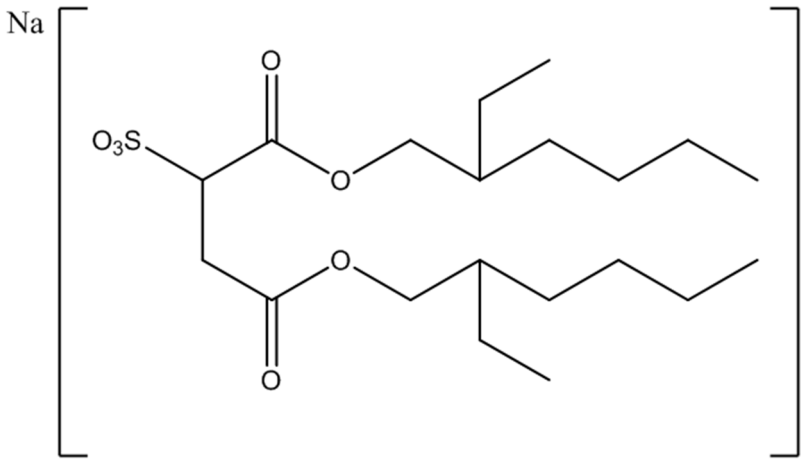

Figure 4.1: Structure of sodium Aerosol-OT (AOT).

A saturated aqueous solution (100 ml) of the relevant metal nitrate/acetate was slowly added to an ethanolic solution (150 ml, 1 M) of pure sodium-AOT (8g, $9.043x10^{-3}$ mol), while stirring. These solutions were stirred for a further *ca.* 5 min. Diethyl ether (100 ml) was added to the mixture and two phases appeared. The $M(AOT)_2$ rich organic phase was separated and washed five times with water until clear. The organic solvent was removed under reduced pressure and residual water removed *in vacuo* overnight at 60 °C.

4.5.2 Iron hexacyanoferrate

Two solutions were prepared for the synthesis. The first solution comprised of potassium hexacyanoferrate/ferricyanide (658 mg, 0.002 mol, 1 e.q.) that was dissolved in 2,2,4-trimethylpentane (10 ml) and water (10 ml) to which was added sodium-AOT (445 mg) in 2,2,4-trimethylpentane (10 ml).

The second solution consisted of $Fe(AOT)_2$ (2.3 g, 0.0026 mol, 1 e.q.) dissolved in 2,2,4-trimethylpentane (20 ml) and water (400 ml).

The first solution was added dropwise to the second solution while stirring for 15 minutes. After stirring, the solution was sonicated for 15 min with a 35% amplitude. After sonication, the solution was centrifuged for 30 min at 15 °C. The excess water was discarded while the precipitate was washed with methanol and centrifuged for 30 min at 15 °C. The methanol was discarded and the resulting precipitate dried *in vacuo* overnight at 60 °C. The resulting powder was finely crushed to yield 0.024 g (1.40 %) of pure nano-FeHCF (**N1**).

ATR FTIR *v* (CN) = 2077 cm^{-1}.

***XPS of nano-FeHCF* (N1):** Binding energy, eV 710.25 (Fe $_{2p3/2}$), 398.79 (N 1s).

4.5.3 Cobalt hexacyanoferrate

Two solutions were prepared for the synthesis. The first solution comprised of potassium hexacyanoferrate/ferricyanide (660 mg, 0.002 mol, 1 e.q.) that was dissolved in 2,2,4-trimethylpentane (10 ml) and water (10 ml) to which was added sodium-AOT (445 mg) in 2,2,4-trimethylpentane (10 ml).

The second solution consisted of $Co(AOT)_2$ (2.3 g, 0.0026 mol, 1 e.q.) dissolved in 2,2,4-trimethylpentane (20 ml) and water (400 ml).

The first solution was added dropwise to the second solution while stirring for 15 minutes. After stirring, the solution was sonicated for 15 min with a 35% amplitude. After sonication, the solution was centrifuged for 30 min at 15 °C. The excess water was discarded while the precipitate was washed with methanol and centrifuged for 30 min at 15 °C. The methanol was discarded and the resulting precipitate dried *in vacuo* overnight at 60 °C. The resulting powder was finely crushed to yield 0.672 g (55.93 %) of pure nano-CoHCF (**N2**).

ATR FTIR *v* (CN) = 2100, 2162 cm^{-1}.

***XPS of nano-CoHCF* (N2):** Binding energy, eV 709.27 (Fe $_{2p3/2}$), 397.87 (N 1s).

4.5.4 Nickel hexacyanoferrate

Two solutions were prepared for the synthesis. The first solution comprised of potassium hexacyanoferrate/ferricyanide (659 mg, 0.002 mol, 1 e.q.) that was dissolved in 2,2,4-trimethylpentane (10 ml) and water (10 ml) to which was added sodium-AOT (445 mg) in 2,2,4-trimethylpentane (10 ml).

The second solution consisted of $Ni(AOT)_2$ (2.3 g, 0.0026 mol, 1 e.q.) dissolved in 2,2,4-trimethylpentane (20 ml) and water (400 ml).

The first solution was added dropwise to the second solution while stirring for 15 minutes. After stirring, the solution was sonicated for 15 min with a 35% amplitude. After sonication, the solution was centrifuged for 30 min at 15 °C. The excess water was discarded while the precipitate was washed with methanol and centrifuged for 30 min at 15 °C. The methanol was discarded and the resulting precipitate dried *in vacuo* overnight at 60 °C. The resulting powder was finely crushed to yield 0.514 g (94.96 %) of pure nano-NiHCF (**N3**).

ATR FTIR *v* (CN) = 2165 cm^{-1}.

***XPS of nano-NiHCF* (N3):** Binding energy, eV 709.21 (Fe $_{2p3/2}$), 398.70 (N 1s).

4.5.5 Copper hexacyanoferrate

Two solutions were prepared for the synthesis. The first solution comprised of potassium hexacyanoferrate/ferricyanide (665 mg, 0.002 mol, 1 e.q.) that was dissolved in 2,2,4-trimethylpentane (10 ml) and water (10 ml) to which was added sodium-AOT (445 mg) in 2,2,4-trimethylpentane (10 ml).

The second solution consisted of $Cu(AOT)_2$ (2.3 g, 0.0026 mol, 1 e.q.) dissolved in 2,2,4-trimethylpentane (20 ml) and water (400 ml).

The first solution was added dropwise to the second solution while stirring for 15 minutes. After stirring, the solution was sonicated for 15 min with a 35% amplitude. After sonication, the solution was centrifuged for 30 min at 15 °C. The excess water was discarded while the precipitate was washed with methanol and centrifuged for 30 min at 15 °C. The methanol was discarded and the resulting precipitate dried *in vacuo* overnight at 60 °C. The resulting powder was finely crushed to yield 0.371 g (67.33 %) of pure nano-CuHCF (**N4**).

ATR FTIR *v* (CN) = 2077, 2153 cm^{-1}.

***XPS of nano-CuHCF* (N4):** Binding energy, eV 709.2 (Fe $_{2p3/2}$), 397.13 (N 1s).

4.6 Heterogeneous Catalysis Reactions

4.6.1 Hydrogenation of 1-Octene

4.6.1.1 Using Nickel Hexacyanoferrate

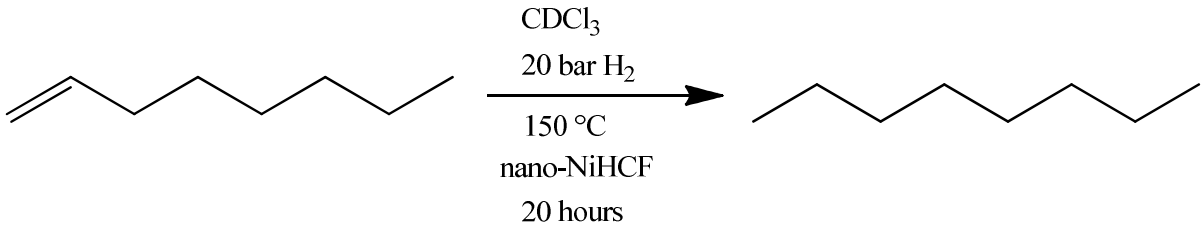

Nickel hexacyanoferrate (50 mg) was mixed with 1-Octene (0.5 mL) and deuterated chloroform (2.5 ml) in a 25 ml Parr reactor under H_2 pressure (20 bar) and heated to 150 °C. Samples of the reaction mixture were removed to record NMR at 20 hours.

4.6.1.2 Using Cobalt Hexacyanoferrate

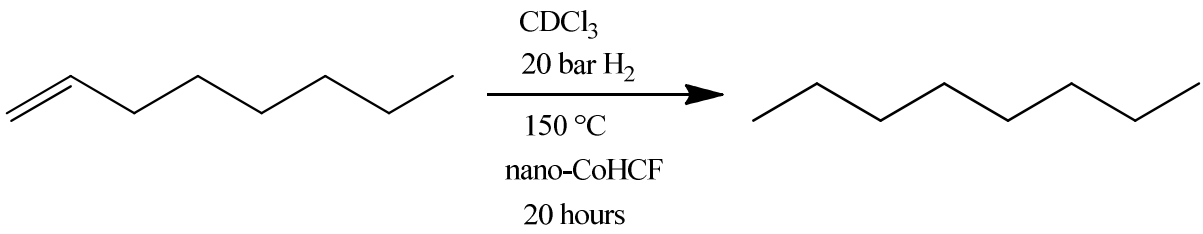

Cobalt hexacyanoferrate (50 mg) was mixed with 1-Octene (0.5 mL) and deuterated chloroform (2.5 ml) in a 25 ml Parr reactor under H_2 pressure (20 bar) and heated to 150 °C. Samples of the reaction mixture were removed to record for NMR at 20 hours.

4.7 Electrode preparation

Multiple electrodes were utilized during the course of the electrochemical studies of the cobalt hexacyanoferrates that were prepared. This section will provide insight into the different electrodes that were prepared.

4.7.1 Physical coating of a glassy carbon electrode surface with the cobalt hexacyanoferrates B2 and N2

The glassy carbon electrode was modified in two ways: The first way was by creating a physical coating of a cobalt hexacyanoferrate on the glassy carbon surface which was covered in nafion. This ensured that the sample material was firmly kept in place while still maintaining electrical conductance for the duration of the electrochemical experiments. The glassy carbon working electrode was polished to a mirror finish before each experiment. A suspension of cobalt hexacyanoferrate (**B2** and **N2**) was prepared by adding 10 mg of **B2** or **N2** to 5 ml de-ionized water and ultrasonic dispersion for 10 minutes. Then 10 µl of the suspension was pipetted onto the surface of the electrode and allowed to air dry. When completely dry, 10 µl of a 1 wt % Nafion solution was pipetted onto the modified surface.

4.7.2 Electrodeposition of cobalt hexacyanoferrate onto a glassy carbon electrode surface

The second way of modifying the glassy carbon electrode was by electrodeposition. Electrodeposition is the process where metal cations are reduced in solution simply by the addition of electrons via electric current. After the metal cations have been reduced they form a metal coating on the electrode.

A freshly cleaned glassy carbon electrode was continuously scanned (40 cycles) from -200 to 1000 mV in a 10 mM cobalt nitrate and 10 mM potassium hexacyanoferrate water/0.1 M KCl solvent system at a scan rate of 100 $mV \cdot s^{-1}$.

4.7.3 Cobalt hexacyanoferrate (B2 and N2) modified carbon paste electrodes

The cobalt hexacyanoferrates were also integrated into carbon pastes for electrochemical studies.

A mixture of 750 mg graphite, 250 mg paraffin oil and 50 mg of either **B2** or **N2** was grinded together with a mortar and pestle for 30 min. The mixture was packed tightly in a 1 ml syringe and a copper wire was added for clamping it to the electrochemical equipment. The surface of the carbon paste electrode was smoothed on Whatman paper.

4.8 Electrochemistry

4.8.1 Electrochemical characterisation in blank solutions of modified electrodes

The current increase of the modified electrodes in response to the change in potential was measured in a water solution containing 0.1M KCl as supporting electrolyte at 25°C and a scan rate of 100 $mV \cdot s^{-1}$, referenced against Ag/AgCl. The CV of the modified electrodes in acetonitrile and tetra-*n*-butylammonium hexafluorophosphate (0.1 M $TBAPF_6$) acting as the supporting electrolyte, was also measured at 25°C and a scan rate of 100 $mV \cdot s^{-1}$.

4.8.2 Evaluation of ferrocene oxidation on all the modified electrodes

The oxidation of the Fe^{II}/Fe^{III} couple of ferrocene (0.5 mM) in response to the different modified electrodes was tested in acetonitrile and 0.1 M tetra-*n*-butylammonium hexafluorophosphate (supporting electrolyte) at 25°C and a scan rate of 100 $mV \cdot s^{-1}$ referenced against Ag/AgCl.

4.8.3 Electrocatalytic oxidation of hydrazine on all the modified electrodes

The electrocatalytic oxidation of hydrazine (0.1 M) in response to the different modified electrodes was tested in water and 1 M KCl (supporting electrolyte) at 25°C and a scan rate of 100 $mV \cdot s^{-1}$ referenced against Ag/AgCl.

References

[1] J. Eastoe, G. Fragneto, B.H. Robinson, T.F. Towey, R.K. Heenan, F.J. Leng, *J. Chem. Soc. Faraday,* 1992, **88**, 461-471.

5 Conclusion and Future Prospects

5.1 Conclusion

This chapter describes in short the outputs that was achieved in fulfilment of the objectives as set out in chapter 1.

This study focused on the preparation and in-depth characterisation of metal hexacyanoferrates with a general formula of $K_xM_y[Fe(CN)_6]_z \cdot qH_2O$, with *x*, *y*, *z* and *q* representing stoichiometric numbers, which were either bulk-size (M = Fe (**B1**), Co (**B2**), Ni (**B3**) and Cu (**B4**)) or nano-size (M = Fe (**N1**), Co (**N 2**), Ni (**N 3**) and Cu (**N 4**)). Electrochemical studies were performed as well as preliminary catalytic experiments.

All prepared metal hexacyanoferrates (**B1-B4** and **N1-N4**) were characterised by multiple characterisation techniques. Spectroscopic characterisation involved, attenuated total reflection Fourier transformed infrared (ATR FTIR), X-ray photoelectron spectroscopy (XPS) and transmission electron spectroscopy (TEM). Thermal analysis of the complexes was achieved by thermogravimetric analysis (TGA), and differential scanning calorimetry (DSC), electrochemical properties was investigated by using cyclic voltammetry (CV) while inductive coupled plasma optical emission spectroscopy (ICP-OES) and elemental analyses confirmed element ratios.

A series (four) of bulk-sized metal hexacyanoferrates, **B1-B4**, were prepared by a simple co-precipitation reaction. The yields of **B1-B4** were found to be a function of the Pauling scale electronegativity, σ_M, of the metal M in $K_xM_y[Fe(CN)_6]_z \cdot qH_2O$. The order of increasing yield of the metal hexacyanoferrates were found to be **B1** (M = Fe, 26% yield, $\sigma_M = 1.83$) < **B2** (M = Co, 43% yield, $\sigma_M = 1.88$) < **B4** (M = Cu, 85% yield, $\sigma_M = 1.90$) < **B3** (M = Ni, 94% yield, $\sigma_M = 1.91$).

A series (four) of nano-sized metal hexacyanoferrates, **N1-N4**, were prepared by reverse microemulsion using an anionic surfactant, sodium bis(2-ethylhexyl)sulfosuccinate. The yields was again dependent on σ_M, with an increasing order of yield: **N1** (M = Fe, 14% yield, $\sigma_M = 1.83$) < **N2** (M = Co, 56% yield, $\sigma_M = 1.88$) < **N4** (M = Cu, 67% yield, $\sigma_M = 1.90$) < **N3** (M = Ni, 94% yield, $\sigma_M = 1.91$). Transmission electron microscopy confirmed that the size of **N2-N4** were in the nano range, with an average size between 46 and 124 nm, depending on the metal. **N1** was found not to be nano in size. It also confirmed that the compounds formed in cubic lattices that self-assembled in superlattices.

The TEM image for the nano-sized nickel hexacyanoferrate, **N3**, displayed the smallest particles, with a particle mean diameter of 46.61 nm. However, the shape of the **N3** particles are not as much cubic as they are spherical, in comparison to **N2** and **N4**, which were larger in size by about 2.5 time but displayed a cubic shape.

Multiple peaks of the cyano-group stretching frequencies, ν(C≡N), were observed in the 1900 – 2200 cm^{-1} area of the infrared spectroscopy of **B1-B4** and **N1-N4**. Each stretching frequency at the different wavenumbers represents a different possible combination of the different oxidation states e.g. Fe^{II}-C≡N-Fe^{II}, Fe^{III}-C≡N-Fe^{II}, Fe^{III}-C≡N-Fe^{III} and Fe^{II}-C≡N-Fe^{III}. Infrared spectroscopy also confirmed that the prepared metal hexacyanoferrates exhibited interstitial sites where water molecules or potassium ions could be trapped.

X-ray photoelectron spectroscopy was used to confirm the presence of each metal as well as the different oxidation states in which they occur. XPS was very useful in calculating the ratio between the metals as well as the ratio of each oxidation state of the different metals in **B1-B4** and **N2-N4**. All compounds contained Fe^{II} and Fe^{III} which show $2p_{3/1}$ photoelectron lines at ca. 708 eV for Fe^{II} and 710 eV for Fe^{III}. Secondary (satellite) peaks were also found in all compounds at a few eV higher than the main 2p photoelectron lines that were ascribed to the charge transfer that exists between the iron and the CN ligand. The XPS spectra of all non-iron metals also showed charge transfer peaks at a few eV higher than the main 2p photoelectron lines. The bulk-sized CoHCF showed a greater charge transfer ratio than the nano-sized CoHCF. The same trend was observed for the CuHCF complexes. However, in the NiHCF complexes, the nano-sized NiHCF showed a greater charge transfer ratio than the bulk-sized NiHCF. In comparison to iron there exists a smaller charge transfer ratio between ligand and non-iron metal than between ligand and iron. All the nano-sized complexes exhibited approximately the same charge transfer ratio between ligand and iron (ca. 0.33) and between ligand and M (ca. 0.16). The bulk-sized MHCF showed that in general the charge transfer ratio between ligand and metal was dependant on the Pauling electronegativity of the different metals.

The comparison of results between infrared spectroscopy and X-ray photoelectron spectroscopy gave insight into the electron distribution, charge transfer and degree of coordination within these compounds. With the assistance of previous publications it was possible to positively identify the different oxidation states of the metal atoms in most of the prepared compounds.

The elemental analyses and inductively coupled plasma optical emission spectroscopy determined the composition of each compound and assigned percentage values to the present atoms of the prepared bulk-sized metal hexacyanoferrates (**B1-B3**).

The thermal stability of all synthesized compounds was determined from the thermal gravimetric analyses of **B1-B4** and **N1-N4**. The mass loss between room temperature and ~200 °C are ascribed to the evaporation of external water molecules, while mass loss from~200 to ~300 °C are attributed to the

evaporation of intercalated (internal) water molecules. It might be necessary to thermally activate these materials before its use in catalysis studies. The mass loss associated with further heating up to 500 °C (it was only measured up to 500 °C) is assigned to the decomposition of the organic binder.

Differential scanning calorimetry was used to determine the heat flow (or structural changes) as a function of temperature for **B1-B4** and **N1-N4**. It also confirmed that external and internal water molecules were released (up to 300 °C) from the structure after which decomposition started to occur (300 °C – 500 °C).

The cobalt hexacyanoferrates (**B2** and **N2**) were used to modify the surface of glassy carbon electrodes by either physical coating them or by electrodeposition onto the glassy carbon working electrode, carbon paste modified electrodes were also prepared. The electrochemical response of the modified electrodes was tested in a blank water and acetonitrile solution. No valuable data could be obtained from the acetonitrile solvent system. However, in water/KCl, the modified glassy carbon electrodes revealed no Co^{II}/Co^{III} couples, which implies that the compounds crystallised in the insoluble form. The Fe^{II}/Fe^{III} couple for both **B2** and **N2** modified glassy carbon electrodes were found to be electrochemical irreversible with $\Delta E > 150mV$ but chemically reversible with $i_{pa}/i_{pc} \approx 1$. In general the nano-modified sample induced a larger current responses. The electrochemical behaviour in water/KCl of cobalt hexacyanoferrates-electrodeposited modified glassy carbon electrode (**GCED**), showed an electrochemically reversible ($\Delta E = 0$ mV) but chemically irreversible ($i_{pa}/i_{pc} < 1$) Fe^{II}/Fe^{III} couple. **GCED** further also showed two irreversible peaks at lower potential than the Fe^{II}/Fe^{III} couple, which was assigned to the possible reduction of the Co^{II}/Co^{III} and Co^{III}/Co^{IV} couple. As mentioned earlier, the cobalt hexacyanoferrates (**B2** and **N2**) were also used to prepare a series of carbon paste modified electrodes that were evaluated for their electrochemical properties and responses. The two CoHCF carbon paste modified electrodes (**CPN2** and **CPB2**) that were subjected to a cyclic voltammety experiment in water/KCl, produced currents (i_p) that were ca. 5-6 times larger than that found with glassy carbon modified electrodes. The electrochemical behaviour in water/KCl of cobalt hexacyanoferrate modified carbon paste electrode (**CPN2**) showed an electrochemical irreversible ($\Delta E = 168$ mV) but chemically reversible ($i_{pa}/i_{pc} \approx 0.94$) Fe^{II}/Fe^{III} couple. When the same cyclic voltammetry experiment was performed in CH_3CN/ $TBAPF_6$, **CPN2** showed no electrochemical response while **CPB2** maintained two reduction peaks with no oxidation peaks. The electrochemical response (in CH_3CN/ $TBAPF_6$) of the **CPN2** and **CPB2** electrodes were almost the same as that found for **GCB2** and **GCN2** electrodes.

The influence of the modified electrodes on the fast electron transfer compound ferrocene was also investigated. During ferrocene oxidation, the Fe^{II}/Fe^{III} couple measured on **GCN2** and **GCED** displayed electrochemical reversibility ($\Delta E = 65$ and 62 mV, respectively) while also being a chemical reversible redox process ($i_{pc}/i_{pa} \approx 0.9$). The ΔE of the two modified glassy carbon electrodes **GCN2** and **GCED**

are smaller than that found for the unmodified glassy carbon electrode, which shows that the modification enhance electron transfer. The E_{pa} of **GC** and **GCED** are within experimental error the same (434 and 440 mV), showing the modification does not affect the ease of ferrocene oxidation. However, the current response is significantly influenced and **GCN2** oxidised ferrocene at ca. 100 mV higher. The **GCED** electrode has the smallest current response when using the same concentration ferrocene at 8 mA compared to **GC** electrode which has i_{pc} of 39 mA, while **GCN2** displays the largest current response with i_{pa} = 306 mA. The **GCB2** electrode displayed a quasi-reversible electrochemical process (ΔE = 117 mV, quasi reversibility is defined as: 90 mV < ΔE > 150 mV) while displaying a chemical reversible redox process (i_{pc}/i_{pa} = 1) for the oxidation of ferrocene. **GCN2** seems to enhance the electrochemical reversibility of ferrocene oxidation while **GCB2** diminishes the electrochemical reversibility, as can be seen from the ΔE, but the E_{pa} is the same as that found for **GC** and **GCED**.

These electrodes were also tested for their electrocatalytic oxidation of hydrazine. During this oxidation, the nano-sized modified electrodes (glassy carbon and carbon paste) showed the largest current response, which was found to be due to the large surface area associated with the nano-size of the particles which gives more place for the electrocatalysis to occur. **GCED** exhibited the smallest current which is ascribed to the very thin layer of cobalt hexacyanoferrate which electrodeposited on the surface of the glassy carbon electrode. The modified electrodes oxidized the hydrazine at various potentials ranging from 562 mV (measure with **CPB2**) to 881 mV (measure with **CPN2**). In general it seems like the bulk-sized and electrodeposited cobalt hexacyanoferrate modified electrodes electrocatalytically oxidized hydrazine at lower potentials than the nano-sized cobalt hexacyanoferrate modified electrodes.

Carbon paste electrodes delivered larger current responses than the glassy carbon modified electrodes, while the glassy carbon electrodes exhibited oxidation at lower potentials than carbon paste electrodes.

The model reaction of the heterogeneous hydrogenation of 1-octene was chosen for the preliminary testing to determine the viability and practicality of metal hexacyanoferrate compounds to be used as heterogeneous catalytic material. During these preliminary catalysis experiments it was determined that more than one product formed during the hydrogenation of 1-octene. However, the solving of exactly what products formed during these reactions does not fall within the scope of this study, but this result does show that metal hexacyanoferrates has the potential to be used as heterogeneous catalysts.

5.1 Future Prospects

During the investigation of the four different metal hexacyanoferrates prepared during this study (iron-, cobalt-, nickel- and copper hexacyanoferrate) a vast amount of different results were obtained. Varying the nitrogen-coordinated metal in the metal hexacyanoferrates led to a significant change in the physical and chemical properties of the different compounds. A great quantity of knowledge may be obtained

by employing a systematic investigation of metal hexacyanoferrates or even metal hexacyanometallates where the metals are varied to include more transition, rare and even lanthanide metals. The preparation of nano size metal hexacyanometallates will be further investigated by using different surfactants and methods.

There is possible potential of these material to be used in heterogeneous catalysis. During this study preliminary catalysis were performed by hydrogenation 1-octene to indicate the viability of possible future heterogeneous catalysis studies. Amongst the possible products that formed, were rearrangement- and double bond migration products. In future studies the catalysed double bond migration, will be investigated in detail using piperylene as the starting material. When the products can be isolated and quantified properly, a full catalytic investigation (including the determination of turn over frequencies, activity, selectivity and stability of the catalyst) can be performed/carried out.

It is also an option to utilise powder diffraction for structural determination as well as the determination of structural variations at different temperatures. This would also give insight into the thermochromic behaviour that is displayed by, for instance, cobalt or copper complexes. Nano scanning Auger microscopy can be employed to identify the composition of the final products that are produced from thermal decomposition that occurs after thermal gravimetric analyses or differential scanning calorimetry is performed.

TGA spectra

Spectrum 1: **B1** Fe-CN-Fe. Temperature program: 25 °C – 500 °C. Scan rate of 10 K.min^{-1} under argon gas was applied.

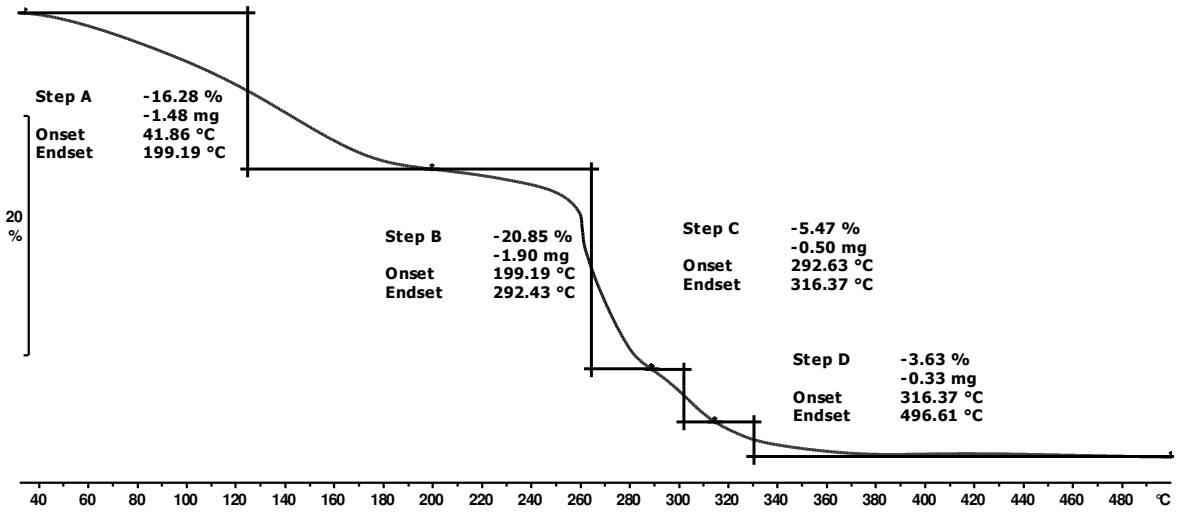

Spectrum 2: **B2** Fe-CN-Co. Temperature program: 25 °C – 500 °C. Scan rate of 10 K.min^{-1} under argon gas was applied.

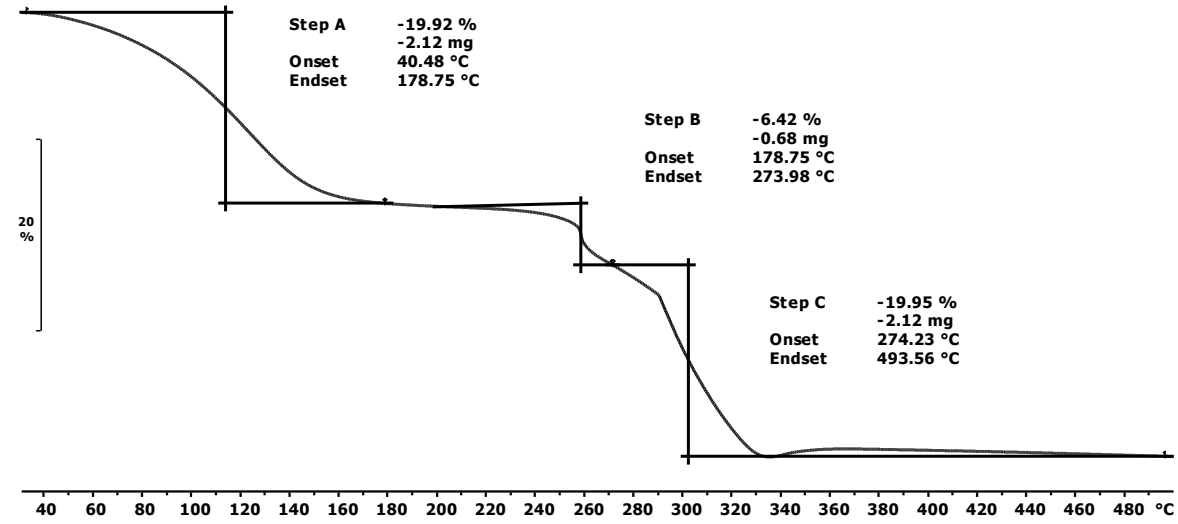

Spectrum 3: **B3** Fe-CN-Ni. Temperature program: 25 °C – 500 °C. Scan rate of 10 K.min^{-1} under argon gas was applied.

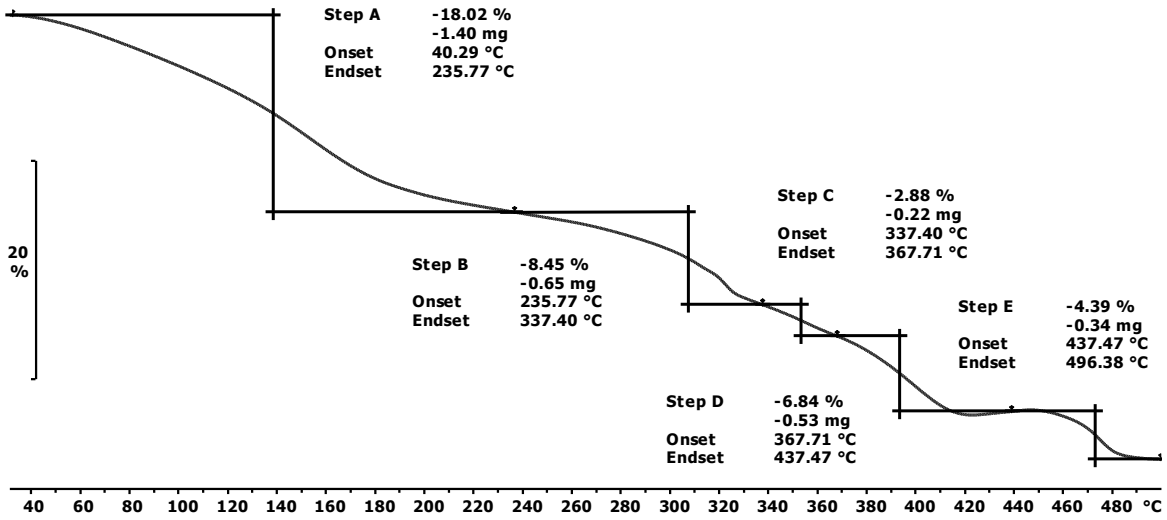

Spectrum 4: **B4** Fe-CN-Cu. Temperature program: 25 °C – 500 °C. Scan rate of 10 K.min^{-1} under argon gas was applied.

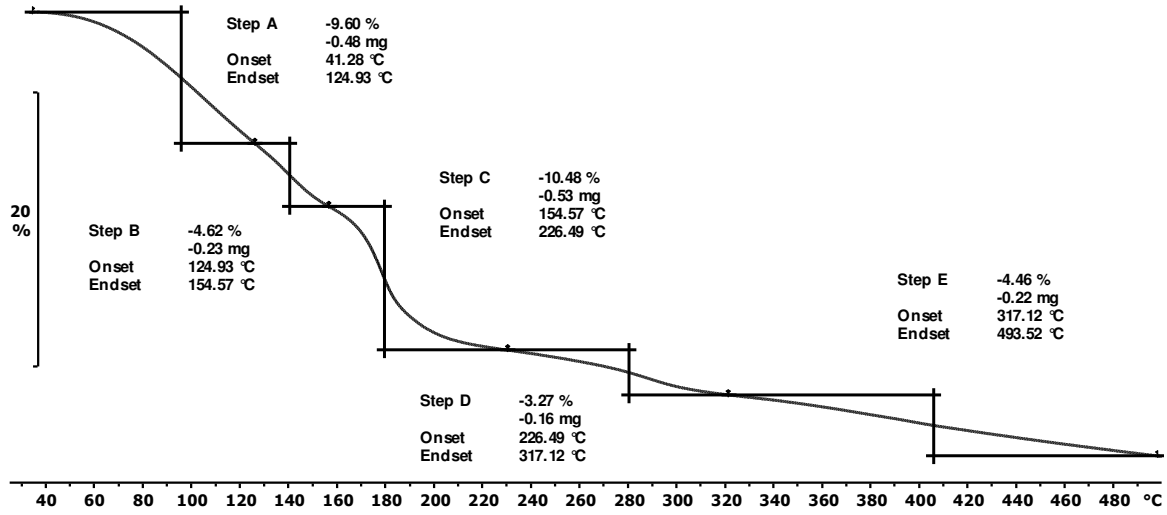

Spectrum 5: **N1** Fe-CN-Fe. Temperature program: 25 °C – 500 °C. Scan rate of 10 K.min^{-1} under argon gas was applied.

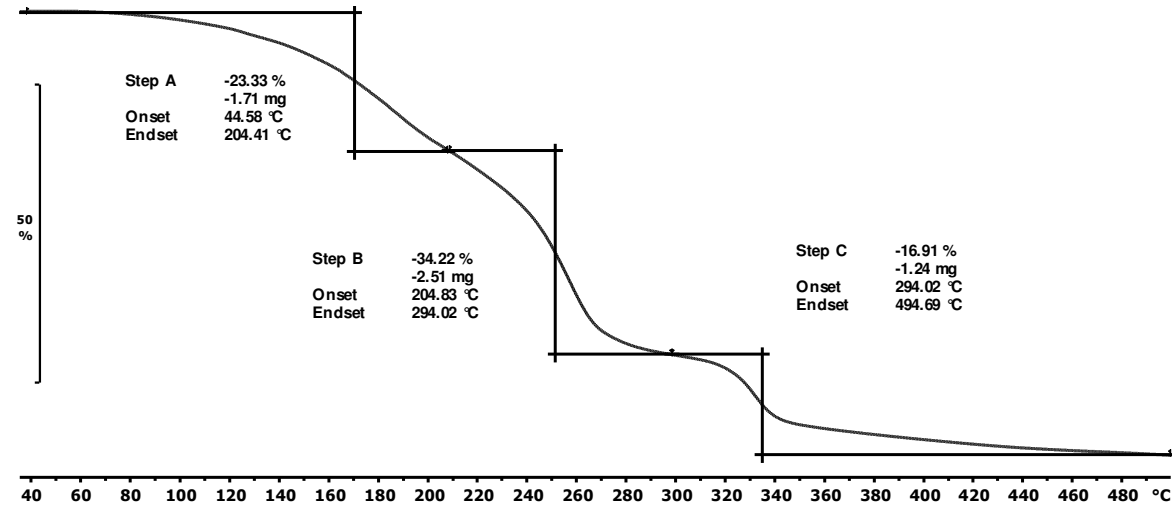

Spectrum 6: **N2** Fe-CN-Co. Temperature program: 25 °C – 500 °C. Scan rate of 10 K.min^{-1} under argon gas was applied.

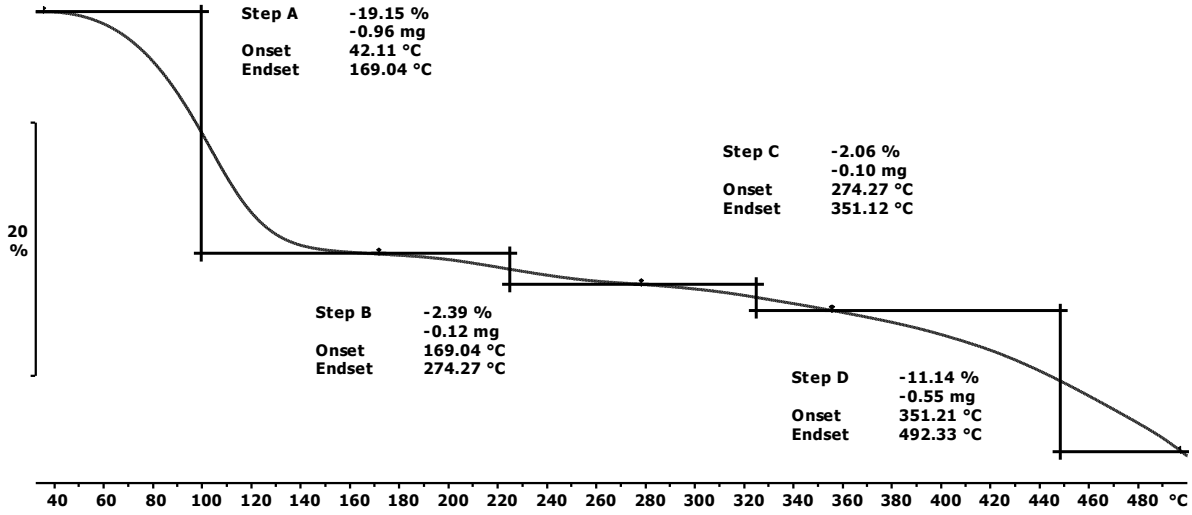

Spectrum 7: **N3** Fe-CN-Ni. Temperature program: 25 °C – 500 °C. Scan rate of 10 K.min^{-1} under argon gas was applied.

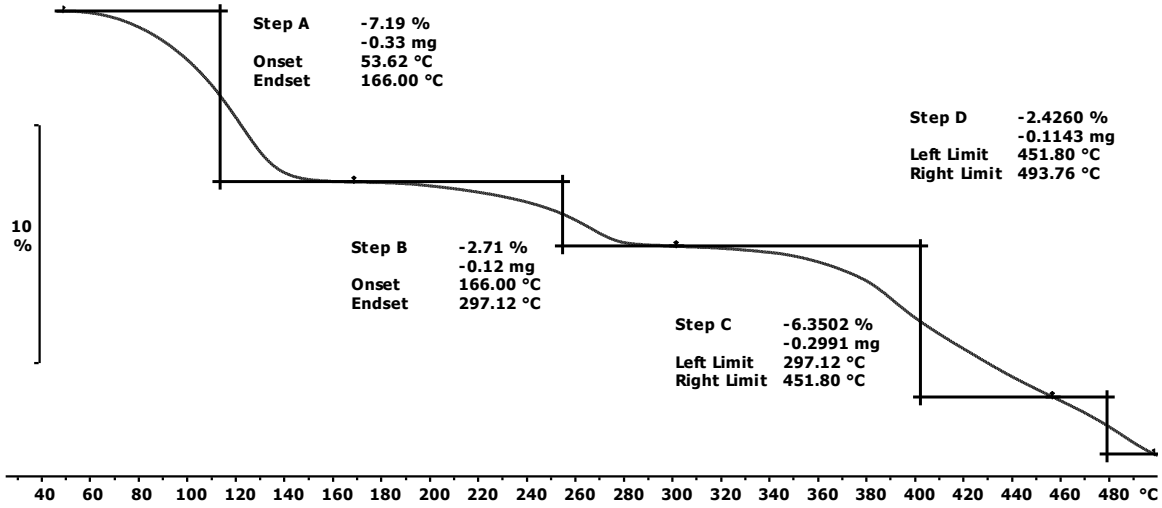

Spectrum 8: **N4** Fe-CN-Cu. Temperature program: 25 °C – 500 °C. Scan rate of 10 K.min^{-1} under argon gas was applied.

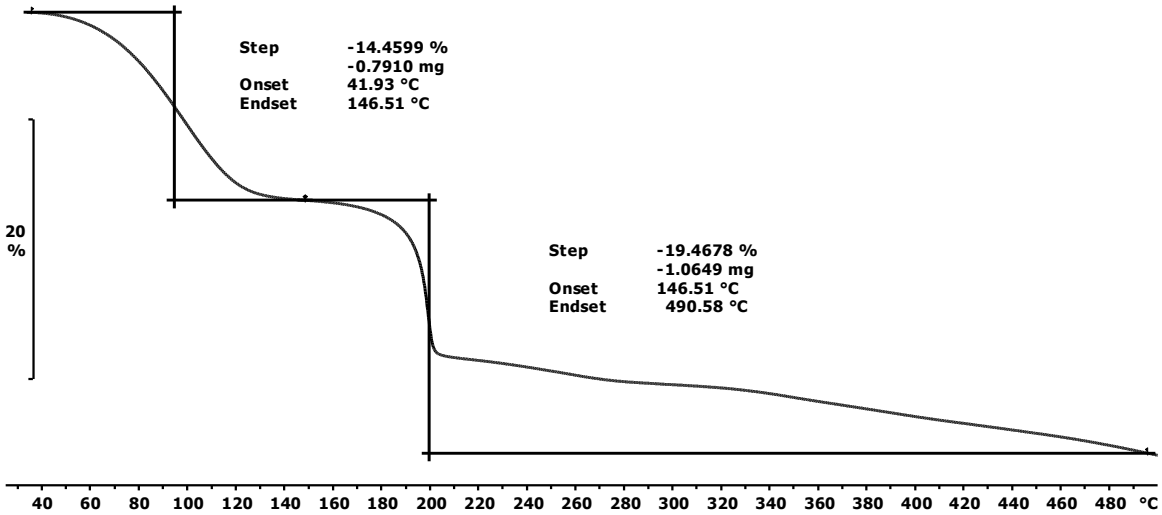

XPS spectra

Spectrum 9: XPS spectrum of bulk-FeHCF (**B1**) in the carbon region.

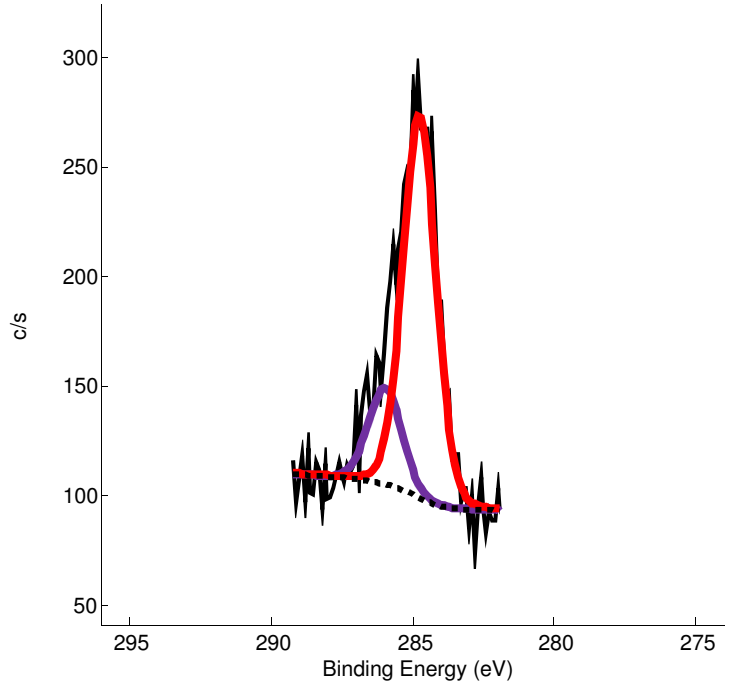

Spectrum 10: XPS spectrum of bulk-FeHCF (**B1**) in the nitrogen region.

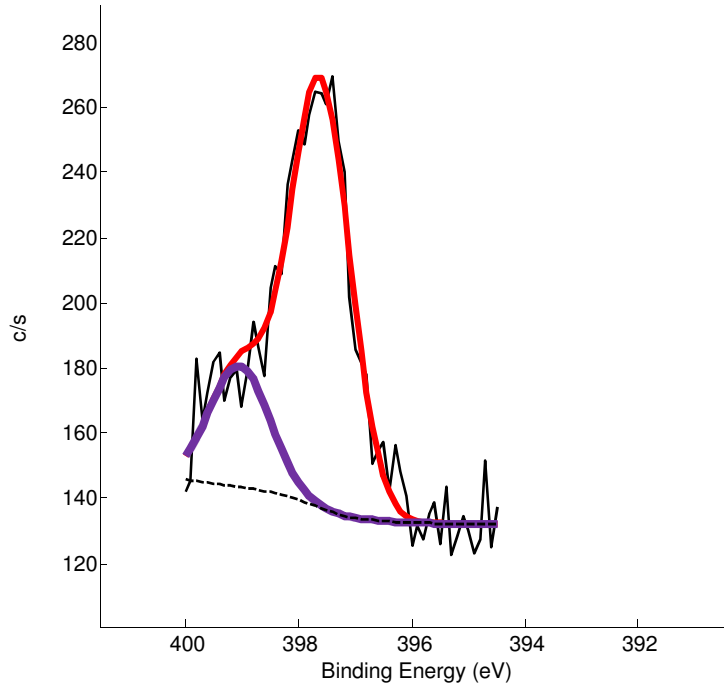

Spectrum 11: XPS spectrum of bulk-CoHCF (**B2**) in the carbon region.

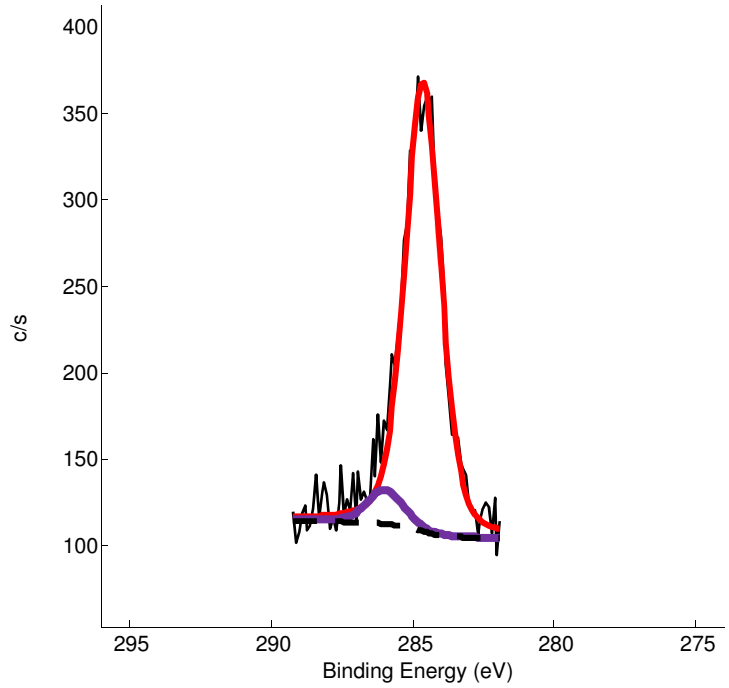

Spectrum 12: XPS spectrum of bulk-CoHCF (**B2**) in the nitrogen region.

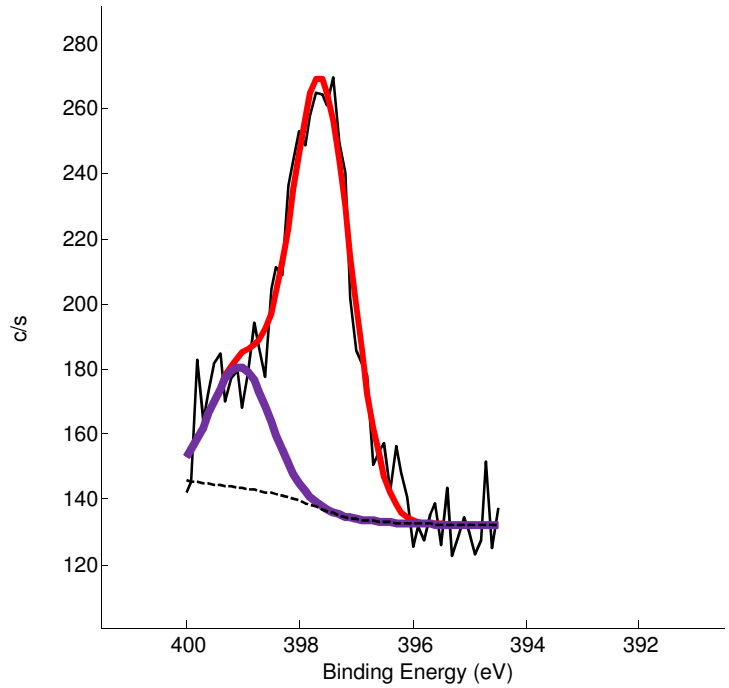

Spectrum 13: XPS spectrum of bulk-NiHCF (**B3**) in the carbon region.

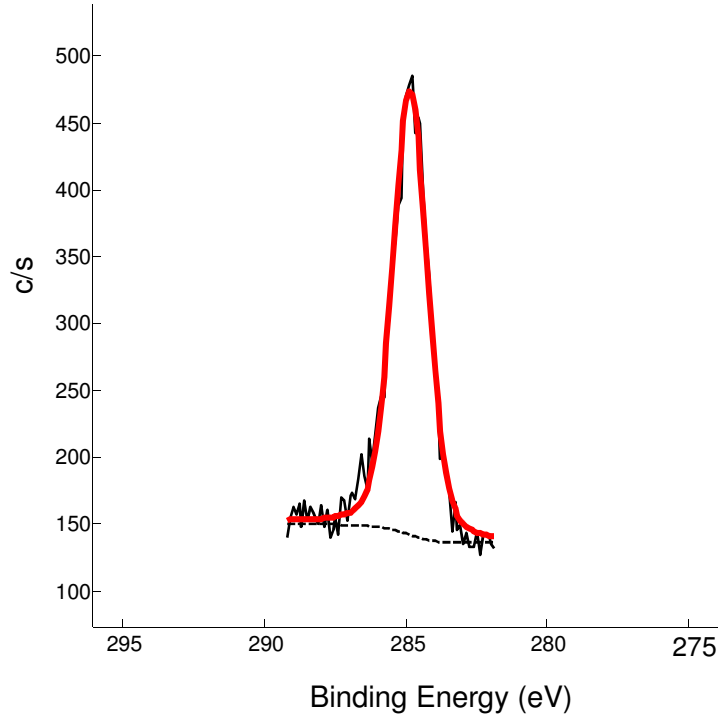

Spectrum 14: XPS spectrum of bulk-NiHCF (**B3**) in the nitrogen region.

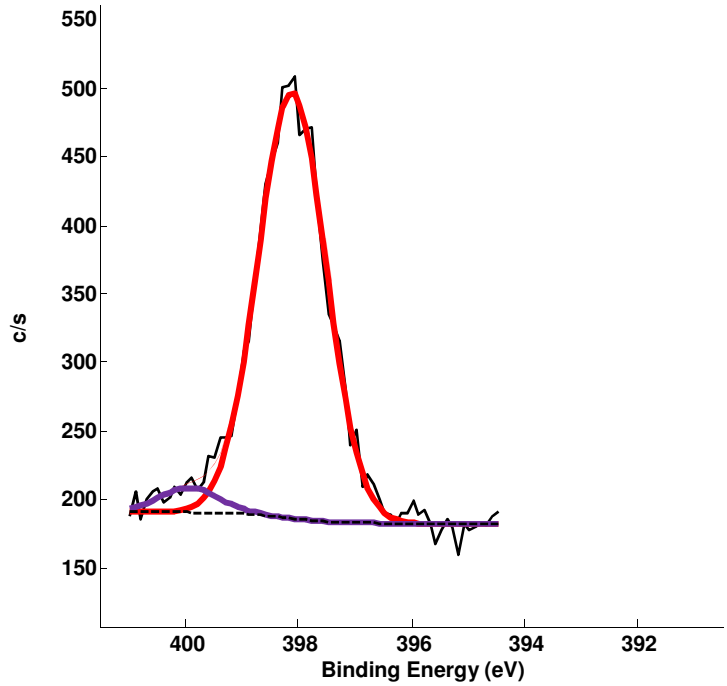

Spectrum 15: XPS spectrum of bulk-CuHCF (**B4**) in the carbon region.

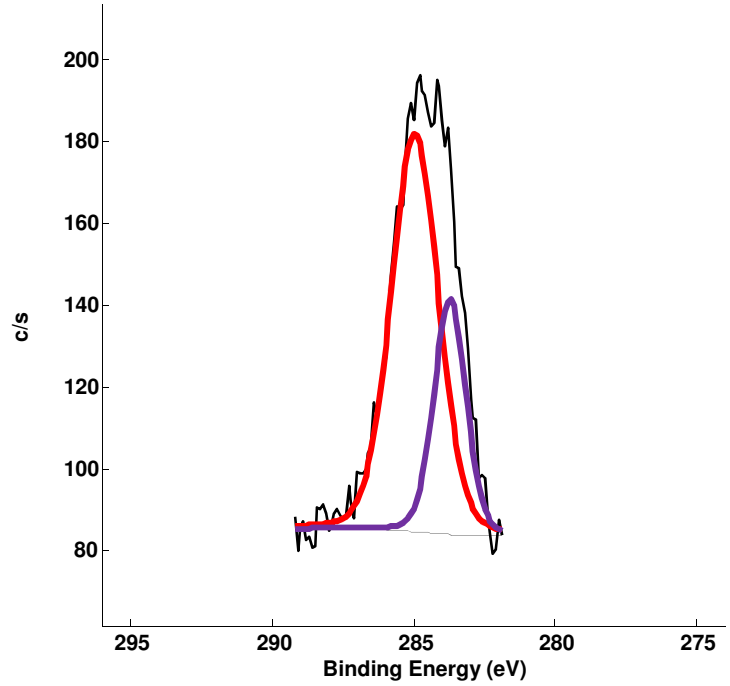

Spectrum 16: XPS spectrum of bulk-CuHCF (**B4**) in the nitrogen region.

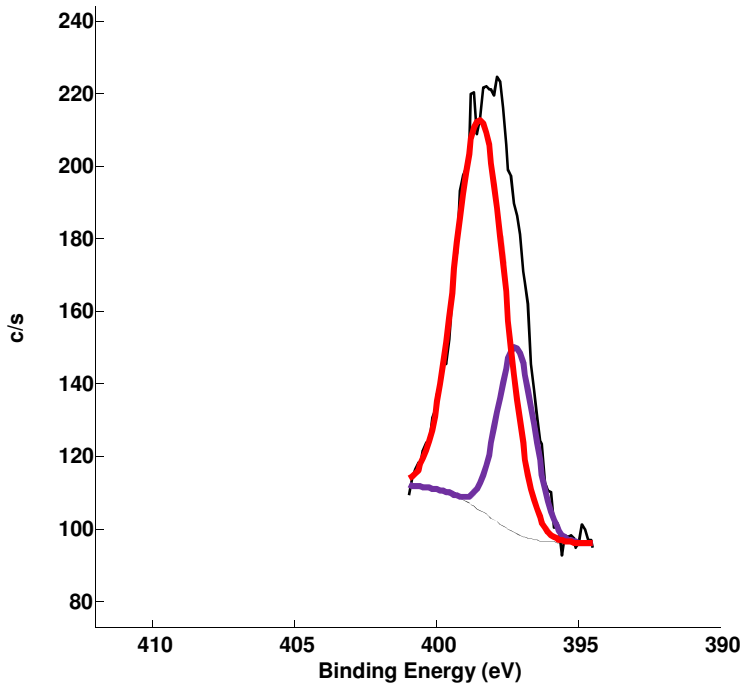

Spectrum 17: XPS spectrum of nano-FeHCF (**N1**) in the carbon region.

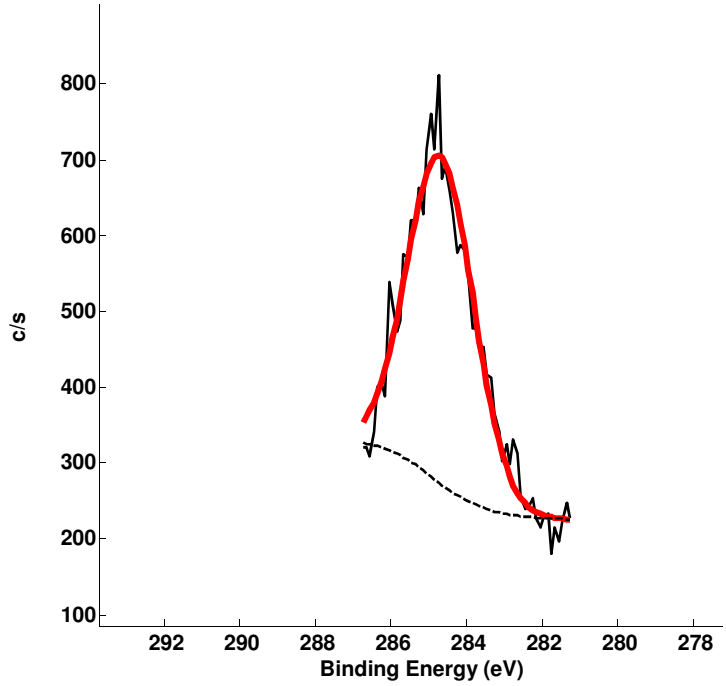

Spectrum 18: XPS spectrum of nano-FeHCF (**N1**) in the nitrogen region.

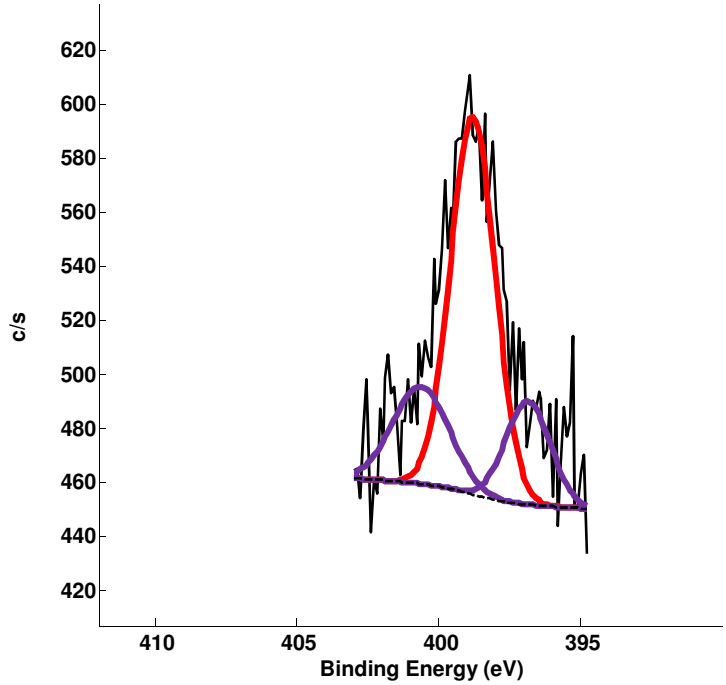

Spectrum 19: XPS spectrum of nano-CoHCF (**N2**) in the carbon region.

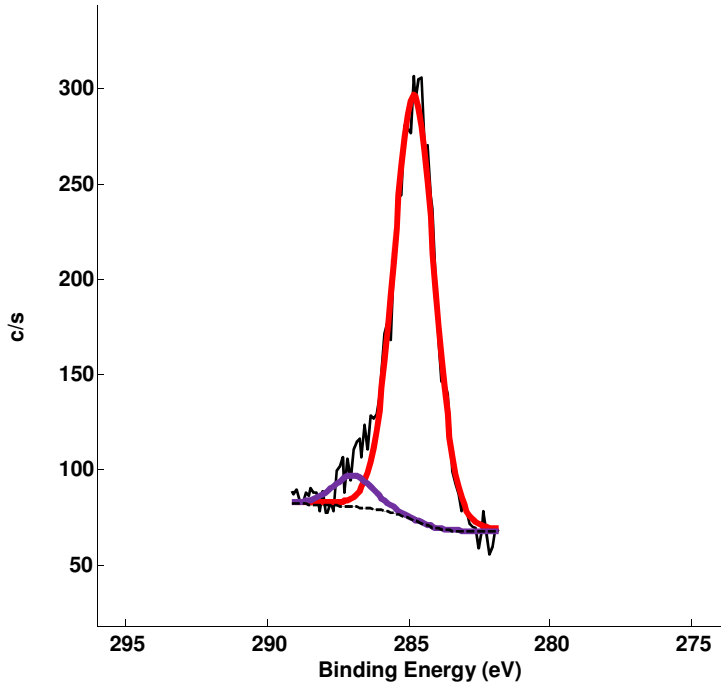

Spectrum 20: XPS spectrum of nano-CoHCF (**N2**) in the nitrogen region.

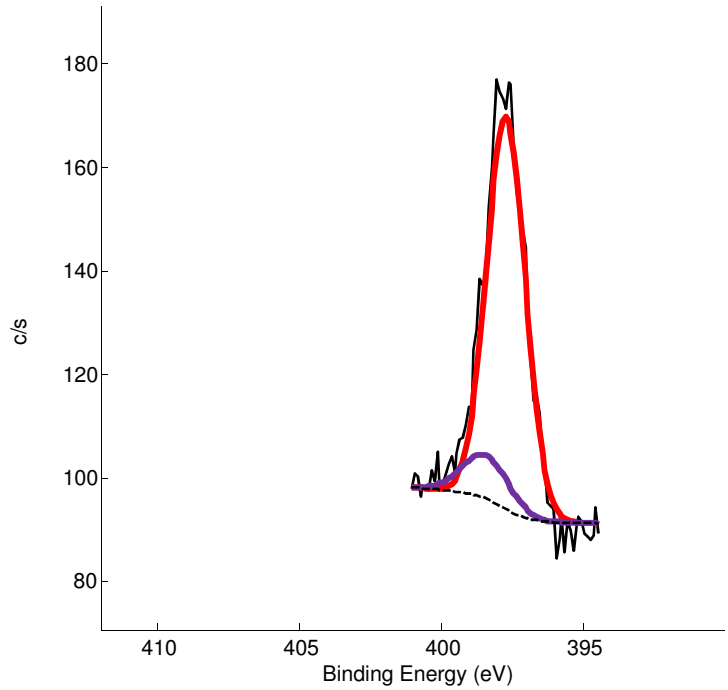

Spectrum 21: XPS spectrum of nano-NiHCF (**N3**) in the carbon region.

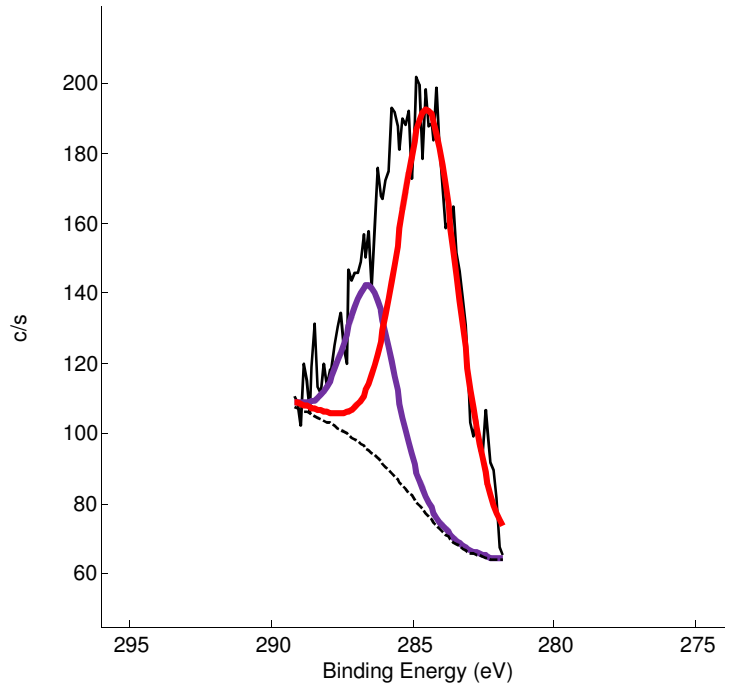

Spectrum 22: XPS spectrum of nano-NiHCF (**N3**) in the nitrogen region.

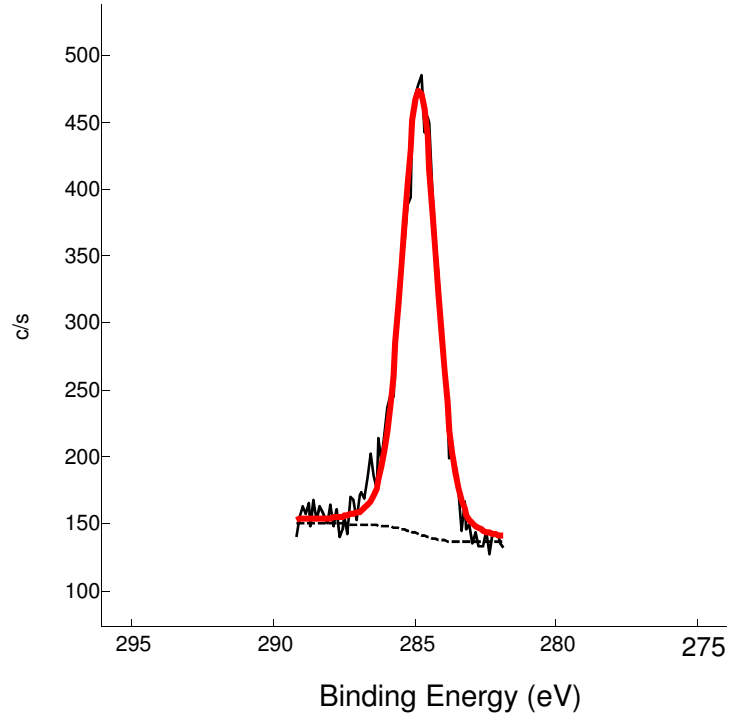

Spectrum 23: XPS spectrum of nano-CuHCF (**N4**) in the carbon region.

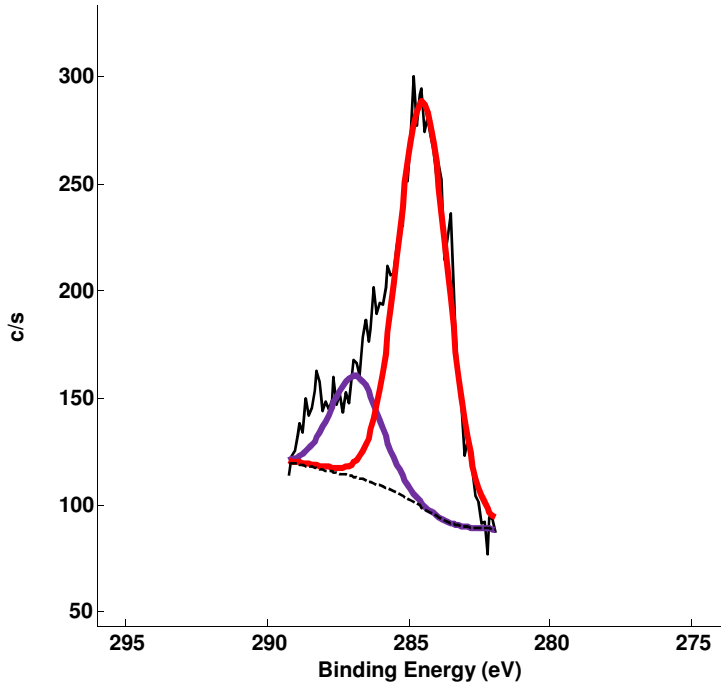

Spectrum 24: XPS spectrum of nano-CuHCF (**N4**) in the nitrogen region.

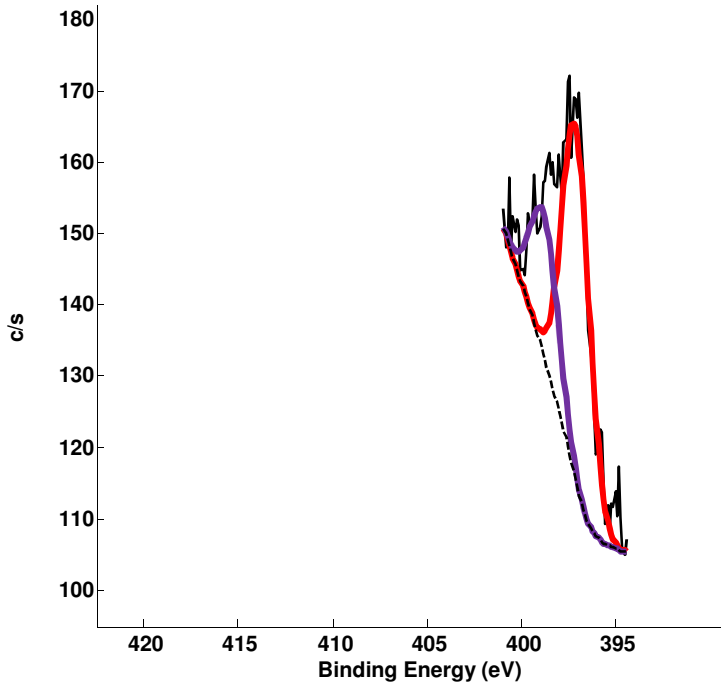

Table A1: The Binding energies of the maximum binding energy (BE) of the C 1s photoelectron lines, binding energy of the two different satellite C1s photoelectron line, as well as the peak separations between main $C1s_{main}$ and the different satellite $C1s_{shake\text{-}up}$ or $C1s_{shake\text{-}down}$, ΔBE_4 and ΔBE_5, the ratio area % between main C 1s and the different satellite $C1s_{shake\text{-}up}$ or $C1s_{shake\text{-}down}$, CHI squared values.

Complex	**No**	**Pauling σ_M**	**BE C $1s_{main}$ (eV)**	**BE C $1s_{shake\text{-}up}$ (eV)**	**BE N $1s_{shake\text{-}down}$ (eV)**	**ΔBE_4 [a] (eV)**	**ΔBE_5 [b] (eV)**	**I_{ratio} [c]**	**I_{ratio} [d]**	**CHI**
Fe-C≡N-Fe	**B1**	1.83	284.76	285.97	-	1.21	-	0.25	-	1.57
	N1		284.70	-	-	-	-	-	-	1.43
Fe-C≡N-Co	**B2**	1.88	284.64	285.97	-	1.33	-	0.08	-	1.24
	N2		284.80	286.93	-	1.42	-	0.08	-	0.71
Fe-C≡N-Ni	**B3**	1.91	284.79	286.34	-	1.55	-	0.08	-	0.86
	N3		284.80	286.22	-	1.42	-	0.08	-	2.02
Fe-C≡N-Cu	**B4**	1.90	284.98	-	283.78	-	1.24	-	0.74	1.13
	N4		284.48	286.84	-	2.36	-	0.24	-	0.99

[a] $\Delta BE_4 = BE_{C1s\ main} - BE_{C1s\ shake\text{-}up}$. [b] $\Delta BE_5 = BE_{C1s\ main} - BE_{C1s\ shake\text{-}down}$. [c] I_{ratio} = ratio between the intensities of the $C1s_{main}$ and $C1s_{shake\text{-}up}$ photoelectron lines ($I_{ratio} = (I_{C1s\ shake\text{-}up})/(I_{C1s\ main})$).[d] I_{ratio} = ratio between the intensities of the $C1s_{main}$ and $C1s_{shake\text{-}down}$ photoelectron lines ($I_{ratio} = I_{C1s\ shake\text{-}down})/(I_{C1s\ main})$).

Spectrum 25: Comparative XPS spectra of bulk- and nano-CoHCF (**B2** and **N2**) in the cobalt region.

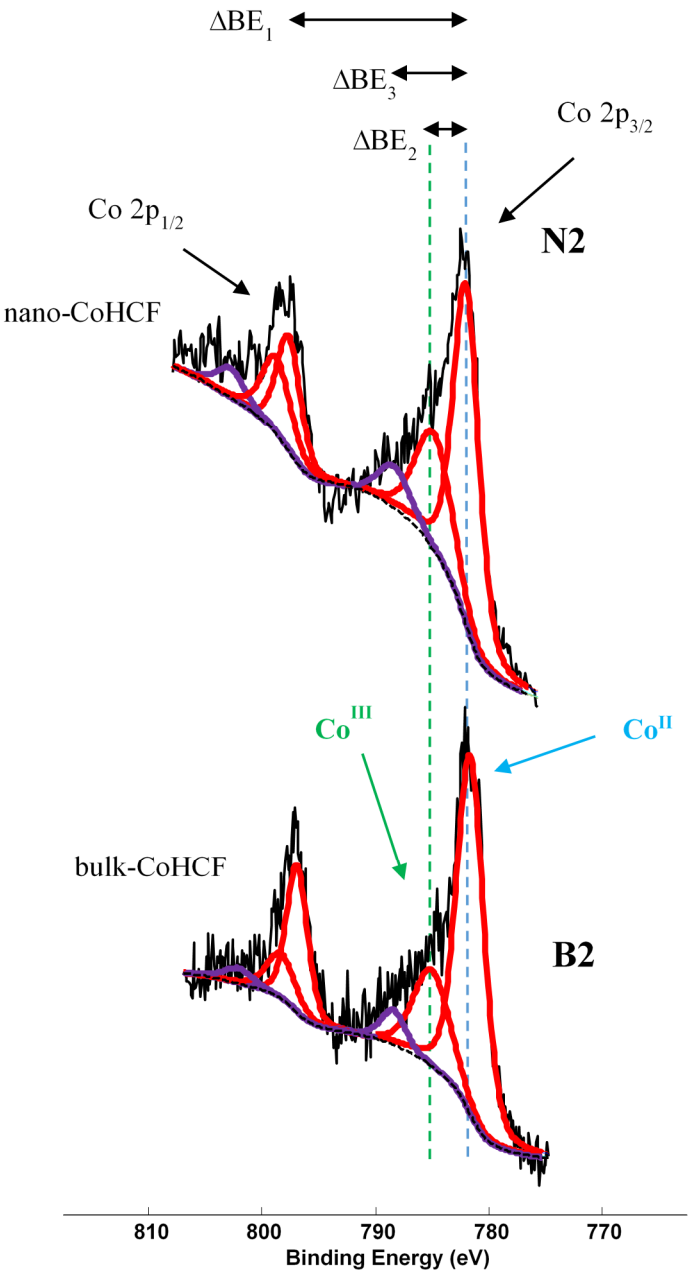

Spectrum 26: Comparative XPS spectra of bulk- and nano-NiHCF (**B3** and **N3**) in the nickel region.

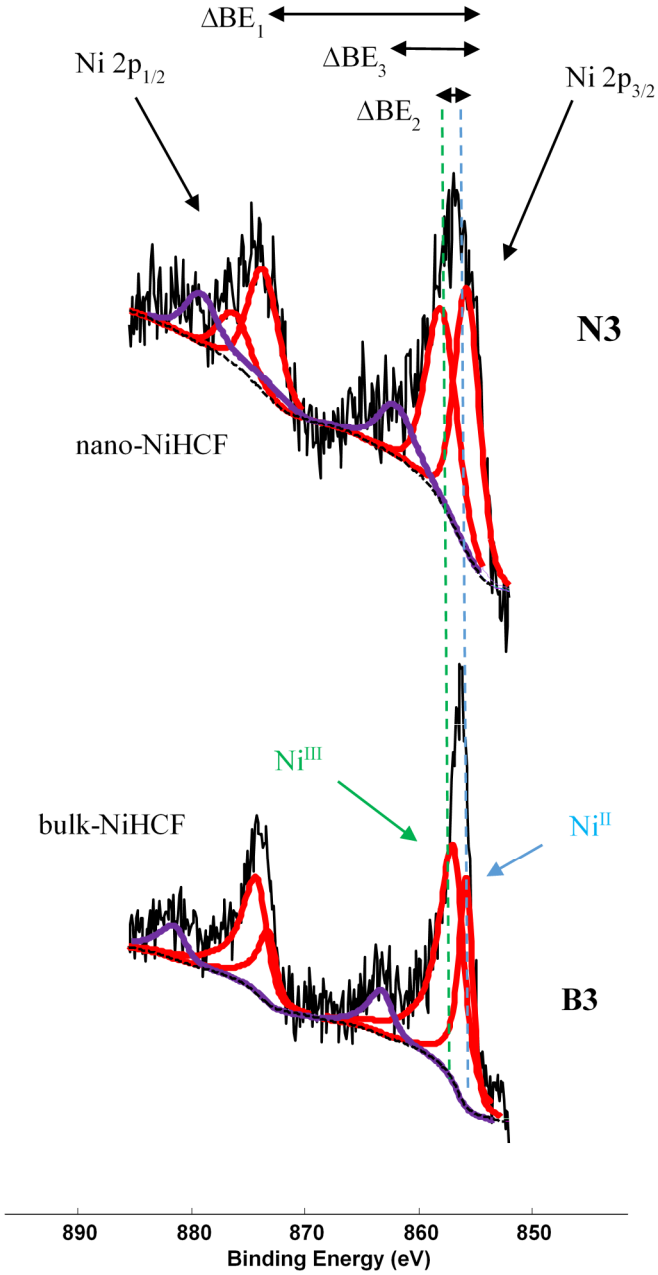

Spectrum 27: Comparative XPS spectra of bulk- and nano-CuHCF (**B4** and **N4**) in the copper region.

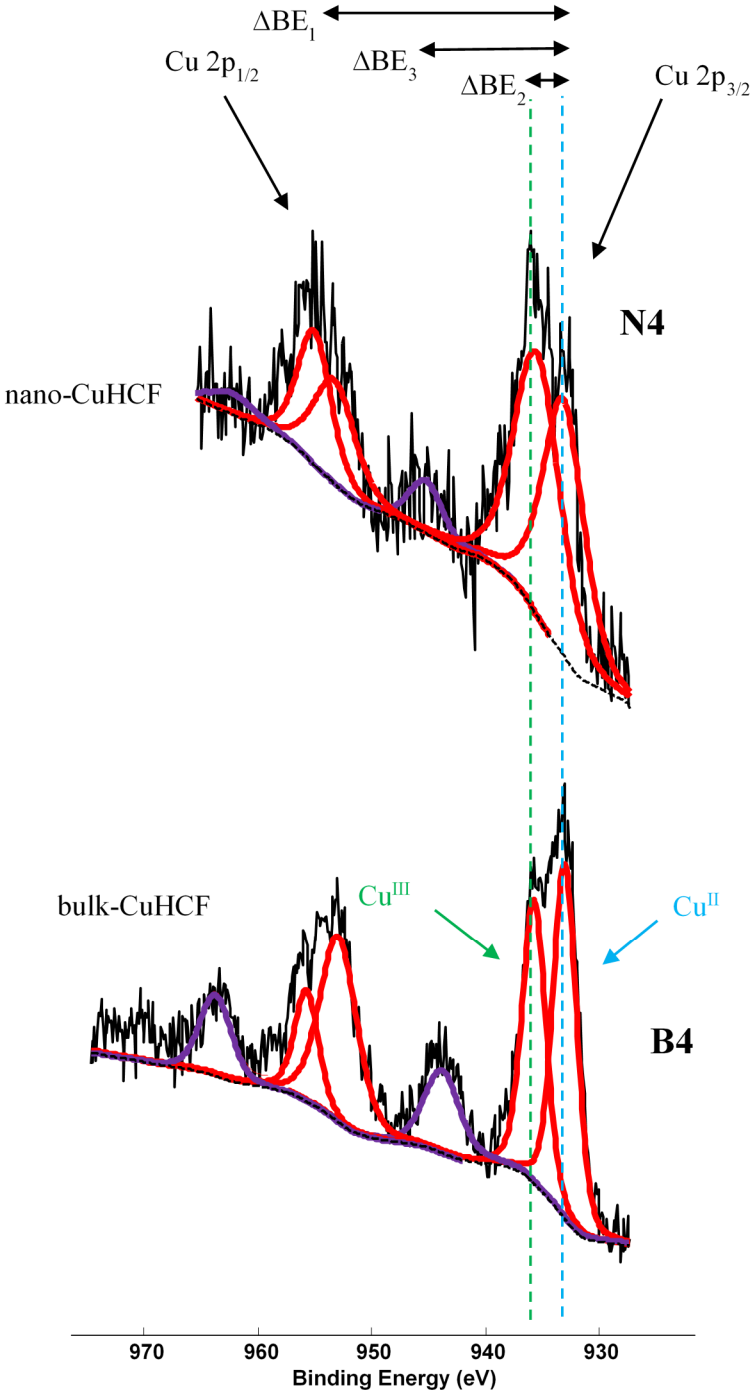

DSC spectra

Spectrum 28: Single DSC heating/cooling cycle of **B1** (bulk-FeHCF).

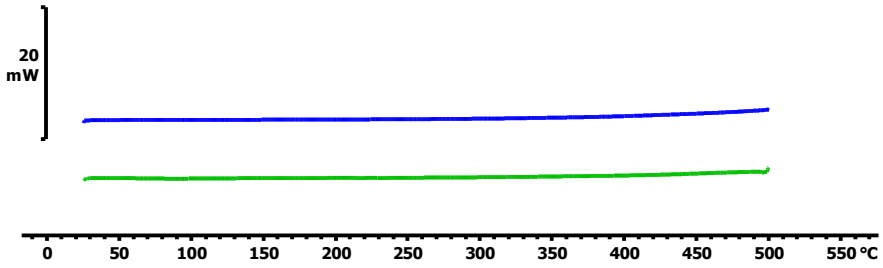

Spectrum 29: Single DSC heating/cooling cycle of **B2** (bulk-CoHCF).

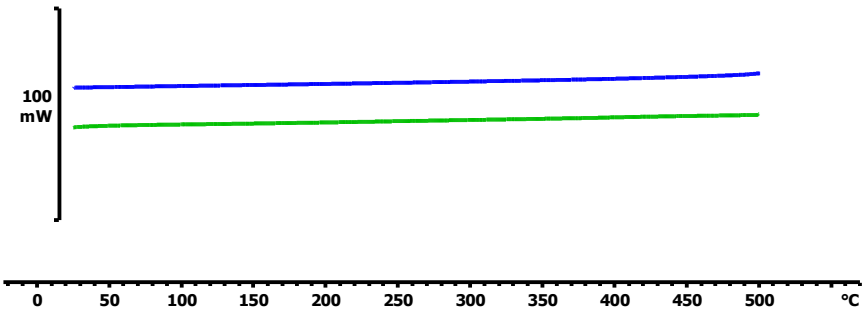

Spectrum 30: Single DSC heating/cooling cycle of **B3** (bulk-NiHCF).

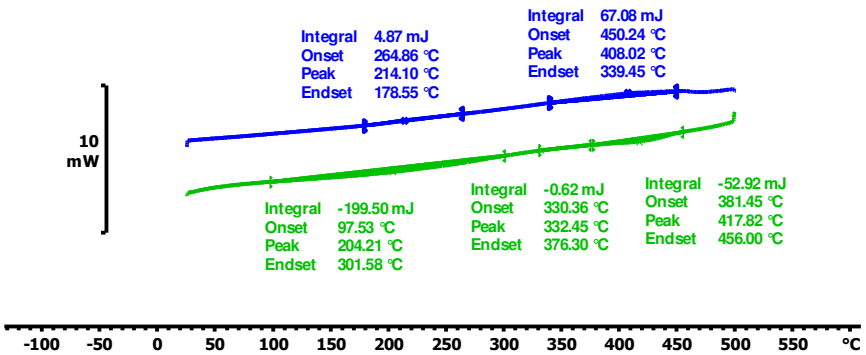

Spectrum 31: Single DSC heating/cooling cycle of **B4** (bulk-CuHCF).

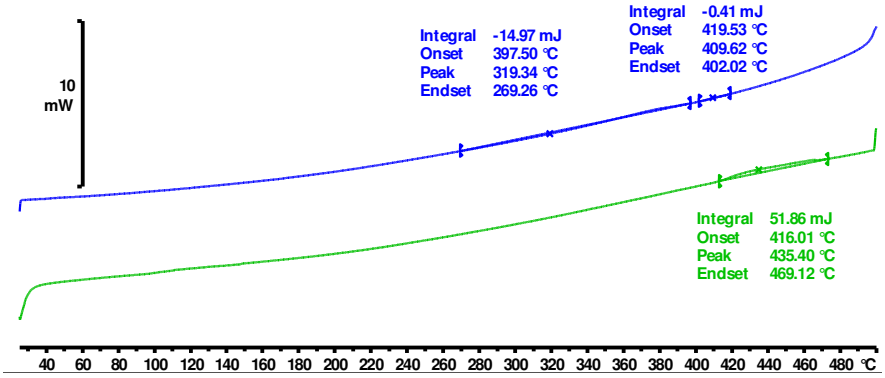

Spectrum 32: Single DSC heating/cooling cycle of **N1** (nano-FeHCF).

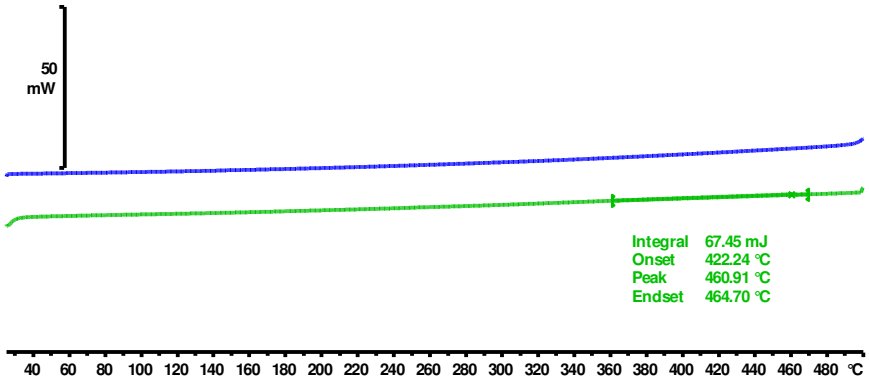

Spectrum 33: Single DSC heating/cooling cycle of **N2** (nano-CoHCF).

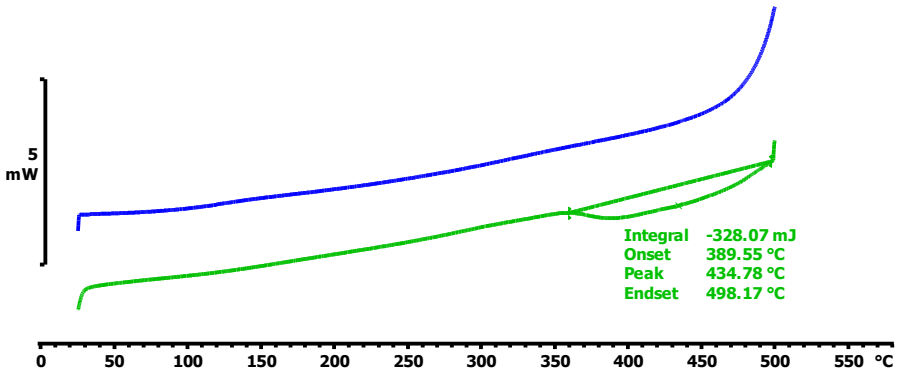

Spectrum 34: Single DSC heating/cooling cycle of **N3** (nano-CoHCF).

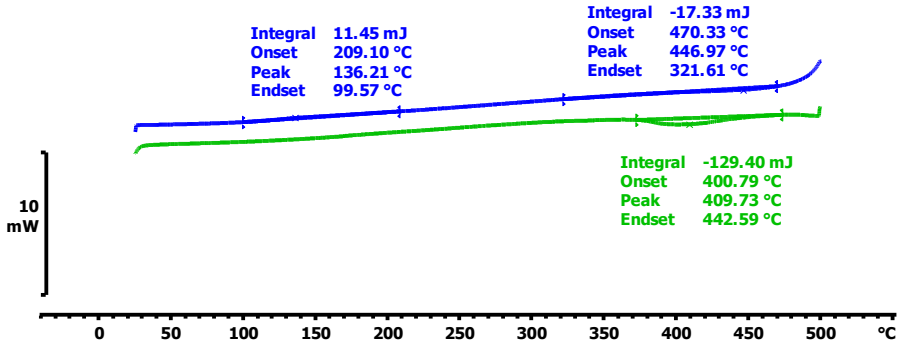

^{1}H NMR spectra

Spectrum 35: ^{1}H NMR spectrum of hydrogenation of 1-octene after 12 hours using **N3** generated using a Bruker Avance II 600 NMR spectrometer.

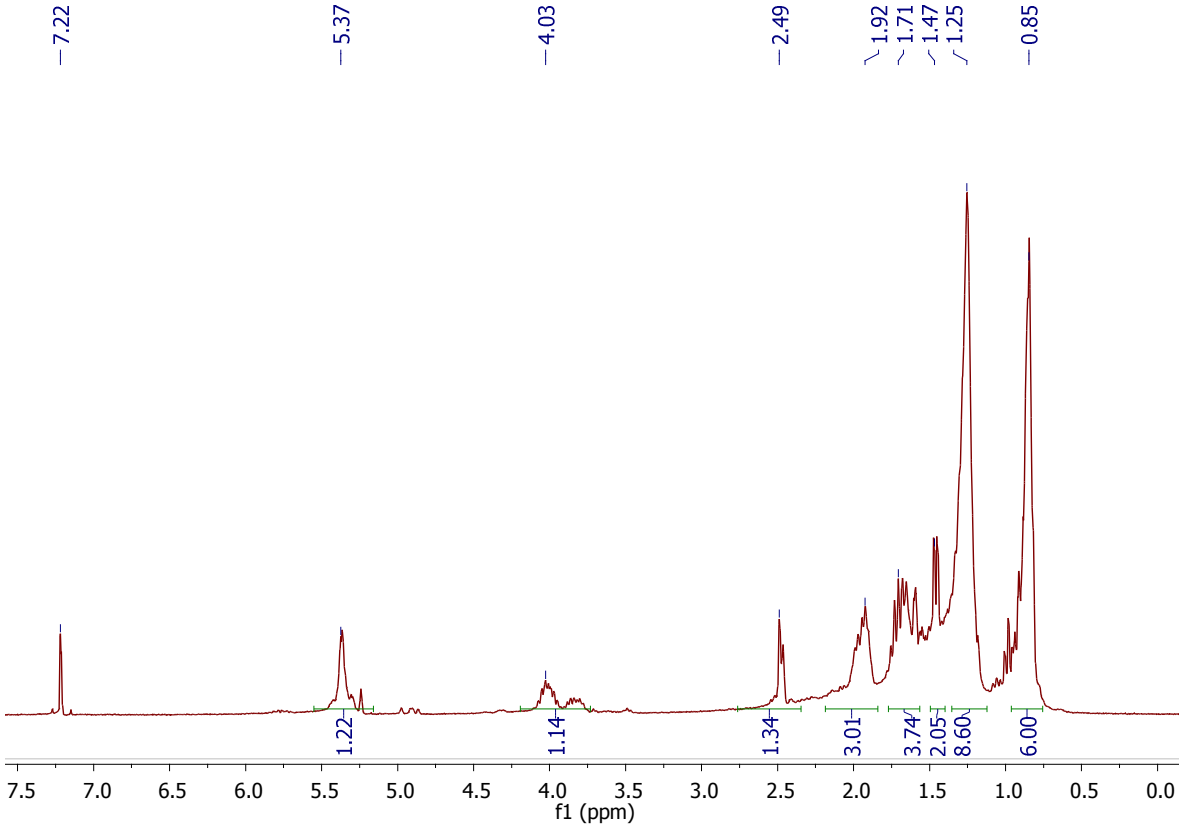

Declaration

I, Stephanus Johannes Gerber, declare that the dissertation hereby submitted by me for the degree Magister Scientiae at the University of the Free State is my own independent work and has not previously been submitted by me at another university/faculty. I further more cede copyright of the dissertation in favour of the University of the Free State.

Signed:..... Date:.....

Acknowledgements

Without the Lord I will not have achieved what I have achieved today. ***Do not be afraid for I am with you, do not be dismayed for I am your God. I will strengthen you, I will help you***. – *Isaiah 41:10.* To Him I am thankful for protecting and guiding me the past 28 years.

Angelique Gerber: No amount of words can describe the greatness of my wife. She is my passion and my queen. You have supported me through too much in so little time. I am forever in your debt my love.

Stephanie Gerber: My mom, she has always given me guidance when I was unsure. Always keeping me motivated for my own goals. Dankie Kuluki.

Dr. Lizette Erasmus: I could not have asked for a better supervisor. I wish to thank her for her guidance as well as her patience and support. Without her, I would still be busy in the laboratory.

Prof. Jannie Swarts: Father figure to all who steps into the physical chemistry group. I will miss you professor and cherish the fond memory of what you meant to us all.

Prof. Walter Purcell: Thank you for seeing me on a regular basis when I needed advice. I greatly appreciate the time you made for me and treating me like a son as well as a friend when I needed it.

I would like to thank my friends Coenraad Lubbe, Dihan Fury and Braam van Niekerk. Your weekly/monthly calls and motivational talks kept me going during the tough times the past 6 years.

All my colleagues in the physical chemistry group. It was an absolute pleasure working with all of you and wish you all the best.

I wish to acknowledge SASOL Ltd. for their financial support during the course of this study and for understanding and assistance during troubled times.

I wish to acknowledge the NRF for their financial support during the course of this study.

Thank you.

Stefaans J. Gerber